X-Ray Scattering Studies of Charge and Orbital Ordering in Transition Metal Oxides

BLAND, STEWART,RODNEY

X-Ray Scattering Studies of Charge and Orbital Ordering in Transition Metal Oxides

by

S. R. Bland

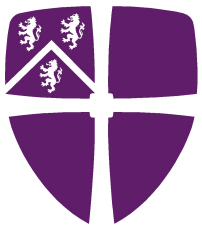

Submitted in conformity with the requirements
for the degree of Ph. D.
Department of Physics
Durham University

Contents

Declaration

The material contained within this thesis has not previously been submitted for a degree at the University of Durham or any other university. The research reported within this thesis has been conducted by the author unless indicated otherwise.

Copyright Notice

List of Publications

1. *Resonant x-ray scattering and full polarisation analysis of forbidden half-integer reflections in magnetite.*
   S. R. Bland, B. Detlefs, S. B. Wilkins, T. A. W. Beale, C. Mazzoli, Y. Joly, P. D. Hatton, J. E. Lorenzo, S. D. Brown and V. A. M. Brabers.
   J. Phys.: Conf. Ser. **211**, 012009 (2010)

2. *Soft x-ray diffraction from lattice constrained orbital order in* $Pr(Sr_{0.1}Ca_{0.9})_2Mn_2O_7$.
   T. A. W. Beale, S. R. Bland, R. D. Johnson, P. D. Hatton, J. C. Cezar, S. S. Dhesi, D. Prabhakaran and A. T. Boothroyd.
   J. Phys.: Conf. Ser. **211**, 012007 (2010)

3. *X-ray resonant scattering study of the incommensurate charge-orbital density wave in* $La_{2-2x}Sr_{1+2x}Mn_2O_7$ *(*$x = 0.7$*).*
   T. A. W. Beale, S. R. Bland, P. D. Hatton, P. Thompson, D. Prabhakaran and A. T. Boothroyd.
   J. Phys.: Conf. Ser. **211**, 012006 (2010)

4. *Observed and calculated energy spectra of Bragg-forbidden reflections in* YVO_3.
   R. D. Johnson, T. A. W. Beale, Y. Joly, S. R. Bland, P. D. Hatton, C. Mazzoli, L. Bouchenoire and D. Prabhakaran and A. T. Boothroyd.
   J. Phys.: Conf. Ser. **200**, 012073 (2010)

5. *Thermally induced rotation of* $3d$ *orbital stripes in* $Pr(Sr_{0.1}Ca_{0.9})_2Mn_2O_7$.
   T. A. W. Beale, S. R. Bland, R. D. Johnson, P. D. Hatton, J. C. Cezar, S. S. Dhesi, M. v. Zimmermann, D. Prabhakaran and A. T. Boothroyd.
   Phys. Rev. B **79**, 054433 (2009)

6. *Probing ion-specific magnetism in multiferroics.*
   R. D. Johnson, S. R. Bland, C. Mazzoli, T. A. W. Beale, C-H. Du, C. Detlefs, S. B. Wilkins and P. D. Hatton.
   ESRF Highlights 2008 (2009)

7. *Full polarization analysis of resonant superlattice and forbidden x-ray reflections in magnetite.*
   S. R. Bland, B. Detlefs, S. B. Wilkins, T. A. W. Beale, C. Mazzoli, Y. Joly, P. D. Hatton, J. E. Lorenzo and V. A. M. Brabers.
   J. Phys.: Condens. Matter **21**, 485601 (2009)

8. *Determining crystal field distortions of YVO_3 through x-ray scattering.*
   T. A. W. Beale, R. D. Johnson, S. R. Bland, P. D. Hatton, L. Bouchenoire, A. T. Boothroyd and D. Prabhakaran.
   Solid State Phenomena **152**, 147 (2009)

9. *Nature of the magnetic order and origin of induced ferroelectricity in $TbMnO_3$.*
   S. B. Wilkins, T. R. Forrest, T. A. W. Beale, S. R. Bland, H. C. Walker, D. Mannix, F. Yakhou, D. Prabhakaran, A. T. Boothroyd, J. P. Hill, P. D. Hatton, and D. F. McMorrow.
   Phys. Rev. Lett. **103**, 207602 (2009)

10. *Magnetic structure determination using polarised resonant x-ray scattering.*
    P. D. Hatton, R. D. Johnson, S. R. Bland, C. Mazzoli, T. A. W. Beale and S. B. Wilkins.
    J. Mag. Mag. Mat. **321**, 810 (2009)

11. *Ordering of localized electronic states in multiferroic $TbMnO_3$: a soft x-ray resonant scattering study.*
    T. R. Forrest, S. R. Bland, S. B. Wilkins, H. C. Walker, T. A. W. Beale, P. D. Hatton, D. Prabhakaran, A. T. Boothroyd, D. Mannix, F. Yakhou and D. F. McMorrow.
    J. Phys.: Condens. Matter **20**, 422205 (2008)

12. *Determination of the magnetic structure of the rare earth ions in $TbMn_2O_5$ using full polarizarion analysis.*
    R. D. Johnson, S. R. Bland, C. Mazzoli, T. A. W. Beale, C-H. Du, C. Detlefs,

S. B. Wilkins, and P. D. Hatton.
Phys. Rev. B **78**, 104407 (2008)

13. *An x-ray diffraction study of the temperature-induced structural phase transitions in $SmVO_3$.*
R. D. Johnson, I. R. Evans, S. R. Bland, D. G. Free, T. A. W. Beale, P. D. Hatton, L. Bouchenoire, D. Prabhakaran, and A. T. Boothroyd.
Submitted to Phys. Rev. B

14. *Analysis of the resonant x-ray scattering signal from the $4p$ quadrupole moment in YVO_3.*
T. A. W. Beale, R. D. Johnson, Y. Joly, S. R. Bland, P. D. Hatton, L. Bouchenoire, C. Mazzoli, D. Prabhakaran, and A. T. Boothroyd.
Submitted to Phys. Rev. B

15. *Antiferromagnetically spin polarized oxygen observed in magneto-electric $TbMn_2O_5$.*
T. A. W. Beale, S. B. Wilkins, R. D. Johnson, S. R. Bland, Y. Joly, T. R. Forrest, D. F. McMorrow, F. Yakhou, A. T. Boothroyd and P. D. Hatton.
Submitted to Phys. Rev. Lett.

16. *A study of charge order in Fe_2OBO_3 through polarized resonant x-ray diffraction.*
S. R. Bland, M. Angst, S. Adiga, V. Scagnoli, R. D. Johnson, J. Herrero-Martín and P. D. Hatton.
Submitted to Phys. Rev. B

17. *Resonant x-ray scattering from charge-orbital satellites in lutetium ferrate.*
S. R. Bland, J. De Groot, T. A. W. Beale, F. Yakhou, V. Scagnoli, S. S. Dhesi, M. Angst and P. D. Hatton.
In Preparation

Abstract

X-Ray Scattering Studies of Charge and Orbital Ordering in Transition Metal Oxides

S. R. Bland

This thesis focusses on the phenomena of charge ordering and orbital ordering in transition metal oxides, using the technique of resonant x-ray diffraction (RXD). The technique is suited to such studies, as it provides an elemental and band specific probe of long range electronic correlations. Here, we present hard and soft x-ray diffraction results on iron and manganese compounds, and demonstrate the utility of resonant x-ray diffraction in revealing their electronic properties.

By performing comprehensive hard x-ray RXD studies on the complex charge ordered structures of magnetite and iron oxyborate, we demonstrate that both systems possess non-integer charge order by using the FDMNES simulation code. We find certain reflections have anisotropic polarisation dependencies, due entirely to the crystal structure, with no need to invoke orbital order to explain the observations. In both materials we demonstrate that the anomalous scattering components can result in a surprising conversion from linearly to non-linearly polarised light, through two subtly different interference processes. This is the first report of such mechanisms.

By performing soft x-ray scattering on $Pr(Sr_{0.1}Ca_{0.9})_2Mn_2O_7$, we have provided the first direct observation of the orbital rotation within this compound. We have found that there is no apparent change in the orbital occupation during the stripe rotation, but an increase in the charge disproportionation upon cooling. We have used soft x-ray RXD on lutetium ferrate to discover an anisotropic contribution to the scattering at the charge order wavevector. This is not apparent when probing the crystal structure directly using hard x-rays. We attribute such a signal to charge-orbital order within the system, in contrast to previous claims that the system is an orbital glass.

Acknowledgements

This thesis represents several years work performed on multiple beamlines, and so would have been impossible to produce without the dedicated work of many people. I thank here as many people as I can individually, but in case I miss anybody, I am very sorry.

First and foremost I must thank my supervisor Peter Hatton who has given me constant support and guidance throughout my PhD, except for those times he was playing *Call of Duty* in the back room. Peter's advice and instruction has been invaluable, as has the freedom he has allowed me to pursue projects which interest me. Secondly I must thank Tom Beale, who has been on hand to perform experiments with me, and answer incessant questions since the start. Tom's knowledge on the practical features of beamlines is phenomenal, and without his experimental support I would no doubt have caused a lot more damage than I did. I thank Roger Johnson for similarly providing experimental support throughout my PhD. Roger has assisted me on many experiments, provided constant advice, and destroyed every chair he has ever sat on. I must thank Stuart Wilkins, who has taught me a great deal and has been essential in discussing the finer points of resonant x-ray diffraction (RXD). I thank John Dobson for keeping the x-ray source(s) in Durham running over the last four years. When it comes to removing a module, and slamming it back again, no one does it quite like John. I thank David Pattinson for cutting endless crystals, and Ian Terry and Damian Hampshire for use and operation of the MPMS and PPMS respectively.

I now thank those I have collaborated with on these projects. I thank Emilio Lorenzo and Yves Joly from the CNRS, with whom I worked extensively on magnetite. Without their input, not only would the work on magnetite have been diminished, but my insight into RXD would not be what it is today. I thank Manuel Angst from Forschungszentrum Jülich, who not only provided the crystals of iron oxyborate and lutetium ferrate, but also participated in the experiments and has been a constant help throughout my analysis of the data. Similarly I thank Manuel's PhD students Joost De Groot and Shilpa Adiga, who I worked with on the $LuFe_2O_4$ and

Fe_2OBO_3 experiments, respectively. I thank D. Prabhakaran and Andrew Boothroyd from Oxford University for the supply of the $Pr(Sr_{0.1}Ca_{0.9})_2Mn_2O_7$ crystal studied in this thesis, but I must also thank them for the numerous other crystals that they have sent me, which are not included in this thesis. I also thank V. A. M. Brabers from Eindhoven University for the supply of the superb crystal of magnetite.

I thank those from beamlines around the world who have contributed a great deal: not only by providing local support, but by providing a considerable amount of advice and instruction. I thank Claudio Mazzoli, Valerio Scagnoli, Javier Herrero-Martín, Blanka Detlefs, Flora Yakhou, Julio Cezar and Luigi Paolasini from the ESRF. I thank Laurence Bouchenoire, Simon Brown, Peter Normile, Paul Thompson and Oier Bikondoa from XMaS at the ESRF. I thank Urs Staub and Raquel De-Souza from the Swiss Light Source. I thank Martin von Zimmermann from HASYLAB and Mark Roper from Daresbury. I thank Sarnjeet Dhesi, Steve Collins and Alessandro Bombardi from Diamond Light Source.

I also thank those with whom I have collaborated and worked with on projects that are not a part of this thesis. Namely Des McMorrow and Tom Forrest from UCL, Heather Lewtas from Oxford University, Helen Walker from the ESRF, Chao-Hung Du from Tamkang University, Yeong-Ah Soh from Imperial College London and Ravi Kummamuru from Dartmouth College.

Finally, I thank my parents for all of their love and support, and to whom I promise I will get a proper job eventually.

And here we go...

Chapter 1

Introduction

1.1 Outline

X-ray diffraction is now a mature technique, having been discovered over one hundred years ago through the ground breaking work of Max von Laue and the Braggs. The technique has enabled the refinement of crystal structures ranging from common minerals to complex proteins, as well as providing direct observation of superstructural electron correlations, as this thesis will focus on. The only truly comparable technique to x-ray diffraction for observing long range correlations is neutron diffraction, which also offers the significant advantage of being highly sensitive to the magnetic structures of materials. However, even non-resonant x-ray scattering is sensitive to magnetic structures, as demonstrated in the pioneering studies of de Bergevin and Brunel [1, 2]. With the advent of synchrotron radiation, magnetic x-ray scattering has become a complementary technique to neutron scattering, as when the x-ray resonant enhancement process is exploited, the result is a direct probe of electron bands. However, the true advantage of x-rays over neutrons becomes apparent when it is the charge rather than the magnetic properties of a system that are of interest. The strong coupling between the electrons and the photon's electric field makes x-ray scattering the probe of choice in studies of charge and orbital order.

To begin we present a brief overview of the basics of x-ray diffraction, before

discussing the types of electronic order studied in this thesis. The fundamentals of the theory of resonant x-ray diffraction are presented, before discussing exactly what the technique is sensitive to. In the body of the text we present resonant x-ray diffraction results from several transition metal oxides, namely magnetite, Fe_3O_4; iron oxyborate, Fe_2OBO_3; a praseodymium-strontium-calcium bilayer manganite, $Pr(Sr_{0.1}Ca_{0.9})_2Mn_2O_7$ and lutetium ferrate, $LuFe_2O_4$. These systems possess very different crystal structures, but all display charge ordering at relatively high temperatures.

1.2 Fundamentals of Diffraction

Here, we present the fundamentals of diffraction, largely based on the approach of Als-Nielsen and McMorrow [3]. For more information the reader is suggested to consult this source.

In order to observe a diffraction signal from a crystal it is necessary that the phase difference between reflected waves is proportional to 2π. The angles that fulfil this requirement are given by equation 1.1, Bragg's Law,

$$n\lambda = 2d_{hkl}\sin(\theta) \tag{1.1}$$

where, d_{hkl} is the spacing between the crystal planes, θ is the angle between the correlated atomic planes and the incoming wave, n is an integer corresponding to the order of the reflection and λ is the wavelength. An improved description may be reached by considering how each atom responds to the radiation, which is then included as part of the whole lattice. The problem is simplified by only considering the x-rays as being scattered once, in an elastic process: this is the *kinematical approximation*. Using the classical description, where an electron acts as a dipole when exposed to the radiation, the principal scattering parameter for a single electron is the *Thomson scattering length* [3], equation 1.2.

$$r_0 = \left(\frac{e^2}{4\pi\varepsilon_0 mc^2}\right) \tag{1.2}$$

For a charge distribution, rather than a single electron, it is necessary to modify the scattering length to equation 1.3,

$$-r_0 f(\mathbf{Q}) = -r_0 \int \rho(\mathbf{r}) e^{i\mathbf{Q}\cdot r}\, d\mathbf{r} \tag{1.3}$$

where the charge distribution is described by $\rho(\mathbf{r})$, and $e^{i\mathbf{Q}\cdot r}$ is a phase factor which arises from the phase differences due to scattering from different charge elements. The term $\mathbf{Q}$ is known as the *scattering vector*, and is defined by equation 1.4,

$$\hbar\mathbf{Q} = \hbar\mathbf{k} - \hbar\mathbf{k}' \tag{1.4}$$

where $\mathbf{k}$ and $\mathbf{k}'$ represent the wavevectors of the incoming and scattered waves respectively. Here, as in the rest of this thesis, the prime is used to denote a scattered term. The term $f(\mathbf{Q})$ is the *atomic form factor*, which is only weakly dependent on energy far from an absorption edge. The atomic form factor is related to the scattering cross-section, that is the number of scattered photons per second per unit of the solid angle, by

$$\frac{d\sigma}{d\Omega} = r_0^2 f(\mathbf{Q})^2 P \tag{1.5}$$

where P is a polarisation factor, which for non-resonant charge scattering is given be $P = \boldsymbol{\epsilon}' \cdot \boldsymbol{\epsilon}$, where $\boldsymbol{\epsilon}$ and $\boldsymbol{\epsilon}'$ represent the incident and scattered polarisation states of the photon. In a crystal, atoms sit at sites within a unit cell, which repeats infinitely in three dimensions. By summing the atomic form factor over all the atoms in a unit cell we may obtain the *unit cell structure factor*, equation 1.6,

$$F^{cell}(\mathbf{Q}) = \sum_{\mathbf{r}_j} f_j(\mathbf{Q}) e^{i\mathbf{Q}\cdot\mathbf{r}_j} \tag{1.6}$$

where f_j and $\mathbf{r}_j$ are the atomic form factor and position, for atom j. We may then sum these terms into a lattice, equation 1.7,

$$F^{crystal}(\mathbf{Q}) = \sum_{\mathbf{r}_j} f_j(\mathbf{Q}) e^{i\mathbf{Q}\cdot\mathbf{r}_j} \sum_{\mathbf{R}_n} e^{i\mathbf{Q}\cdot\mathbf{R}_n} \tag{1.7}$$

where $\mathbf{R}_n$ gives the lattice vectors, of the form,

$$\mathbf{R}_n = n_1\mathbf{a_1} + n_2\mathbf{a_2} + n_3\mathbf{a_3} \tag{1.8}$$

where n_1, n_2, n_3 are integers and $\mathbf{a_1}, \mathbf{a_2}, \mathbf{a_3}$ give the lattice parameters. In order for the second sum in equation 1.7 to be large, we require that $\mathbf{Q} \cdot \mathbf{R}_n = 2\pi \cdot integer$. This requires that $\mathbf{Q}$ is of the form,

$$\mathbf{Q} = h\mathbf{a_1}^* + k\mathbf{a_2}^* + l\mathbf{a_3}^* \tag{1.9}$$

where $\mathbf{a_1}^*, \mathbf{a_2}^*, \mathbf{a_3}^*$ are reciprocal lattice vectors and h, k, l are integers. These integers correspond to the Miller indices of the family of planes that contribute to diffraction, or more conveniently as points in reciprocal space. We define these reciprocal lattice vectors with respect to the real space lattice as

$$\begin{aligned} \mathbf{a_1^*} &= 2\pi \frac{\mathbf{a_2} \times \mathbf{a_3}}{\mathbf{a_1} \cdot (\mathbf{a_2} \times \mathbf{a_3})} \\ \mathbf{a_2^*} &= 2\pi \frac{\mathbf{a_3} \times \mathbf{a_1}}{\mathbf{a_2} \cdot (\mathbf{a_3} \times \mathbf{a_1})} \\ \mathbf{a_3^*} &= 2\pi \frac{\mathbf{a_1} \times \mathbf{a_2}}{\mathbf{a_3} \cdot (\mathbf{a_1} \times \mathbf{a_2})}. \end{aligned} \tag{1.10}$$

The scattered intensity I is related to $F^{crystal}$ by $I \propto \mid F^{crystal} \mid^2$, and so depending upon the symmetry of the crystal, some sets of planes may not contribute to the scattered intensity. These *forbidden* Bragg reflections occur when $F^{crystal}$ is zero, and are fundamentally disallowed by symmetry. These differ from the case of *accidental extinctions* which occur by the chance selection of structure and atoms that add to give (close to) zero intensity.

It should be clear as to how the arrangement of atoms in a unit cell, within a lattice, produces reflections at certain positions in reciprocal space, (h k l). However, once all degrees of freedom (specifically orbital, spin and charge) are taken into account, the unit cell may be larger than the crystallographic description. The effect is that we may detect new reflections at Bragg forbidden values of recipro-

cal space. These *superlattice* reflections are generally observed at wavevectors of ($\pm\delta_a$, $\pm\delta_b$, $\pm\delta_c$) around the Bragg reflections, where $\delta_{a,b,c}$ refers to the ratio of the crystallographic unit cell to the larger unit cell, in the specified direction. These reflections are generally weak, and in order to observe them it is beneficial to exploit the anomalous terms in the atomic form factor that become significant at the absorption edges of the elements. This total atomic form factor is given as

$$f(\mathbf{Q}, \hbar\omega) = f(\mathbf{Q}) + f_{spin}(\mathbf{Q}) + f'(\hbar\omega) + if''(\hbar\omega) \tag{1.11}$$

where $f_{spin}(\mathbf{Q})$ is the non-resonant magnetic contribution, and $f'(\hbar\omega)$ and $f''(\hbar\omega)$ are the resonant terms. The mechanism for the resonant enhancement involves the virtual absorption of an x-ray by a core electron, resulting in a temporary transition to a localised or delocalised band, followed by the emission of a photon. However, even using this enhancement the superlattice reflections are much weaker than Bragg reflections, hence the requirement of a high intensity x-ray source.

1.3 Charge Order and Orbital Order

Charge ordering has been the subject of a substantial number of studies in condensed matted physics, and represents a key concept in helping us understand a range of phenomena. Charge ordering may simply be considered as the ordering of different valences over formerly equivalent crystallographic sites. A variety of transition metal oxides display charge order, such as sodium cobaltate [4] and cuprates [5]. Perhaps the two most well known systems are magnetite, Fe_3O_4, and the cubic perovskite manganites $RA\mathrm{MnO}_3$, where R represents a trivalent lanthanide (*e.g.* La, Pr) and A represents a divalent alkaline earth element (*e.g.* Sr, Ca). These latter materials are part of the Ruddlesden-Popper (RP) series, given by $(R, A)_{n+1}\mathrm{Mn}_n\mathrm{O}_{3n+1}$. A wide range of interesting phenomena exist in this family, including colossal magnetoresistance in some of the $n = 2$ members [6]. As will be discussed in the next chapter, Fe_3O_4 was the first system in which charge order was proposed, after Verwey observed a large increase in the resistivity on cooling below

$T_{\mathrm{V}} \approx 120$ K [7, 8], see figure 1.1. If we consider charge ordering as the localisation of electrons in a particular pattern, it is by no means surprising that the resistivity of materials increases when entering the charge ordered phase. Verwey's model involved Fe^{2+} and Fe^{3+} ions being ordered over previously equivalent sites. This original description is compatible with Anderson's criteria [10] for charge ordering, whereby the Coulomb energy of the system is reduced.

Charge ordering in the manganite perovskites was first predicted by Goodenough in the 1950s [11]. These systems have since been adopted as the classic cases of charge and orbital ordering. Goodenough's charge ordering model for half-doped mixed valence manganites consisted of alternately arranged Mn^{3+} and Mn^{4+} ions, in a *checkerboard* arrangement, see figure 1.2. Indeed this is the preferred arrangement for the majority of half-doped perovskites, with other orderings becoming possible when the balance between divalent and trivalent ions moves far to one side, see *e.g.* reference 12. Numerous experimental studies have used diffraction to study the checkerboard ordering in the RP series, perhaps most prominently in $La_{0.5}Sr_{1.5}MnO_4$ [13, 14], where the charge and structural changes below 220 K have been observed. It is important to introduce the concept of orbital ordering at this point, as it is part of Goodenough's original prediction, and is fundamental to the electronic ground state of the manganites. As for charge ordering, the concept is simple: a long range ordered preferential occupation of the valence orbitals. In this situation, this specifically regards the $3d$ orbitals of the transition metal ions.

In free space the five $3d$ orbitals are degenerate [15–17]. However, when surrounded by anions (typically oxygen ions) the orbitals are split in energy. The effect of the crystal field depends on the number of electrons on both the metal ion, and the arrangement of oxygen atoms around them. Figure 1.3 demonstrates the resulting crystal field splitting for the arrangements relevant to this thesis. The reason the orbitals are split in this manner can be understood once the shapes of the orbitals and their environments are taken into account, for example consider the octahedra shown in figure 1.4. Here, (a) and (b) have orbital lobes which point directly towards the surrounding anions, while (c), (d) and (e) have lobes which point in-

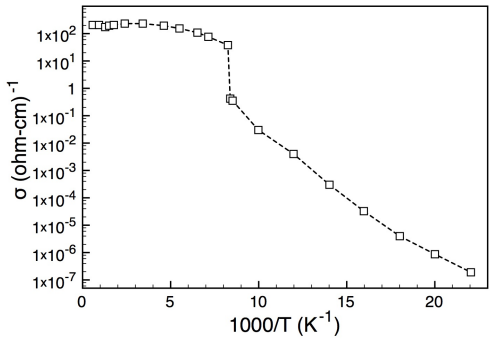

Figure 1.1: The decrease in conductivity in bulk magnetite at T_{V} (≈ 120 K). Figure re-drawn from reference 9 by Miles *et al.*

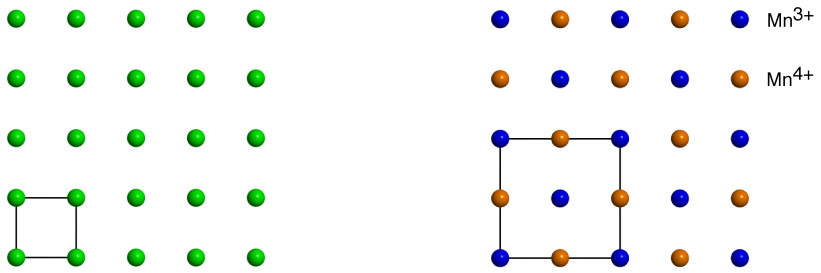

Figure 1.2: A layer of manganese atoms, (a) before and (b) after checkerboard charge ordering has taken place. The green ions in (a) have the same valence of +3.5. The black line shows the charge order unit cell, which in (a) corresponds to the crystallographic unit cell.

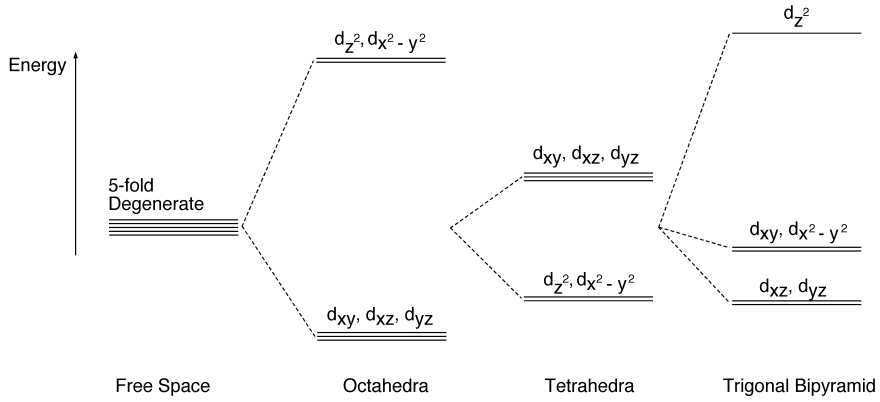

Figure 1.3: The crystal field splitting of the $3d$ orbitals for several surrounding coordinations. The relative values for each splitting are approximate, but qualitatively correct [18].

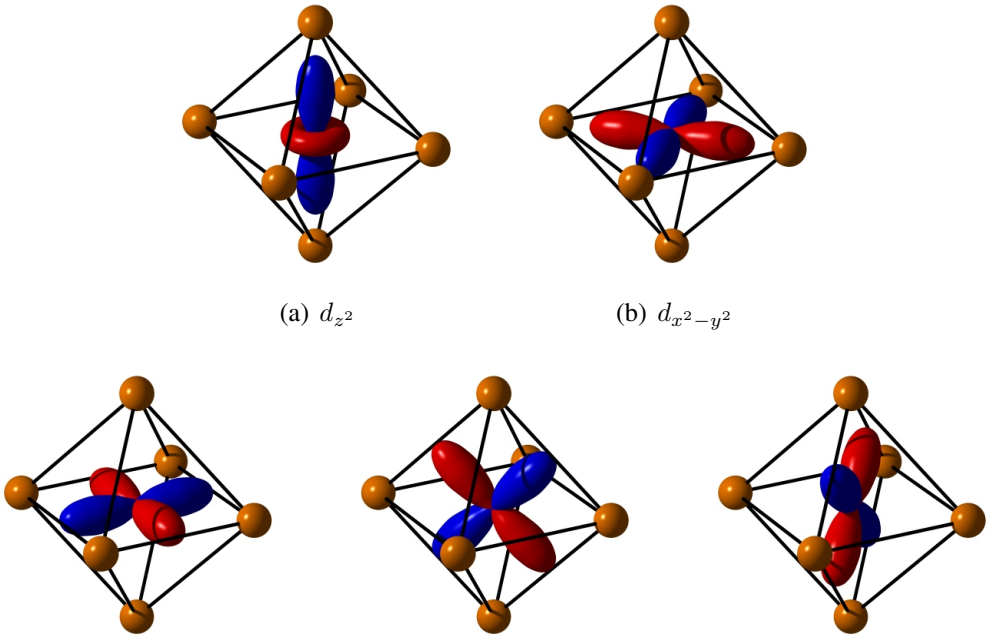

(a) d_{z^2} (b) $d_{x^2-y^2}$

(c) d_{xy} (d) d_{yz} (e) d_{zx}

Figure 1.4: The five $3d$ orbitals in an octahedrally coordinated environment. The orange spheres represent anions, typically oxygens, while the orbitals correspond to transition metal sites. Orbitals (a) and (b) have higher energy in an octahedral environment, and are labelled the e_g orbitals, while (c), (d) and (e) are labelled t_{2g}.

between the anions. Thus (a) and (b) are higher in energy, and so more unstable. However, we must also take the Jahn-Teller effect into consideration, which states that when the electronically degenerate states are unequally occupied, there must be a distortion present to lower the energy [17]. For the case of the octahedra, this effect is strongest when the e_g orbitals are unequally occupied. The nature of this distortion is displayed in figure 1.5. The result is further splitting of the orbital degeneracy, as illustrated in figure 1.6. Within the present context, this effect is important for two reasons. Firstly, the effect results in one orbital being preferentially occupied, and secondly, orbital ordered systems are expected to be Jahn-Teller distorted systems as well. This orbital ordering was also predicted by Goodenough, and the stripe orbital ordering scheme for half-doped manganites is shown in figure 1.7. The associated lattice distortion in its ordered form is referred to as a *cooperative Jahn-Teller* distortion. Thus an interesting question arises: in charge and orbital ordered systems, is the lowest energy electron configuration a result of the charge repulsion, as in a Wigner crystal [19, 20], or driven as a result of the strain from the cooperative distortion [21]? Debate over which of these scenarios is favoured in the manganites remains a popular issue [12, 20–22].

The orbitals fill in accordance with Hund's rules, since the crystal field splitting is not especially large. The orbital filling for the octahedral coordination is shown schematically in figure 1.8 for the situations relevant to this thesis. For Mn^{4+} and Fe^{3+} it is clear that there should be no directionally dependent preferential occupation of the orbitals, and no Jahn-Teller effect. However, for Mn^{3+} and Fe^{2+} there should be a preferential occupation of one e_g and t_{2g} orbital respectively. The Jahn-Teller effect for the Mn^{3+} ion is expected to be larger, as the orbital lobe points directly at the surrounding anion. Nevertheless, the Jahn-Teller effect is still expected for the Fe^{2+} ion.

The classical definition of charge order is of integer valences localised at ionic sites. The original definition of a charge density wave (CDW) in a one-dimensional metal is of a density modulation of conduction band electrons as a result of a Peierls instability [23–25]. That is, the energy of the system can be lowered if an energy

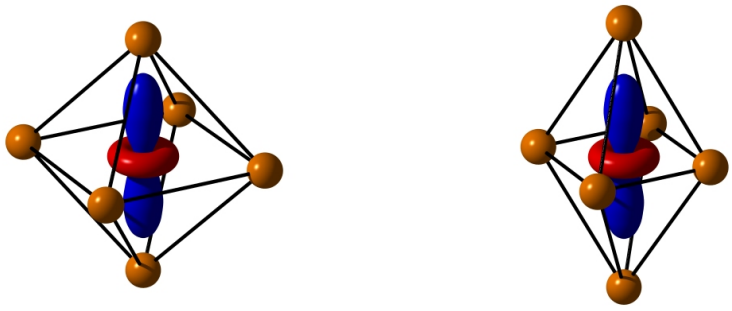

(a) (b)

Figure 1.5: An occupied d_{z^2} orbital in an octahedral environment, without (a) and with (b) a Jahn-Teller distortion. Other orbitals will of course distort the octahedra in different ways.

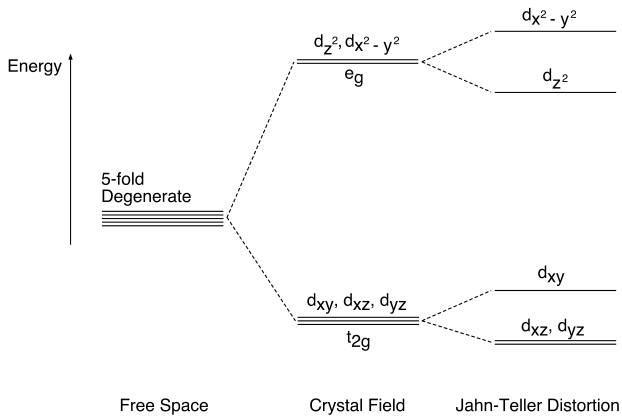

Figure 1.6: An example of how the Jahn-Teller effect can further split the degeneracy of the $3d$ orbitals, for a d^4 system [15]. This is illustrative, and the exact splitting depends on the crystal field strength, and critically on the number of occupied orbitals.

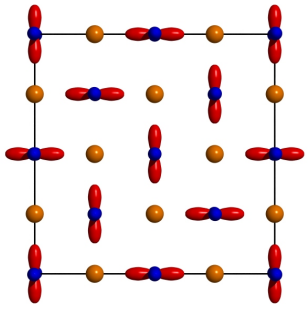

Figure 1.7: Checkerboard charge order and stripe orbital order in the RP series. The orbital stripes correspond to the identical orbitals running from the lower left to the upper right. The black line shows the orbital order unit cell.

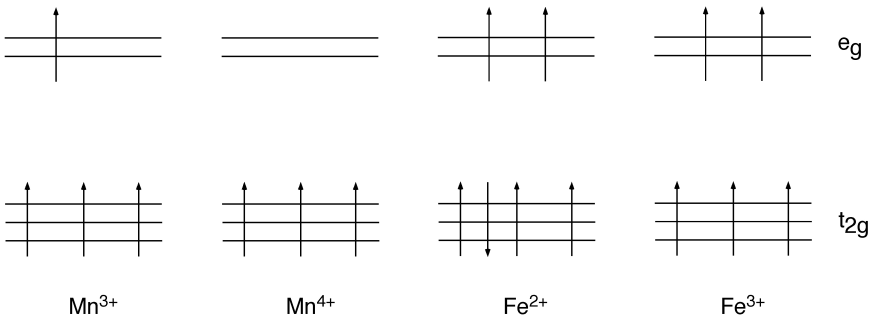

Figure 1.8: Orbital filling of selected manganese and iron ions under octahedral coordination.

gap opens at the Fermi energy. This instability drives the formation of a strain wave known as a Peierls distortion, opening the gap. In a one-dimensional material this should produce a lattice modulation with wavevector $2\mathbf{k_F}$. In three-dimensional materials the wavevector can be deduced by considering where regions of the Fermi surface can be moved to directly coincide with each other. This is referred to as Fermi surface nesting. The vector which links these surfaces determines the corresponding wavevector. It is also important to note that a CDW can slide, meaning that such a material does not necessarily have as high a resistance as may be expected, although the wave is often pinned by defects, eliminating this effect.

Numerous studies using resonant x-ray diffraction [26–30] and bond valence sum (BVS) calculations [31, 32] on materials which are traditionally labelled as charge ordered have shown that the valencies of ion sites are non-integer. Other studies have shown that in such materials the charge-lattice coupling may be too weak to localise the charges to the sites [33], while recent theoretical calculations have demonstrated that any change in valence local to the transition metal ion is incredibly small; rather it is the strength of the crystal field which changes [34]. Several studies of the manganites have indicated that by describing these traditionally charge ordered systems as CDWs, experimental observations of wavevector [35, 36], resistance [37], magnetisation and specific heat [38] can be explained. Further, Fermi surface nesting at the correct wavevector has also been observed [39]. Is it then appropriate to declare that charge ordering is an unhelpful label, and instead always use the term CDW instead? We believe it is not, as although the classical definition for a charge ordered system is clearly not correct, the classical definition of a CDW is also generally not applicable. Recently Johannes and Mazin [25] have argued that few systems show a genuine Peierls instability, as the transitions in real systems are not purely electronically driven. Instead the transition relies on the electronic and ionic systems, and the strong electron-phonon coupling. They go on to point out that Fermi surface nesting does not always predict the correct wavevector, and reason that there is no meaningful difference between these non-classical CDW systems and a system with an incommensurate lattice distortion. In

this thesis we therefore maintain the nomenclature of *charge order*, as we believe a modern definition must acknowledge that the charge is non-localised to the ion site, and must be considered as non-integer within the region of the ion. Indeed, a charge density modulation but without invoking the term CDW, as this term includes the assumption of a true Peierls distortion which is not necessarily the case.

1.4 Experimental Geometry

Before proceeding further it is wise to define the geometry in which the experimental work described herein was performed. The vast majority of the resonant x-ray scattering experiments were performed in vertical scattering geometry, and so the experimental geometry is described as such. For more information on diffraction geometries the reader is referred to reference 40 and related citing articles.

The basis of the polarisation is traditionally given in terms of two orthogonal vectors *in* and *perpendicular to* the scattering plane. The term $\boldsymbol{\epsilon}_\sigma$ is reserved for the component of the polarisation perpendicular to $\mathbf{k}$ and the scattering plane, while the term $\boldsymbol{\epsilon}_\pi$ designates the component perpendicular to $\mathbf{k}$ while remaining in the scattering plane, see figure 1.9. However, it is customary to omit the $\boldsymbol{\epsilon}$ term, and solely use the σ and π notation. In order to study the anisotropy of reflections the sample is usually rotated around the scattering vector, as shown by the motion ϕ in figure 1.9. Traditionally light from synchrotrons is linearly polarised by the source, producing horizontally polarised light, which corresponds to σ polarisation for vertical scattering. However, with the advent of more advanced insertion devices and phase plates, it is instead possible to rotate the incident polarisation of the light to any arbitrary polarisation. The method used for producing this light, and the specific advantages of this technique will be discussed in more detail in following chapters.

After scattering from the sample, the diffracted light can then be scattered again, from an analyser crystal, in order to selectively study a specific linear polarisation channel. This is performed by choosing an analyser crystal which has an appro-

priate value of d_{hkl} for the energy being used. Specifically the value of 2θ should be close to $90°$. As Thomson scattering has a polarisation dependence given by $\boldsymbol{\epsilon}' \cdot \boldsymbol{\epsilon}$, only light in the incident σ channel (relative to the analyser) is scattered when $2\theta = 90°$. Thus by rotating the analyser crystal and the detector stage around η, as shown in figure 1.10, any linear polarisation state can be accessed. It is often convenient to collect data at a number of different η positions, and fit the data to extract the familiar Stokes' parameters [42]. This is preferable as a single Stokes' parameter is a more accurate value than a measurement in any single linear polarisation channel, and because the self normalisation inherently dismisses the absolute intensity, which is generally not useful for studies of this type.

1.5 Resonant X-Ray Diffraction

1.5.1 Mathematical Foundation

The theory of resonant scattering is discussed here, regarding the form of the scattering cross-section, following the approach of Blume [43] and Altarelli [44]. The reader is advised to consult these, and the associated works by Hannon *et al.* [45] and Blume and Gibbs [41] for more detail.

The Hamiltonian for the complete system contains the energy of the electron, the electromagnetic field of the radiation and the interaction terms. However, when considering the scattering process it is only necessary to use the interaction terms, which combine photon and electron components. This *interaction Hamiltonian* is expressed by Blume [43, 46] as

$$H' = \underbrace{\frac{e^2}{2mc^2}\sum_i \mathbf{A}^2(\mathbf{r}_i)}_{H_1} \underbrace{-\frac{e}{mc}\sum_i \mathbf{p}_i \cdot \mathbf{A}(\mathbf{r}_i)}_{H_2} \underbrace{-\frac{e\hbar}{mc}\sum_i s_i \cdot \nabla \times \mathbf{A}(\mathbf{r}_i)}_{H_3} \tag{1.12}$$

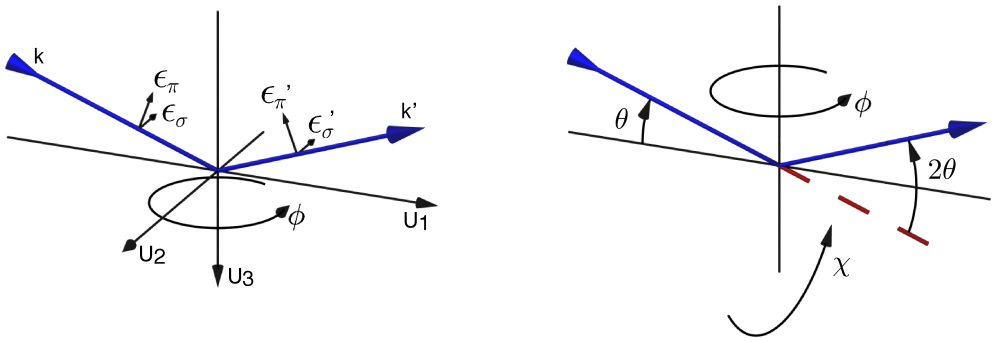

(a) (b)

Figure 1.9: The scattering geometry indicating (a) the incoming and outgoing channels, as well as the **U** basis vectors defined by this set-up [41] and (b) the motor movements. In the figure and the text, a prime signifies the scattered component.

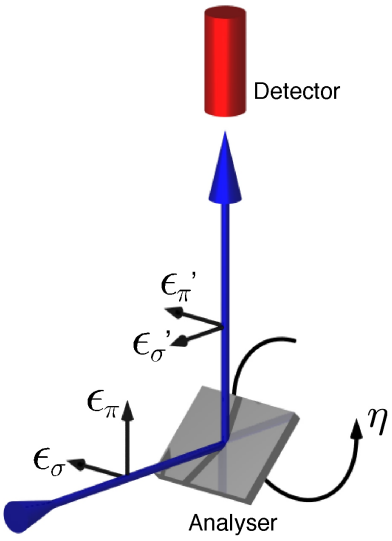

Figure 1.10: The scattering geometry of an analyser stage.

$$\underbrace{-\frac{e^2\hbar}{2(mc^2)^2}\sum_i s_i \cdot (\dot{\mathbf{A}}(\mathbf{r}_i) \times \mathbf{A}(\mathbf{r}_i))}_{H_4}$$

where $\mathbf{A}(\mathbf{r}_i)$ is the vector potential of the electromagnetic field for the i^{th} electron, at position $\mathbf{r}$, with spin and momentum $\mathbf{s}$ and $\mathbf{p}$ respectively. The vector potential is usually expressed as a Fourier series expansion, given by

$$\mathbf{A}(\mathbf{r},t) = \sum_{\boldsymbol{\epsilon},\mathbf{k}} \mathbf{A}_0 \left[\mathbf{a}_{\boldsymbol{\epsilon},\mathbf{k}} e^{i(\mathbf{k}\cdot\mathbf{r}-\omega_{\mathbf{k}}\cdot t)}\boldsymbol{\epsilon} + \mathbf{a}^\dagger_{\boldsymbol{\epsilon},\mathbf{k}} e^{-i(\mathbf{k}\cdot\mathbf{r}-\omega_{\mathbf{k}}\cdot t)}\boldsymbol{\epsilon}'\right] \tag{1.13}$$

where

$$\mathbf{A}_0 = \sqrt{\frac{\hbar}{2\varepsilon V \omega_{\mathbf{k}}}}, \tag{1.14}$$

ε is the permittivity, $\omega_{\mathbf{k}}$ is the angular frequency of the mode given by $\mathbf{k}$, $\boldsymbol{\epsilon}$ represents the polarisation vector of the mode given by $\mathbf{k}$, $\mathbf{a}$ and $\mathbf{a}^\dagger$ are creation and annihilation operators for a photon specified by $\mathbf{k}$ and $\boldsymbol{\epsilon}$, and V is the quantisation volume of the electromagnetic wave.

The transition probability per unit time, W, may be determined by applying Fermi's Golden Rule (FGR) to second order

$$W = \frac{2\pi}{\hbar}\left| < \beta \mid H' \mid \alpha > + \sum_n \frac{< \beta \mid H' \mid n >< n \mid H' \mid \alpha >}{E_\alpha - E_n}\right|^2 \delta(E_\alpha - E_\beta) \tag{1.15}$$

where α, n and β represent the initial, intermediate and final states respectively and the density of states, $\delta(E_\alpha - E_\beta)$, is required as n is a continuum of states. The states given by n are the states which we excite into at a given energy. Hence by tuning to a specific energy, the scattering is sensitive to the occupations and state of specific bands, and thus the electronic structure that the individual sites contribute to. The scattering process involves the creation and annihilation of a photon, and so to second order we only include terms quadratic in $\mathbf{A}$ in the first term, and linear in $\mathbf{A}$ in the second term. Further, we may write our initial and final states to implicitly

include the initial and final state wavevectors, as

$$\mid \alpha >\equiv\mid \alpha; \mathbf{k} > \text{ and } \mid \beta >\equiv\mid \beta; \mathbf{k}' > \tag{1.16}$$

such that

$$W = \frac{2\pi}{\hbar}\Big| < \beta \mid H_1 + H_4 \mid \alpha > + \sum_n \frac{< \beta \mid H_2 + H_3 \mid n >< n \mid H_2 + H_3' \mid \alpha >}{E_0 - E_n + \hbar\omega_{\mathbf{k}}}\Big|^2 \delta(\hbar(\omega_{\mathbf{k}} - \omega_{\mathbf{k}'})) \tag{1.17}$$

where we have now explicitly expressed the initial energy of the state to be the ground state plus some photon energy. Alternatively we could have expressed the intermediate state as including the photon energy and the above expression would instead contain a $-\hbar\omega_{\mathbf{k}}$ term. Unlike non-resonant scattering which can be considered to rely on two processes, absorption and emission, resonant scattering is a single process. However, we still require the annihilation and creation of a photon. In this regard, while resonant scattering requires two invocations of $\mathbf{A}$ (which has linear creation and annihilation operators), absorption only requires one. Thus for scattering, the H_1 and H_4 terms (which both contain two invocations of $\mathbf{A}$) are needed in the first order term of FGR, while the H_3 and H_4 terms (which each contain a single invocation) are necessary in the second order term. Nevertheless, absorption and scattering are linked, and an absorption measurement provides a direct measure of $f''(\hbar\omega)$. It is worth pointing out that the advantage of using diffraction over absorption techniques is that diffraction is automatically wavevector specific, whereas absorption simultaneously probes all elementally equivalent sites.

Far from an absorption edge it is the first terms in equation 1.17 that are important. The extra terms at the start of H_4 in equation 1.12 mean that H_4 is much smaller than H_1, and so for charge scattering away from the absorption edge it is only the H_1 term we need to consider. Although it will not be demonstrated here, evaluation of $< \beta \mid H_1 \mid \alpha >$ reveals the expected polarisation dependence of Thomson scattering as $\boldsymbol{\epsilon}' \cdot \boldsymbol{\epsilon}$. Evaluating the H_4 term, which includes a spin com-

ponent demonstrates the case for non-resonant magnetic scattering, which has a different polarisation dependence, given by $\boldsymbol{\epsilon}' \times \boldsymbol{\epsilon}$. Considering now only the case of resonant scattering, it is the H_2 term that is dominant [44]. This arises as any expansion of $e^{-i\mathbf{k}\cdot\mathbf{r}}$ terms decreases fairly quickly for core levels. Upon evaluation of the H_2 and H_3 integral, the first non-vanishing term for the H_2 component is much larger than the H_3 component, and so only the H_2 component is required. Returning to equation 1.17 it is also necessary to include the extra term $\frac{i\Gamma_n}{2}$ in the denominator, where Γ gives the lifetime of the excited state [47]. This is necessary, as the intermediate states are not static.

Using the H_2 term and applying the annihilation and creation operators, we may then write

$$W = \frac{2\pi}{\hbar}\Big|\left(\frac{hc^2}{V\omega_{\mathbf{k}}}\right)\left(\frac{e}{mc}\right)^2 \sum_n \frac{< 0 \mid \sum_j \bar{\boldsymbol{\epsilon}}' \cdot \mathbf{p}_j e^{-i\mathbf{k}'\cdot\mathbf{r}_j} \mid n >< n \mid \sum_{j'} \bar{\boldsymbol{\epsilon}} \cdot \mathbf{p}_{j'} e^{i\mathbf{k}\cdot\mathbf{r}_{j'}} \mid 0 >}{E_0 - E_n + \hbar\omega_{\mathbf{k}} + \frac{i\Gamma_n}{2}}\Big|^2 \delta(\hbar(\omega_{\mathbf{k}} - \omega_{\mathbf{k}'})). \tag{1.18}$$

The final step we will show here is the application of the dipole approximation. That is, when $e^{i\mathbf{k}\cdot\mathbf{r}}$ is expanded as

$$e^{i\mathbf{k}\cdot\mathbf{r}} \approx 1 + i\mathbf{k}\cdot\mathbf{r} - \frac{(\mathbf{k}\cdot\mathbf{r})^2}{2} + ... \tag{1.19}$$

the latter terms quickly decrease, as $\mathbf{k}.\mathbf{r}$ is small for core levels. The dipole approximation requires that we simply take the first term in the expansion. Finally, since $[\mathbf{r}, H_{elec}] = \frac{i\hbar\mathbf{p}}{m}$ when H_{elec} is of the form $H_{elec} = \frac{\mathbf{p}^2}{2m} + V$ we can write

$$W = \frac{2\pi}{\hbar}\Big|\left(\frac{hc^2}{V\omega_{\mathbf{k}}}\right)\left(\frac{e}{mc}\right)^2\left(\frac{im}{\hbar}\right)^2 \sum_n \frac{< 0 \mid \sum_j \bar{\boldsymbol{\epsilon}}' \cdot [\mathbf{r}_j, H_{elec}] \mid n >< n \mid \sum_{j'} \bar{\boldsymbol{\epsilon}} \cdot [\mathbf{r}'_j, H_{elec}] \mid 0 >}{E_0 - E_n + \hbar\omega_{\mathbf{k}} + \frac{i\Gamma_n}{2}}\Big|^2 \delta(\hbar(\omega_{\mathbf{k}} - \omega_{\mathbf{k}'})) \tag{1.20}$$

which gives

$$W = \frac{2\pi}{\hbar}\Big| \left(\frac{hc^2}{V\omega_{\mathbf{k}}}\right)\left(\frac{e}{mc}\right)^2\left(\frac{im}{\hbar}\right)^2 (E(n)-E(0))^2 \sum_n \frac{< 0 \mid \sum_j \bar{\boldsymbol{\epsilon}}' \cdot \mathbf{r}_j \mid n >< n \mid \sum_{j'} \bar{\boldsymbol{\epsilon}} \cdot \mathbf{r}'_j \mid 0 >}{E_0 - E_n + \hbar\omega_{\mathbf{k}} + \frac{i\Gamma_n}{2}}\Big|^2 \delta(\hbar(\omega_{\mathbf{k}} - \omega_{\mathbf{k}'})). \tag{1.21}$$

We do not proceed further, as at this stage it should be clear where the resonant scattering process originates. However, if one continues, by writing $\mathbf{r}$ in spherical coordinates, and evaluating the integral, the selection rules for a dipole transition are revealed as $\Delta l = \pm 1$. We may relate the transition probability to the differential cross-section through

$$\frac{d\sigma}{d\Omega} = \frac{W}{\Phi \Delta\Omega} \tag{1.22}$$

where Φ represents the flux incident on the sample and $\Delta\Omega$ a unit area of the solid angle.

1.5.2 Overview

To summarise where we have arrived: resonant x-ray diffraction provides an element specific probe of the electronic order within a distinct electron band, determined by the excitation energy. The dipole terms are generally the dominant terms, and the transitions allowed from core to valence levels are those of the form $\Delta l = \pm 1$. As will be discussed shortly, the dipole operator must be expressed as a tensor [46, 48, 49] of rank 2, and so information regarding the anisotropy of the electron distribution around the resonating site can also be gleaned, by studying the unique polarisation dependencies and complex energy spectra. This is a capability which is not available with neutron or alternative x-ray techniques (excluding other near-edge techniques such as EXAFS and XANES).

It is easy to overlook the most exploited advantage of resonant scattering though, which is the enhancement itself, allowing weak signals to be observed above background. The evaluation of the integral, which comes from equation 1.21, reveals that a larger signal is observed when there is a more significant overlap (in space)

between the core states and the valence states we excite in to. With regard to this thesis, this explains why a large resonant enhancement is available when performing soft x-ray experiments at the iron $L_{2,3}$ edges where the dipole transition consists of an excitation from the $2p$ to the $3d$ states. This is particularly useful of course, as it is the $3d$ band in which the valence electrons lie in iron and manganese. As will be shown, the resonant enhancement is far less impressive at the iron K edge, where the dipole transition consists of an excitation from the $1s$ to $4p$ states.

1.5.3 Resonant Scattering Contributions

In the previous section the dipole approximation was used to show that the dipole-dipole (referred to as E1-E1) component is the dominant term, as the value of $\mathbf{k} \cdot \mathbf{r}$ is small. However, higher terms can not always be neglected and multipolar contributions can be significant. Rather than consider expressions of the form used in equations 1.18, 1.20 and 1.21 it is more convenient to consider the total scattering amplitude $f(\boldsymbol{\epsilon}, \boldsymbol{\epsilon}')$, which is effectively the atomic form factor without the explicit $\mathbf{Q}$ and $\hbar\omega$ dependencies. Up to the quadrupole-quadrupole (E2-E2) component this gives [49]

$$\begin{aligned} f(\boldsymbol{\epsilon}, \boldsymbol{\epsilon}') &= \boldsymbol{\epsilon} \cdot \boldsymbol{\epsilon}' f^0 + \sum_{m,n} \epsilon_m \epsilon'_n \hat{S}^0_{mn} \\ &- i \sum_{m,n,o} \epsilon_m \epsilon'_n (k_o - k'_o) \hat{T}^0_{mno} \\ &+ \sum_{m,n,o,p} \epsilon_m \epsilon'_n k'_o k'_p \hat{U}^0_{mnop} + ... \end{aligned} \tag{1.23}$$

where f^0, $\hat{S}$, $\hat{T}$ and $\hat{U}$ represent tensors of rank 0, 2, 3 and 4; m, n, o and p correspond to the indices of the tensors and where $\boldsymbol{\epsilon}$ and $\boldsymbol{\epsilon}'$ again represent the incident and scattered polarisation states of the photon. These tensors are the sum of the individual tensors which correspond to each resonating site. In accordance with Neumann's Principle each of these tensors must possess the same symmetry as the site of the atom. Furthermore, for charge scattering the tensors must be symmetric,

and for magnetic scattering the tensor must be anti-symmetric, as a manifestation of the time reversal symmetry breaking. At the K edge of the $3d$ transition metals, the $\hat{S}$ term corresponds to a dipole transition into the $4p$ band, due to the dipole selection rule $\Delta l = \pm 1$. The $\hat{U}$ term corresponds to a quadrupolar transition, and so has different selection rules, specifically $\Delta l = 0, \pm 2$. In this case this corresponds to a transition to the $3d$ band. The $\hat{T}$ term corresponds to the mixed dipole-quadrupole terms, which in this case are due to the mixing of the d and p states, for example by hybridising with an adjacent ion [50]. The term f^0 corresponds to the non-resonant Thomson contribution, which generally dominates the scattering unless it is symmetry forbidden.

We note at this point that it is the difference in the scattering factors between sites that we are sensitive to on resonance. Thus for sites that possess high symmetry, a weaker signal will typically be observed than for the case of low symmetry. Specifically it is the contrast between the density of states, which we are sensitive to, hence the ability of RXD to directly probe electronic order, rather than just the structural distortion.

The E1-E1 ($\hat{S}$) term is the dominant resonant component, which can be further separated into unique components (which can lead to added confusion due to the nomenclature used). These terms are often referred to as the monopole, dipole and quadrupole contributions, and are the three terms represented in the famous formalism of Hannon *et al.* [45] for the scattering amplitude, equation 1.24,

$$f(\boldsymbol{\epsilon}, \boldsymbol{\epsilon}')_{E1-E1} \propto [\boldsymbol{\epsilon}' \cdot \boldsymbol{\epsilon} F^{(0)} - i(\boldsymbol{\epsilon}' \times \boldsymbol{\epsilon}) \cdot \mathbf{z} F^{(1)} + (\boldsymbol{\epsilon}' \cdot \mathbf{z})(\boldsymbol{\epsilon} \cdot \mathbf{z}) F^{(2)}]. \quad (1.24)$$

Here $\mathbf{z}$ gives the angular momentum quantisation axis, while the F terms represent the monopole (0), dipole (1) and quadrupole components. When written in full, each of these terms contain different combinations/components of the sum in equation 1.21, when written in spherical coordinates. The monopolar component is the (resonant) isotropic charge order term, the dipolar contribution results in magnetic scattering, and the quadrupolar term is sensitive to any further anisotropy [44, 45, 51]. All three terms are parity even, while only the monopolar

and quadrupolar terms are even under time reversal symmetry. In practice it is often convenient to represent all of these terms as the matrix $\hat{S}$ as in equation 1.23, while preserving the required symmetry of each term. We note at this point that going beyond the dipole approximation, and considering the E1-E2 and higher terms allows other multipolar terms to be studied, such as the magnetic toroidal moments.

We must now acknowledge an important point, as we must remark that (even without superlattice order) the crystal structure can still produce resonant reflections. In practice this is generally irrelevant for allowed Bragg reflections, as the non-resonant component dominates. However, in cases where Bragg reflections are forbidden by compound symmetry operations (screw axis and glide planes) the tensorial components can still be allowed. The result, known as Templeton-Templeton [49] or ATS (Anisotropy of the Tensor of Susceptibility) [48] scattering produces reflections from the crystal structure which can display complex polarisation dependencies. This phenomena has been observed in a large number of materials, ranging from the original and ongoing studies of potassium chromate [49, 52] to room temperature magnetite [53] to germanium [54] and many more. One important example of ATS scattering which must be addressed, is those cases where ATS has been observed, and attributed to orbital ordering. In the manganites this originally related to the studies by Murakami *et al.* [47, 55], who claimed to directly observe orbital order in the cubic and monolayer (La,Sr) half-doped manganites, see figure 1.11. However, it was later demonstrated by Benfatto *et al.* that the observed signal is due to the degeneracy of the $4p$ band being lifted by distorted octahedra [56]. Indeed, in such a situation the measurement is rather of ATS scattering which results from the anisotropy of the Jahn-Teller distortion to the crystal structure. This is generally the problem when the excited transition does not probe the electron band in which the orbital order takes place, but rather some delocalised band: as is the case when tuned to the K edge of all but the lightest elements.

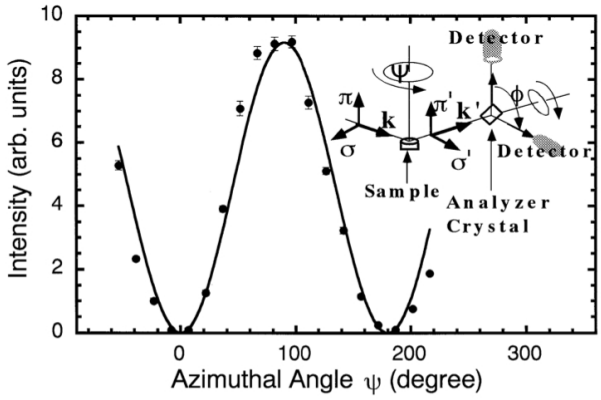

Figure 1.11: Azimuthal dependence at the *orbital order* wavevector, demonstrating the expected behaviour, by Murakami *et al.* Reprinted figure with permission from reference 47. Copyright 1998 by the American Physical Society.

1.5.4 Simulation

The simulation of resonant x-ray spectra can be achieved using several different approaches, however in this thesis the FDMNES code is used [57]. The code, Finite Difference Method for Near Edge Spectroscopy (FDMNES) was initially developed for XANES (X-ray Absorption Near Edge Spectroscopy) but has since been extended to the related field of resonant diffraction. At its heart FDMNES uses Density Functional Theory (DFT), by applying the Local Spin Density Approximation (LSDA) to solve the Schrödinger equation. The electronic properties of the system are determined by a functional which represents the electron density. It is then the value of this density at any point which determines the electron interactions. FDMNES does not solve this over an infinite crystal, but rather over a cluster of atoms, with a maximum radius of $\sim$ 10 Å. This cluster is centred around the resonating atom, as it is the local structure around this site which determines the electronic environment of the ion. A potential must be chosen, and at this point FDMNES offers two options: the finite difference method may be employed, or a muffin-tin potential may be used. The former method establishes a grid of points throughout the cluster, with each point possessing a specifically determined

potential. The latter method uses a spherically symmetric potential up to some radius around an atom, with a constant value being used beyond the radius, between spheres. This latter method requires multiple scattering theory, *i.e.* it calculates how an electron wave is scattered by the muffin-tin potentials around the resonating site. It is found that for the type of calculations presented here, using multiple scattering (MS) theory produces results similar to using the finite difference method (FDM). Due to the greatly increased speed in calculations using MS rather than FDM, the code is run in MS mode throughout the calculations presented in this thesis. Separate clusters around each inequivalent resonating atom are generated, with each producing a separate energy dependence. The final part of the calculation convolutes these individual spectra together, producing the resonant spectrum. Finally it is important to point out that FDMNES regards the scattering process as mono-electronic, and so works significantly better when the intermediate state is non-localised. In regard to the iron and manganese compounds studied here, this means that the simulations are only accurate for the iron and manganese K edges.

1.6 Summary

In summary, we have provided a concise description of x-ray scattering, and specifically resonant x-ray diffraction (RXD). RXD is a powerful approach for solving the subtleties of crystal structures. The ion and band selectively provided by exciting a specific electronic transition can be highly rewarding. However, the technique can also be problematic. Resonant scattering experiments are technically difficult, as many of the signals are weak despite the resonant enhancement, and because all variables and experimental conditions must be known and accurately controlled. These difficulties are amplified in the soft x-ray regime, where the experiment must be carried out under ultra high vacuum, and the sample can not be aligned using Bragg reflections once inside the diffraction chamber. However, the principle problem regarding RXD studies is the shear volume of information that can potentially be probed. As we have shown, even in the dipole approximation the scattering pro-

cess is sensitive to charge and magnetic ordering, as well as orbital and structural anisotropies. Nevertheless, through careful analysis, using cutting-edge simulation codes, the components can be disentangled, leading to a greater understanding of the material.

Chapter 2

Magnetite, Fe_3O_4

2.1 Background

Magnetite, Fe_3O_4, is the oldest known magnetic solid, with curiosity in the material dating back to the discovery of lodestone and its magnetic properties [58]. Yet, despite its long history, a number of mysteries still surround it, with recent studies suggesting magnetite may even be multiferroic [59]. At room temperature the material is well understood: magnetite is a poor metal, ferrimagnetic, and has an inverse spinel structure, with Fe ions sitting at tetrahedral (A) and octahedral (B) coordinated sites, figure 2.1. The structure is cubic, with space group $Fd\bar{3}m$ (No. 227) and $a_C = 8.394$ Å. The chemical formula is often written as $Fe^{3+}[Fe^{2+}Fe^{3+}]O_4$ to highlight the mixed valence nature. Here, the first term corresponds to Fe^{3+} ions in tetrahedrally coordinated sites, and the second term to Fe^{2+} and Fe^{3+} ions in octahedrally coordinated sites. These octahedral sites have no long range charge order, and the charge fluctuates, with an average valence of $2.5+$ for each octahedral site. The magnetic structure also represents the classic example of a ferrimagnetic system, as the tetrahedral and octahedral sublattices are each ferromagnetically aligned along the $[1\ 1\ 1]$ axis, but antiferromagnetically aligned with respect to each other.

Upon cooling below $\sim$120 K the system undergoes a sharp first-order phase transition, accompanied by a change in structure [60], magnetic easy axis, resistivity [61], thermal expansion [62], specific heat [63] and magnetisation [64] prop-

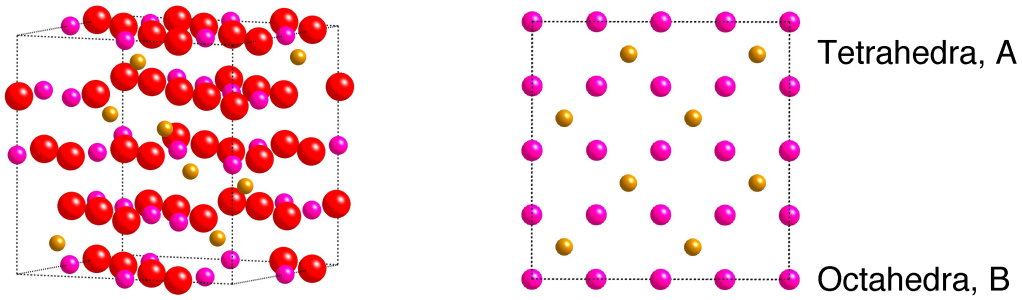

(a) (b)

Figure 2.1: The room temperature structure of magnetite, featuring sixteen octahedrally coordinated irons (pink) and eight tetrahedrally coordinated irons (orange). The oxygen atoms are shown in (a) in red, but are omitted in (b) for clarity. The cubic axes correspond to the dashed lines of the unit cell.

erties, as shown in figure 2.2. The temperature at which this transition occurs is very sensitive to the stoichiometry of the sample [65], with even small changes in the iron/oxygen ratio shifting the transition by several Kelvin, as shown in figure 2.3. This is referred to as the Verwey transition (T_{V}), after Verwey [7, 8], who proposed that the transition is also accompanied by a transformation to a charge ordered state, explaining the increase in resistivity of two orders of magnitude. Specifically he proposed an alternate layering along the c-axis of Fe^{2+} and Fe^{3+} ions on the octahedral iron sites, as shown in figure 2.4. It has since become clear that this pure ionic picture of charge ordering in magnetite is incorrect, although it has not stopped magnetite often being cited as the classic charge ordered system. Total ionic separation has now been demonstrated to be incorrect based on Kerr effect [66] and diffraction [26] measurements, and further supported on entropic [67] and theoretical grounds [68].

Perhaps the most surprising problem with respect to magnetite today, is that the low temperature crystal structure is still not solved, and there are indications that the structure is in fact triclinic [69]. It is clear that below T_{V} the symmetry of the crystal structure is significantly lowered, and a major step in solving the structure was achieved by Wright *et al.*, when the structure was refined as monoclinic $P2/c$ (No. 13) [70, 71]. This structure, refined using $Pmca$ (No. 57) constraints, contains

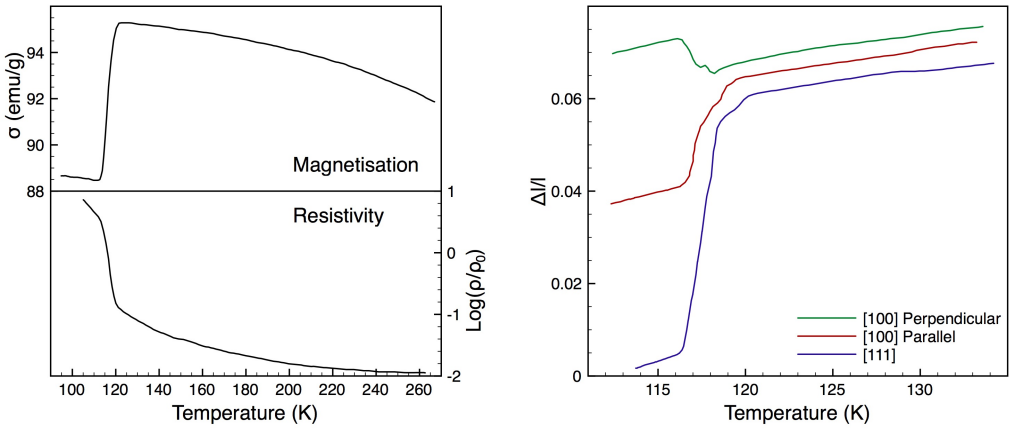

(a) (b)

Figure 2.2: (a) The anomalies in magnetisation and electrical resistivity at T_{V}. (b) Thermal expansion of magnetite around T_{V}. Figures re-drawn from reference 62 by Bickford *et al.* and references therein.

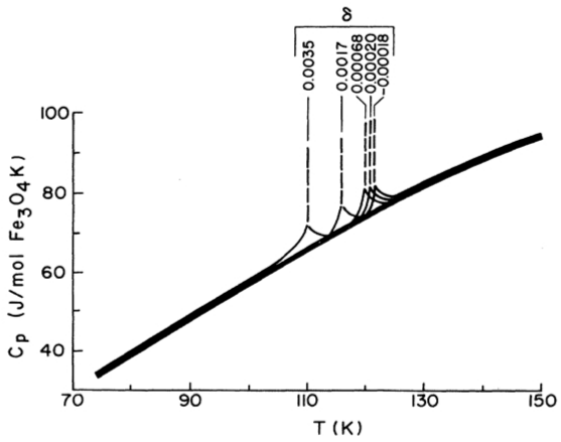

Figure 2.3: Heat capacities of several samples of $Fe_{3(1-\delta)}O_4$ measured by Shepherd *et al.* Reprinted figure with permission from reference 65. Copyright 1991 by the American Physical Society.

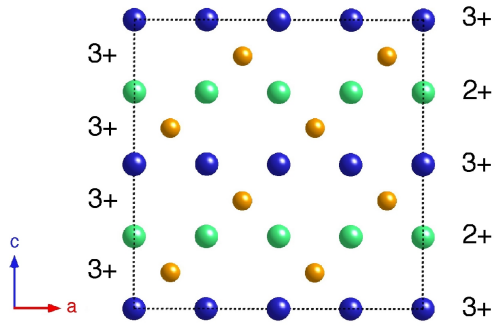

Figure 2.4: Verwey's model for charge ordering in magnetite, featuring alternate layers of Fe^{2+} (green) and Fe^{3+} (blue) ions at the octahedral sites.

six inequivalent B sites; however, even in the simpler orthorhombic $Pmca$ structure there are still four inequivalent octahedral sites, as well as two inequivalent tetrahedral sites. The lowest symmetry refinement to date uses a monoclinic Cc (No. 9) structure [72], which contains sixteen independent octahedral sites and eight independent tetrahedral sites. The monoclinic distortion away from $Pmca$ symmetry is small, and so this orthorhombic structure with lattice parameters $a_O = 5.944$ Å, $b_O = 5.924$ Å, $c_O = 16.775$ Å remains a popular choice, figure 2.5. However, when indexing reflections we will use the cubic structure for simplicity, unless otherwise stated.

The most debated problem in Fe_3O_4 regards the charge and orbital structures of magnetite. While it has become clear that Verwey's initial model is not correct [26, 66–68], debate still continues as to the correct arrangement and magnitude of the charge disproportionation (see *e.g.* [26, 70, 73, 74]). Bond valence sum (BVS) calculations [70] and RXD studies [26] have suggested a valence of approximately 2.6+ for the B2 and B3 sites, and 2.4+ for the B1 and B4 sites, while other studies [74] have suggested the disproportionation must be below $0.1\ e^-$. Theoretical studies [68] support a segregation of $0.7\ e^-$ within the t_{2g} band, but due to screening the total charge difference between sites is $\approx 0.23\ e^-$. Numerous experimental and theoretical studies (*e.g.* [68, 70]) have concluded that the charge ordering wavevector is $(0\ 0\ 1)_C$ with an additional minor modulation of $(0, 0, \frac{1}{2})_C$. However, an extra

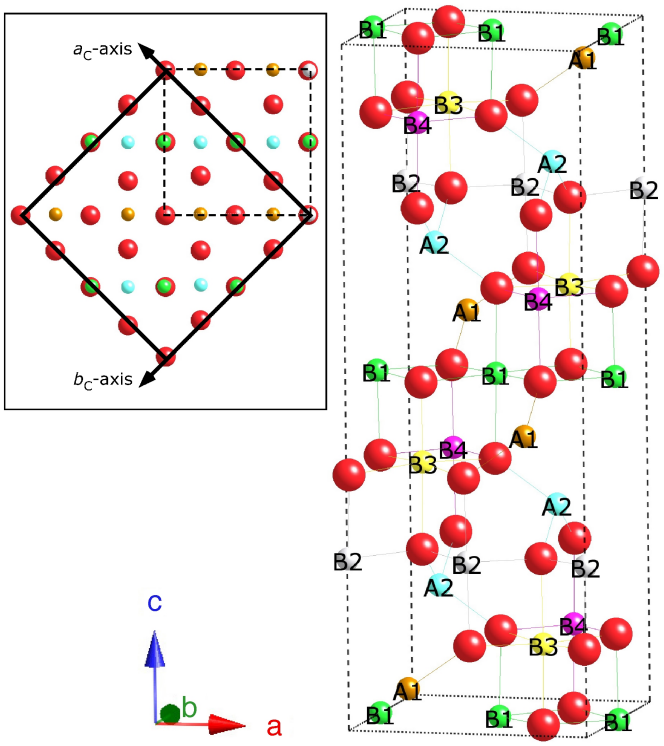

Figure 2.5: The simplified low temperature structure of magnetite, in the orthorhombic $Pmca$ refined unit cell. Fe^{3+} ions sit at tetrahedral A sites while charge ordering takes place over the four inequivalent octahedral B sites. Oxygens sit at the corners of the polyhedra. In the $P2/c$ cell there are six inequivalent B sites. The inset shows the view along the c-axis, showing the high temperature cubic cell as a solid black line, and the orthorhombic cell as a dashed line.

level of complexity is then added when the possibility of orbital order is included [67, 68, 75]. Below $T_{\rm V}$ there is a small trigonal distortion which effects the nearest-neighbour atomic environment. The electronic structure is split from that shown in figure 1.8, as the degeneracy of the t_{2g} orbitals (triplet) is lifted into a singlet (a_{1g}) and a doublet (e_g). The singlet is slightly lower in energy, and so represents the ground state; however, this does not rule out orbital ordering, as the 150 meV gap [76] between the singlet and the doublet is much smaller than the bandwidth of the t_{2g} band. The complete a_{1g} and e_g basis must instead be considered, allowing the possibility of orbital order within the t_{2g} band [66]. Recent calculations have indicated that orbital ordering takes place below $T_{\rm V}$. LSDA + U [66, 68] and GGA + U [67] calculations predict orbital ordering with orbital unit cells the same size as the crystal unit cells used in the simulations, that is the $P2/c$ and Cc cells respectively. These orbital structures are shown in figure 2.6. In the case of figure 2.6(a), we note that although the structure shown is only one cubic length along the c-axis, the (0, 0, $\frac{1}{2}$)$_C$ modulation is present, as the B3 and B4 positions swap over the next cubic unit. In both the Leonov and Jeng structures, the B1 sites possess mainly d_{xz}/d_{yz} character while the B4 sites have mainly d_{xy} character, with respect to the cubic basis. This information is summarised in table 2.1, where we see that the B2 and B3 sites make only minimal contributions to the t_{2g} orbital order, while the B1 and B4 sites have a clear orbital preference.

Recently both hard [77] and soft [78, 79] x-ray resonant diffraction experiments have claimed to observe orbital ordering in magnetite, at a wavevector of (0, 0, $\frac{1}{2}$)$_C$.

Table 2.1: Occupation of the most populated t_{2g} minority orbitals of the iron B sites, calculated within the $P2/c$ structure. Table adapted from reference 68.

Site	Orbital (in cubic frame)	Occupation (no. of e^-)
B1	d_{xz}/d_{yz}	0.76
B2	-	0.09
B3	-	0.09
B4	d_{xy}	0.80

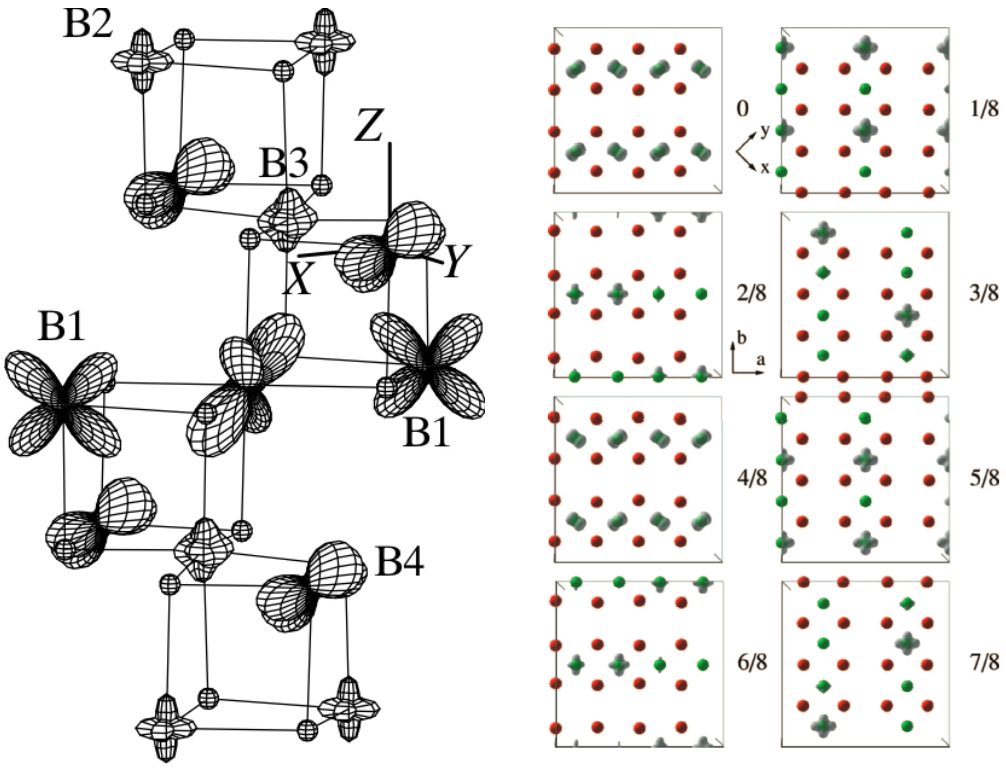

(a) (b)

Figure 2.6: (a) Charge and orbital structure predicted by Leonov *et al.* The extension along the c-axis shown represents one cubic unit cell length, which is half as long as the $P2/c$ and Cc unit cell. Figure from reference 68. (b) Orbital structure predicted in the t_{2g} band for the Cc structure by Jeng *et al.* The red and green spheres represent oxygen and iron atoms respectively. The crystallographic (Cc) axes are given by a and b, while cross-sections are shown along the c-axis. Reprinted figures with permission from references 68 and 67 respectively. Copyright 2004 and 2006 by the American Physical Society.

In the former hard x-ray study the argument for orbital ordering comes from a gradual second-order, rather than a first-order, transition at T_{V} for the half-integer reflections. This is not seen for the integer-type reflections, see figure 2.7, and so Lorenzo *et al.* argue that there is an additional order parameter in action, beyond the charge and structural effects. The widths of the reflections attributed to orbital order also appear considerably larger than the charge order reflections, as shown in figure 2.8.

Soft x-ray experiments have also claimed that the half-integer reflections are the result of orbital order, based on simulations of the spectra using an orbitally ordered model. However, an additional soft x-ray study has demonstrated that the experimental results can be simulated equally well when orbital order is not considered, and see no sign of a gradual transition at T_{V}, figure 2.9 [80].

In order to address these issues surrounding observations of charge order and orbital order, we performed an RXD experiment on a high quality, single crystal of magnetite, subjecting the sample to full polarisation analysis of the diffracted signal. It was our intention to see what RXD could truly tell us about the electronic structure of magnetite by applying a simple charge order model and the most accurate crystallographic structure.

2.2 Sample Preparation

The sample was a synthetically produced crystal of Fe_3O_4, grown using the floating zone method in an image furnace [81]. This method produces high purity crystals, as only a small section of the crystal is kept molten, which is then drawn along the boule. This leaves highly pure material in the cooled region, preserving impurities in the melt. Specific heat measurements, figure 2.10, were performed by using a small specimen of magnetite obtained from the same growth boule as used for the scattering experiments. These measurements, performed on a Quantum Design Physical Property Measurement System, revealed the Verwey transition to be at 120.4 ± 0.3 K with the transition peak possessing a full-width at half-maximum of ≈ 3 K, and an entropy of transition (ΔS_{V}) of 5.8 ± 0.3 J/mol K. This is a lower

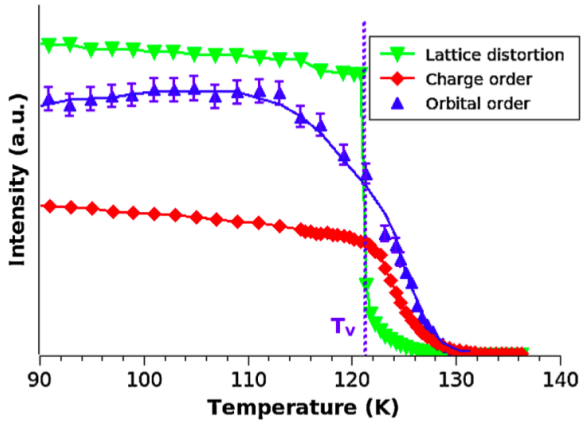

Figure 2.7: Temperature dependencies of the $(0\,0\,3)_C$ (green triangles), $(0\,0\,1)_C$ (red diamonds) and $(0,\,0,\,\frac{2n+1}{2})_C$ (blue triangles) reflections in magnetite, at 7.119 keV measured by Lorenzo *et al.* Reprinted figure with permission from reference 77. Copyright 2008 by the American Physical Society.

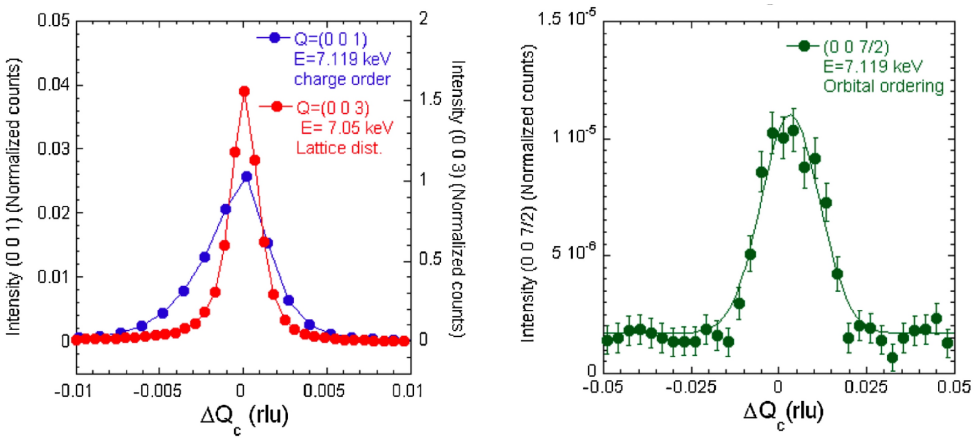

(a) (b)

Figure 2.8: Widths of several reflections in magnetite at 50 K, measured at 7.119 keV by Lorenzo *et al.* Reprinted figures with permission from reference 77. Copyright 2008 by the American Physical Society.

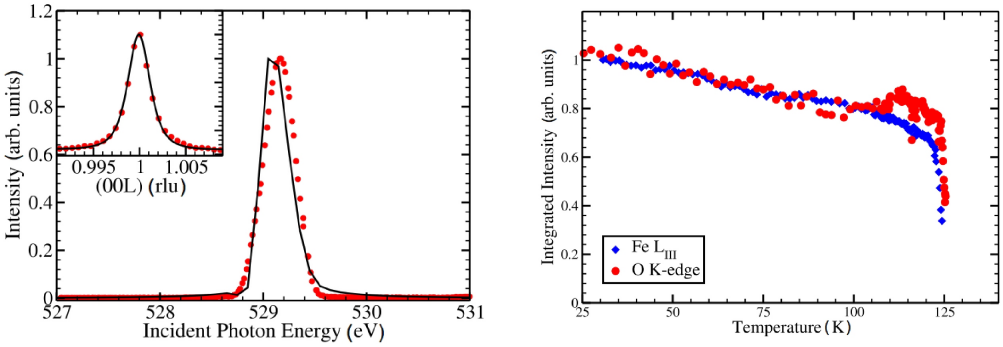

(a) (b)

Figure 2.9: (a) Energy scan of the (0, 0, $\frac{1}{2}$)$_C$ reflection in magnetite, measured around the oxygen K edge [80] at 30 K. Inset: Reciprocal space scan of the (0, 0, $\frac{1}{2}$)$_C$ reflection, indexed in the orthorhombic setting. (b) Temperature dependence of the (0, 0, $\frac{1}{2}$)$_C$ reflection at the oxygen K edge and iron L_3 edges by Wilkins *et al.* Reprinted figures with permission from reference 80. Copyright 2009 by the American Physical Society.

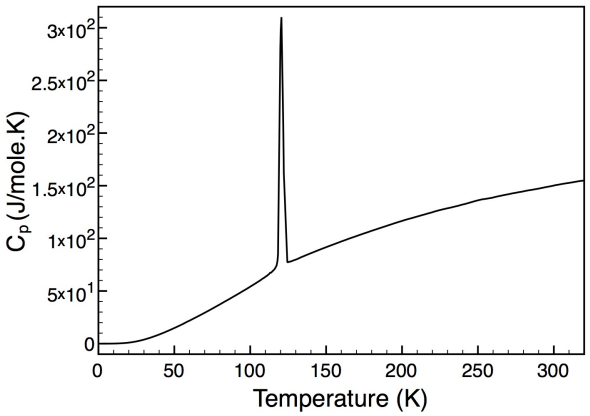

Figure 2.10: The heat capacity of magnetite, clearly showing the phase transition at T_V.

Verwey transition temperature than the value reported by Kim-Ngan *et al.* [82] of 123.5 K for a stoichiometrically correct sample, which displayed a heat capacity peak width of 0.2 K and ΔS_{V} of 6.4 J/mol K. However, despite the differences in transition temperatures and ΔS_{V} it is clear that the sample was well within the first-order transition region [65, 83] (given by $\delta < 0.0012$, where $\mathrm{Fe}_{3(1-\delta)}\mathrm{O}_4$) and with purity above $\delta \leq 0.0007$.

The crystals were pre-aligned using a rotating anode x-ray source with a four-circle diffractometer. The $\langle 0\ 0\ 1 \rangle_C$ axis was prepared to be surface normal, before being polished using diamond suspensions. The primary sample used at ID20 (see below) was polished in several stages, eventually using a $0.1\ \mu\mathrm{m}$ diamond suspension, so that the sample could also be used for soft x-ray scattering experiments. Such experiments are very dependent on the surface preparation, as the penetration depth for soft x-rays is only several hundred Ångströms. The second sample, used solely on the hard x-ray beamline XMaS (see below), did not require such fine preparation and was polished to $3\ \mu\mathrm{m}$. During the first experiment on ID20 a ~ 0.3 T SmCo magnet, in the shape of a disc measuring ≈ 5 mm in diameter and ≈ 5 mm high, was attached to the magnetite crystal using a layer of silver paint. The field was applied along one of the $\langle 0\ 0\ 1 \rangle_C$ axes to fix and uniquely define the monoclinic c-axis on cooling through T_{V} [84]. In the second experiment on ID20 a stronger NdFeB magnet was used, measuring approximately the same size as the SmCo magnet, but with a field of ~ 0.5 T at the surface. The magnetite samples were small discs, with diameters of ≈ 4 mm and heights of ≈ 2 mm; however, a small segment was removed from the second sample prior to the experiment so that supplementary measurements could be performed.

The following results have previously been published in references 85 and 86.

2.3 Experimental Technique

This experiment was carried out on the beamline ID20 at the ESRF (European Synchrotron Radiation Facility), a beamline which is principally used for magnetic

diffraction. The ESRF is a 6 GeV machine, and so is an ideal source of hard x-rays. The beamline normally uses two undulators (up to three are available) to produce a highly intense, horizontally polarised x-ray beam with a tuneable energy between 3 and 30 keV. A double-bounce silicon (111) monochromator acts to produce a monochromatic beam with a resolution of up to $\approx$1 eV, with the second crystal used for horizontal focussing. Additional mirrors are used for vertical focussing, resulting in a spot size which is approximately $200\ \mu$m $\times\ 100\ \mu$m, with the broader and more divergent component being in the horizontal plane. The mirrors, which operate on the principle of total external reflection, also act to suppress higher harmonics as the critical angle is larger [87] for higher energies. The $4 + 1$-circle diffractometer installed in the first experimental hutch was used, figure 2.11(a). This provided the standard θ, 2θ, χ and ϕ motions, plus an additional rotation capable of increasing θ to higher angles without obstructing the incident beam with the χ circle. A Displex cryostat was used, which is capable of reaching temperatures of $\approx\ 10$ K when a radiation shield is used. However, as the region of interest was $\approx\ 120$ K a radiation shield was not used, and the sample was mounted beneath a single beryllium dome to minimise absorption.

For this experiment the synchrotron was operated in *16 bunch mode*, meaning the storage ring contained 16 equally spaced electron bunches with a current in the ring of 90 mA, rather than the maximum of 200 mA which the ESRF most frequently operates at (although in several different modes) [88]. The detector was an avalanche photodiode (APD) which operates as a photodiode under an applied reverse bias. This bias increases the voltage barrier, impeding current flow. However, with a large enough voltage an avalanche effect will occur, whereby electrons which are turned into mobile carriers through the absorption of photons are accelerated, liberating more electrons through collisions with atoms. For part of the experiment, a diamond phase plate was inserted in the beam, figure 2.11(b). The phase plate operates on the principles of dynamical diffraction in perfect crystals, *i.e.* the wave-crystal interaction is considered using a periodic potential, and multiple scattering and non-elastic interactions are not ignored. Here, close to a Bragg

reflection a phase shift is introduced between orthogonal polarisation components. The phase shift depends on the phase plate thickness and critically on the distance from the Bragg reflection (typically several arcminutes), and so arbitrary polarisations can be generated. The most useful of these are circular [89] and linear [90] polarisations. However, because the beam is neither perfectly collimated or perfectly monochromatic, depolarisation can occur [91]. This can be reduced by using a thicker phase plate, but with the added cost of increased absorption. By rotating the phase plate around the incident/exit beam, the linear polarisation can be rotated, as is shown schematically in figure 2.12. For this experiment a $720\ \mu\mathrm{m}$ diamond crystal was used, diffracting near the (111) reflection, acting as a half-wave plate. The result was a linear polarisation of between $\approx$ 90-100% for the incident beam. An MgO (2 2 2) analyser crystal was used for polarisation analysis of the scattered beam. The analyser leakthrough between orthogonal channels was measured to be very small, at $\sim 0.92\%$, for the energies used.

Additional measurements were taken on XMaS (X-ray Magnetic Scattering), a British beamline at the ESRF [92]. XMaS uses a bending magnet source to produce x-rays, and so is significantly less intense and more horizontally divergent than ID20. The beamline is equipped with a set of mirrors for harmonic rejection, and a six-circle diffractometer, operated in four-circle vertical scattering geometry. An MgO (222) analyser was again used, as was a Displex cryostat without a radiation shield, giving a base temperature of ≈ 20 K. The detector was a (Bicron) scintillator detector, which operates through the use of a NaI(Tl) scintillator crystal. When an x-ray photon is absorbed by the scintillator crystal, a photon is emitted in the optical region. This photon then strikes a photo-cathode, a negatively charged material which can emit an electron through the photoelectric effect. The liberated electron is then accelerated toward a positively charged electrode, freeing other electrons when it collides. This process is repeated for other charged electrodes producing a measurable pulse. The synchrotron was operated in *hybrid mode*, meaning the storage ring contained 24 groups of bunches plus one single bunch, with a current of 200 mA in the ring [88].

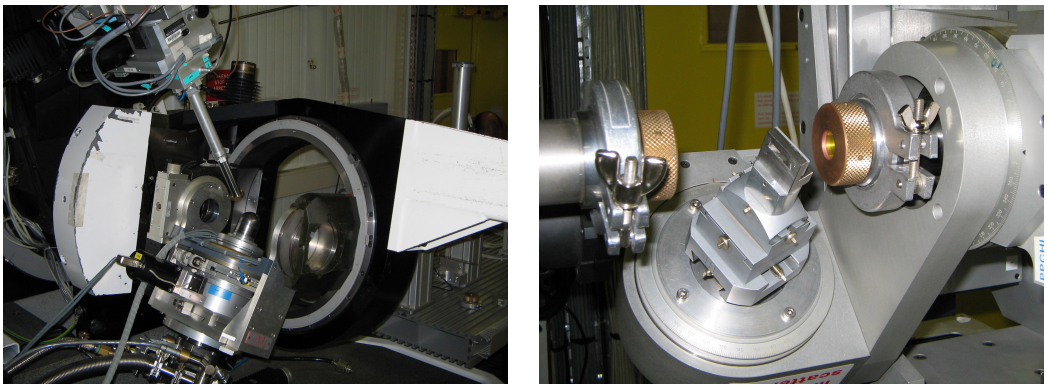

(a) (b)

Figure 2.11: (a) The $4 + 1$-circle diffractometer in the first experimental hutch at ID20. (b) The original phase plate installation at ID20.

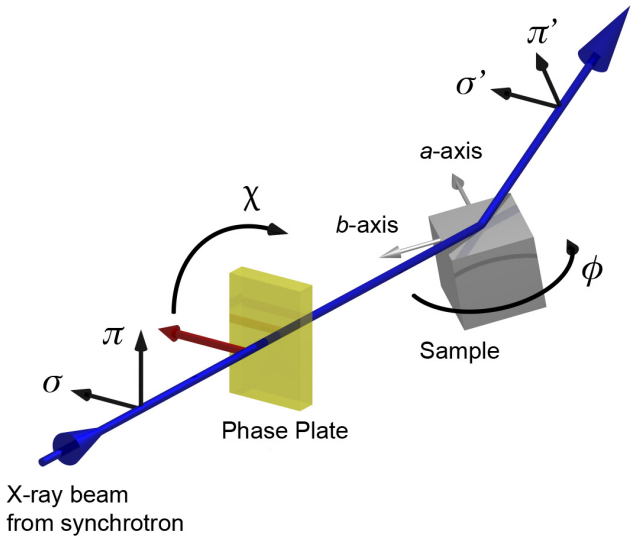

Figure 2.12: The rotation of the phase plate χ angle causes a rotation of the incident polarisation (dark red arrow) by $2 \times \chi$. The Bragg angle of the phase plate is set to zero in this figure for simplicity. The crystal is shown as it was orientated during the experiment, with $\phi = 8.4°$, when measured between the cubic a-axis and the scattered beam.

2.4 Results

After mounting the sample, the crystal was orientated in the beam, with the c-axis defined as being surface normal. The sample was then cooled to a base temperature of 20 K. The crystal was then re-aligned and the MgO (222) analyser crystal was inserted into the scattered beam and calibrated on the $(0\ 0\ 4)_C$ Bragg reflection. Several superlattice and forbidden reflections were identified close to the iron K edge, however, performing an energy scan revealed a large amount of contamination from multiple scattering (Renninger reflections) [93]. These reflections are Bragg reflections from x-rays scattered several times within a crystal, and so more reflections can be observed for crystals with large unit cells, such as low temperature magnetite. The effect of the contamination is shown in figure 2.13, where the real resonant diffraction signal is clear near the centre-right of the graph. In order to proceed with alternative measurements, an azimuth was selected at which there was a negligible contribution from multiple scattering at 7.12 keV for all reflections studied.

To identify which superlattice and forbidden reflections were present, a scan was performed along the $[0\ 0\ L]_C$ and $[1\ 0\ L]_C$ axes in reciprocal space, figure 2.14. Several cubic forbidden $(0\ 0\ odd)_C$ and half-integer reflections were clearly identified. The presence of the $(0, 0, \frac{n}{2})_C$ reflections at the iron K edge is in contrast to the previous study by Subias *et al.* [74] who also used RXD to attempt to observe these peaks. However, in our study we had an improved signal to noise ratio, of greater than three orders of magnitude, which is most likely the reason we were able to detect the half-integer reflections. Further, the initial scan along the L-axis conducted in the earlier study [74], corresponding to figure 2.14(a), was performed over the region containing the weaker superlattice reflections between $\sim(0\ 0\ 2)_C$ and $\sim(0\ 0\ 4)_C$. In that study it was concluded that the complete lack of $(0, 0, \frac{2n+1}{2})_C$ reflections, along with the lack of a resonant enhancement for the $(0, 0, 2n+1)_C$ reflections indicated that any charge segregation must be very small; with a maximum disproportionation of 0.1 e^-.

After maximising on the $(0, 0, \frac{9}{2})_C$ and $(0\ 0\ 5)_C$ reflections, their widths along

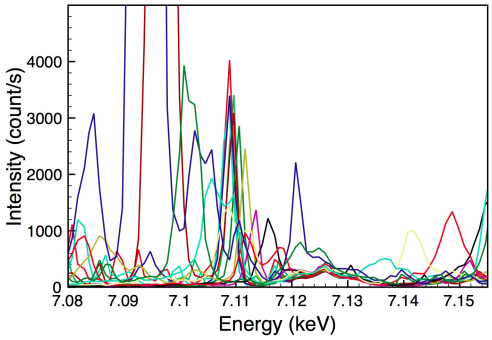

Figure 2.13: Attempted energy scans at fixed wavevector of the (0, 0, $\frac{9}{2}$)$_C$ reflection at 20 K, measured in the σ-σ' channel. Each scan (different colours) is offset consecutively by $0.5°$ in ϕ, shifting the multiple scattering reflections to different positions. Results collected on ID20, ESRF.

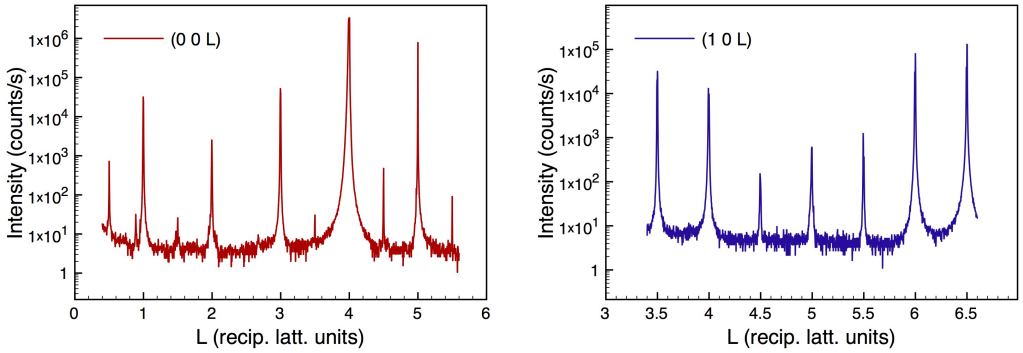

(a) (b)

Figure 2.14: Scans along (a) the L-axis and (b) the [1 0 L]$_C$-axis in reciprocal space at 20 K, tuned to 7.120 keV in the σ-σ' channel. The detector saturated whilst moving through the (0 0 4)$_C$ reflection, although supplementary scans indicated the corresponding intensity was approximately 400×10^6 counts per second. A weak (0, 0, $\frac{5}{2}$)$_C$ reflection was also located on separate scans. Results collected on ID20, ESRF.

the L-axis were measured, with both reflections having a Lorentzian squared lineshape. The reflections shown in figure 2.15 are more than an order of magnitude smaller than the (0, 0, $\frac{9}{2}$)$_C$ reflection measured in the study by Lorenzo *et al.* [77]. At 20 K we determined inverse correlation lengths of $2.94 \pm 0.04 \times 10^{-4}$ and $2.18 \pm 0.05 \times 10^{-4}$ Å^{-1} for the (0, 0, $\frac{9}{2}$)$_C$ and (0 0 5)$_C$ respectively, using equation 2.1;

$$\xi^{-1} = \frac{2\pi}{d}\Delta\mathbf{q}_{HWHM}. \tag{2.1}$$

Here, d represents the lattice spacing along the direction of measurement, and $\Delta\mathbf{q}_{HWHM}$ gives the half-width at half-maximum of the reflection in reciprocal space. This corresponds to a reduction in the correlation of e^{-1} after $7.30 \pm 0.10 \times 10^3$ Å and $9.84 \pm 0.23 \times 10^3$ Å for the (0, 0, $\frac{9}{2}$)$_C$ and (0 0 5)$_C$ respectively [94]. The (0 0 5)$_C$ peak was later found to be approximately one third broader than the (0 0 4)$_C$ Bragg reflection, indicating that the orders responsible for the additional reflections below the Verwey transition were very well correlated with respect to the crystal structure. A temperature dependence of the (0, 0, $\frac{9}{2}$)$_C$ and (0 0 5)$_C$ reflections was attempted, but due to contamination from multiple scattering, this was not possible. However, it was clear that the transition was abrupt. To measure the temperature dependence, a second crystal of the same stoichiometry, but with poorer crystallinity was studied on the XMaS beamline. The sample was located several centimetres away from the temperature sensor, resulting in a small offset of the temperature. However, figure 2.16(a), clearly shows a first-order transition for the (0, 0, $\frac{9}{2}$)$_C$ reflection, which becomes extinct at T_{V}. Similarly, the allowed (0 0 4)$_C$ Bragg reflection shows an increase in intensity at T_{V} indicating the structural phase transition is indeed first-order. The widths of the reflections shown in figure 2.16(b) also show no sign of the gradual transition observed by Lorenzo *et al.* [77]. The widths measured in figure 2.16(b) are much larger than those measured in the primary sample due to the much poorer crystallinity, *i.e.* the much smaller crystallographic domains. However, this does not change the fundamental result that the samples of magnetite studied here do not show any evidence of a second-order transition.

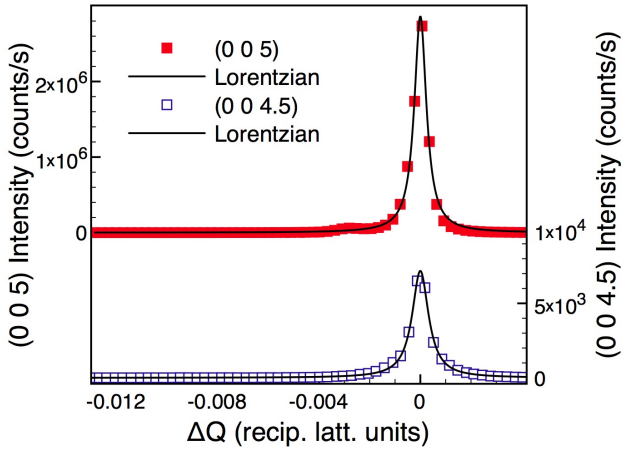

Figure 2.15: Scans along the L-axis of the (0, 0, $\frac{9}{2}$)$_C$ and (0 0 5)$_C$ reflections, tuned to 7.12 keV at 20 K in the σ-σ' channel. The peaks have been artificially shifted to the origin for ease of comparison. Both reflections show a similar width, although the (0, 0, $\frac{9}{2}$)$_C$ reflection is significantly weaker in this channel. Results collected on ID20, ESRF.

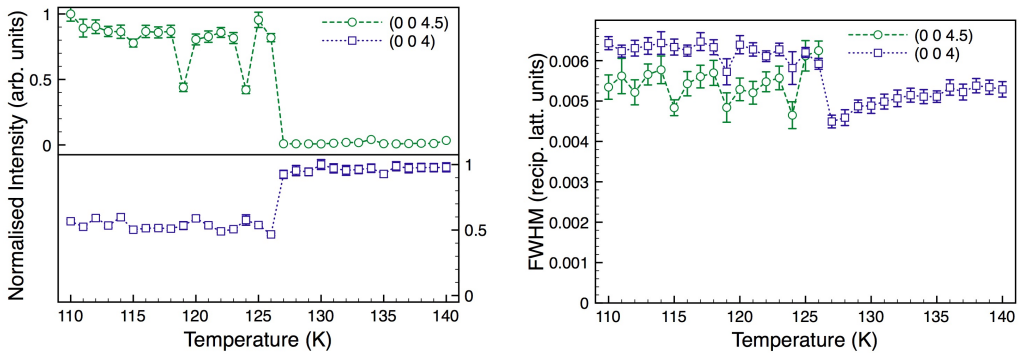

(a) (b)

Figure 2.16: Temperature dependence of the (0, 0, $\frac{9}{2}$)$_C$ and (0 0 4)$_C$ reflections, measured on warming, in the σ-π' channel. Results collected on XMaS, ESRF.

Composite energy scans were conducted by collecting standard energy scans at fixed wavevector for a large number of slightly offset azimuthal positions, as in figure 2.13. This allowed the contributions from multiple scattering and the kinematical components to be separated, as the kinematical signal appears almost identical on each successive scan. The result of this approach, combined with an absorption correction on the four reflections studied, can be seen in figure 2.17. The advantage of expressing the reflections in terms of an absorption corrected measurement is clear when we consider the $(0\ 0\ 1)_C$ and the $(0\ 0\ 5)_C$ reflections. These reflections, which are expected to be due to charge order but are also allowed reflections in the $Pmca$ and lower symmetry settings, have large non-resonant components. The result of performing the multiple scattering correction alone can be seen in figure 2.18(a). Here, the enhancement of the $(0\ 0\ 1)_C$ is still clearly visible, but the $(0\ 0\ 5)_C$ reflection is much less noticeable. At first glance the spectra before and after the absorption correction may seem quite different; however, close inspection reveals matching features with their absorption corrected counterparts. We note that the absorption correction effectively enhances the higher energy components, making some local maximums move slightly, but this is to be expected. When comparing to simulation the absorption must be accounted for at some point, either in the simulation or by experimental correction using a Bragg peak energy scan or the fluorescence, figure 2.18(b). In this case it is advantageous to perform the experimental correction in order to make the resonant spectra clearer.

To address the origin of the reflections, the standard procedure is to measure the azimuthal dependence of the reflection, while measuring the intensity in perpendicular polarisation channels, allowing any anisotropy in the reflections to be detected. However, by rotating the plane of incident polarisation rather than the sample itself, the sample may be kept stationary in the x-ray beam and the problem of contamination from multiple scattering is eliminated, while providing effectively the same information. The elimination of multiple scattering is the result of being able to select a single azimuthal orientation such that Renninger reflections at the chosen energy are excluded. Further, since the sample need not be rotated, the technique is

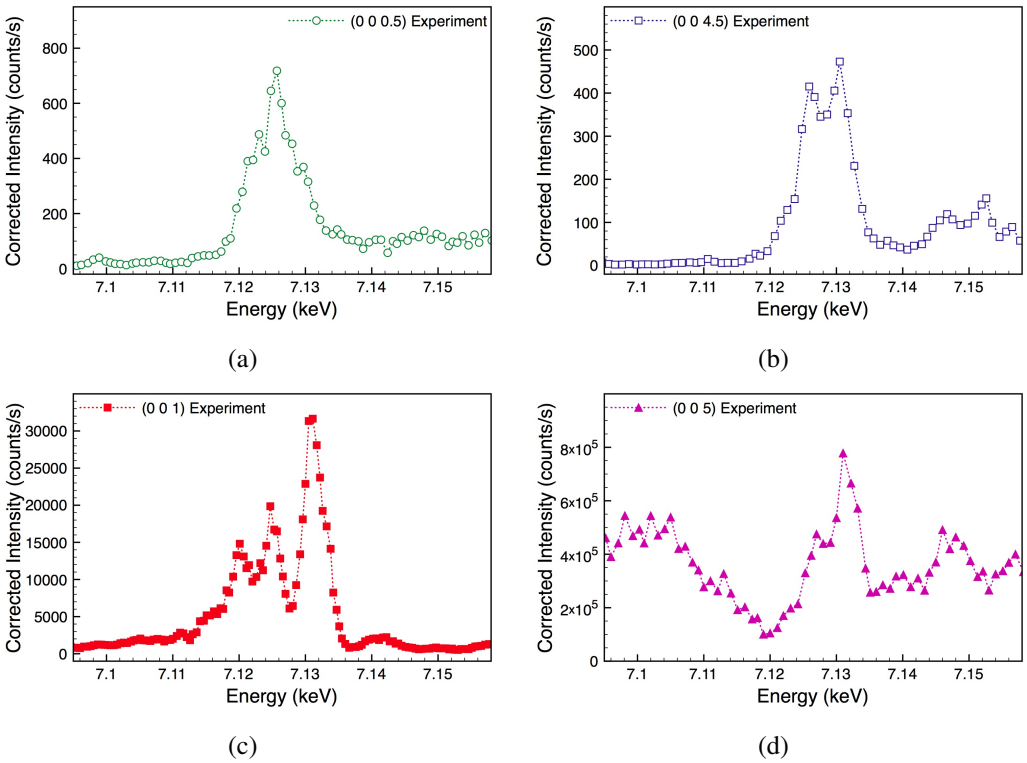

Figure 2.17: Energy scans at fixed wavevector, corrected for absorption and multiple scattering effects, measured at 20 K in the σ-σ' channel. As the data has been corrected, the intensity axis is instead scaled to concur with figure 2.14(a), for ease of comparison. Results collected on ID20, ESRF.

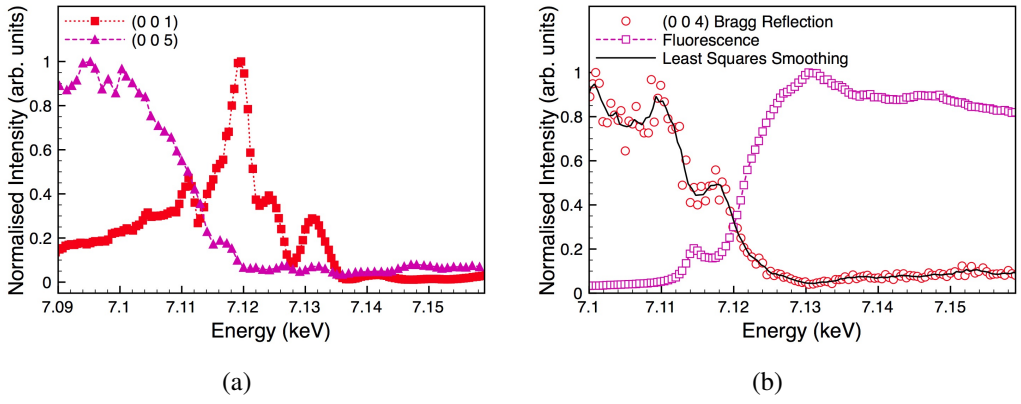

Figure 2.18: (a) Energy scans at fixed wavevector, corrected for multiple scattering effects, measured at 20 K in the σ-σ' channel. (b) Energy scan at fixed wavevector of the $(0\,0\,4)_C$ Bragg reflection, measured at 20 K and a fluorescence measurement. Results collected on ID20, ESRF.

less sensitive to contributions from different domain populations in the sample. The technique of rotating the incident polarisation has previously been demonstrated to allow the determination of otherwise unresolvable mixed multipolar contributions to the scattering [52], the relative contributions of magnetic domains [95], and the determination of magnetic moment directions [96]. To perform the polarisation analysis, an azimuthal position was selected, and the polarisation of the incident light rotated through 180° from σ to π to σ, in the direction indicated in figure 2.12. To extract the polarisation information of the diffracted signal the analyser crystal was rotated through 180° around η for each value of the incident polarisation. The dependence of the intensity on the angle of the analyser crystal allowed the linear components of the familiar self normalised Stokes' parameters [42] to be extracted:

$$P_1 = \frac{(I_{\sigma'} - I_{\pi'})}{I_0}, \tag{2.2}$$

$$P_2 = \frac{(I_{+45^{\circ\prime}} - I_{-45^{\circ\prime}})}{I_0} \tag{2.3}$$

where I_0 represents the total scattered intensity. $I_{\sigma'}$ and $I_{\pi'}$ represent the intensities of the scattered σ' and π' channels while $I_{+45^{\circ\prime}}$ and $I_{-45^{\circ\prime}}$ represent the intensities of the scattered $\eta = +45^{\circ}$ and $\eta = -45^{\circ}$ intermediate channels, where η is defined as in figure 1.10. Of course $\eta = 0$ corresponds to the scattered σ' channel and $\eta = 90$ corresponds to the scattered π' channel. The Stokes' parameters are extracted by fitting the reflection intensities as a function of η to equation 2.4 [97],

$$I = \frac{I_0}{2}[1 + P_1\cos(2\eta) + P_2\sin(2\eta)]. \tag{2.4}$$

We are unable to directly measure the circularly polarised components to find P_3,

$$P_3 = \frac{(I_{\circlearrowright'} - I_{\circlearrowleft'})}{I_0}, \tag{2.5}$$

where $I_{\circlearrowright'}$ and $I_{\circlearrowleft'}$ represent the scattered intensities in the right and left circularly polarized channels, respectively. However, an upper limit for P_3 can be deduced

through subtraction as

$$P_{N-L}^2 = 1 - P_1^2 - P_2^2. \tag{2.6}$$

This thus produces a *pseudo* P_3 value, which represents all non-linearly polarised terms.

The result of the polarisation analysis in terms of P_1 is shown in figure 2.19. It is immediately obvious that the (0, 0, $\frac{9}{2}$)$_C$ and (0 0 5)$_C$ reflections have very different polarisation dependencies, and therefore completely different origins. The scattered light from the (0, 0, $\frac{9}{2}$)$_C$ reflection has been significantly rotated, while the (0 0 5)$_C$ reflection displayed the opposite dependence, *i.e.* little change from incident to scattered polarisation.

2.5 Discussion

The first and most straightforward point that must be acknowledged is that the temperature dependence of the (0, 0, $\frac{9}{2}$)$_C$ reflection appears to show a completely first-order transition, with no significant change in intensity or width up to T_{V}, at which point the signal disappears. The widths of the reflections measured in the sample with higher crystallinity are also effectively identical, and very close to that of the (0 0 4)$_C$ Bragg peak. This is in stark contrast to the results of Lorenzo *et al.* [77], where the widths of the (0, 0, $\frac{2n+1}{2}$)$_C$ type reflections were found to be almost an order of magnitude larger than the (0, 0, $2n + 1$)$_C$ type reflections, and where a correlation length of ~ 100 Å along the c-axis was reported for the former reflections. The most likely explanation is that a sample with excess oxygen was used in the former study, as this is know to cause second-order transitions in heat capacity measurements [65].

To examine the energy and polarisation dependencies the scattering from charge and non-charge ordered structures of magnetite was modelled using FDMNES. A 7 Å cluster radius was used containing 148 atoms, and the magnetic structure was neglected, as the observed signals were too intense to result from magnetic scattering. This was confirmed through initial tests, which revealed that adding the

magnetic structure did not affect the results. To obtain an accurate fit to the degree of charge segregation, a much greater number of reflections is required, such as performed by Nazarenko *et al.* [26]. Thus, in this case a simplified charge order model based on the most recent refined structure was used [72]: a Cc structure derived from the $Pmca$ structure of Wright *et al.* [71], using a charge disproportionation between the B1 and B2 sites only [72]. The charge ordered structure, in the form of the $Pmca$ structure is shown in figure 2.20. The best agreement with the experimental data was found for a disproportion of 0.2 e^-, however, due to the limited data set it is not possible to provide accurate errors.

Figure 2.21 clearly demonstrates that the main origin of the (0, 0, $2n+1$)$_C$ reflections is charge ordering. Specifically, the resonant features are entirely caused by the charge disproportionation. The simulations shown represent the E1-E1 component, and it was found that this was the only significant contribution to the scattering. The energy scans of the (0, 0, $\frac{2n+1}{2}$)$_C$ reflections were also carried out in the σ-σ' channel. However, as is now clear following the polarisation analysis shown in figure 2.19, the majority of the signal was in the scattered π' channel for σ incident light. The results of the simulations with and without charge order for the (0, 0, $\frac{9}{2}$)$_C$ reflection are shown in figure 2.22. The simulations for both the σ-σ' and σ-π' channels are shown, however, the σ-π' channel simulation has been scaled down by $\sim 99.08\%$ to correspond to the expected amount of the π' polarised light resulting from the analyser leakthrough. It is clear that in both the charge ordered and non-charge ordered cases, the σ-π' leakthrough contribution is responsible for the observed signal. This is clear in the non-charge ordered model, as there is no σ-σ' contribution, but the same appears to be true for the charge ordered model, as the feature close to 7.13 keV is not coincident with any of the features in the σ-σ' simulation. To confirm that the measured signal is in fact almost purely σ-π' leakthrough, an energy scan was performed on the second sample on the XMaS beamline, in the σ-π' channel. The energy scan, shown in figure 2.23, was repeated at a slightly offset azimuthal position, and found to be identical, demonstrating the scans to be clear of multiple scattering. The XMaS energy scan has been shifted by

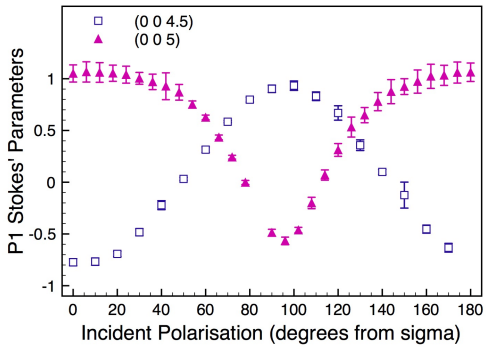

Figure 2.19: The polarisation dependence of the (0, 0, $\frac{9}{2}$)$_C$ (blue squares) (0 0 5)$_C$ (purple diamonds) reflections. Measured at 20 K with an energy of 7.120 keV. Results collected on ID20, ESRF.

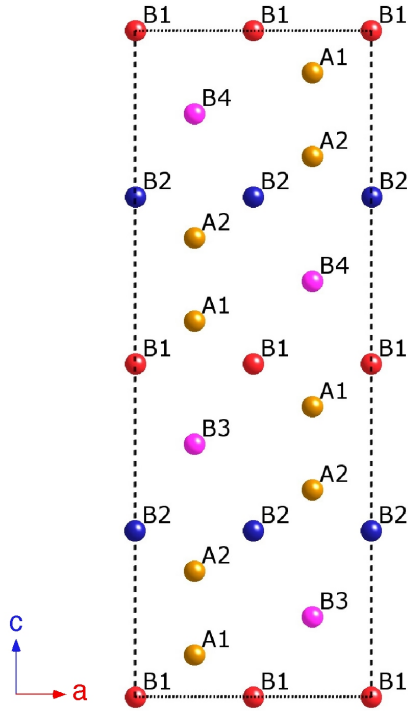

Figure 2.20: The charge ordered structure used, presented as the $Pmca$ structure as in figure 2.5. The B1 sites are $Fe^{2.4+}$, the B2 sites are $Fe^{2.6+}$, while the other sites do not make large contributions to the charge order, and have valences of $Fe^{2.5+}$ and Fe^{3+} for the B3/B4 and A sites respectively.

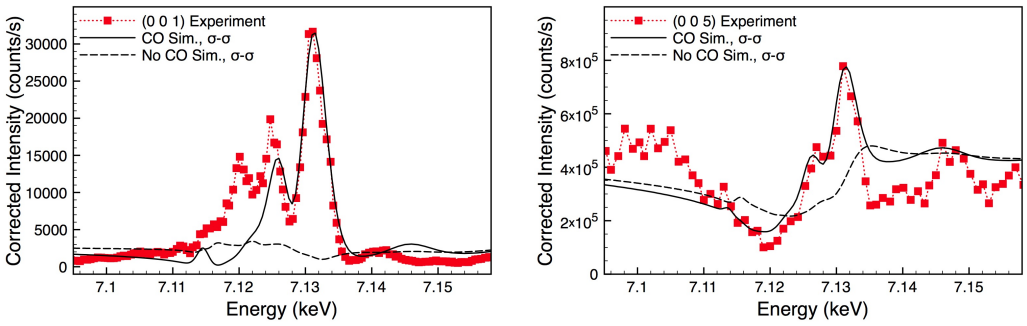

(a) (b)

Figure 2.21: The energy dependence of the (a) $(0\ 0\ 1)_C$ and (b) $(0\ 0\ 5)_C$ reflections at 20 K in the σ-σ' channel, measured at fixed wavevector. The experimental dependence has been corrected for multiple scattering and absorption effects. The solid (dashed) line represents a simulation with (without) charge order (CO). The simulation axes have been scaled to obtain the best agreement, and the corrected intensity represents an order of magnitude estimate based on figure 2.14(a). Results collected on ID20, ESRF.

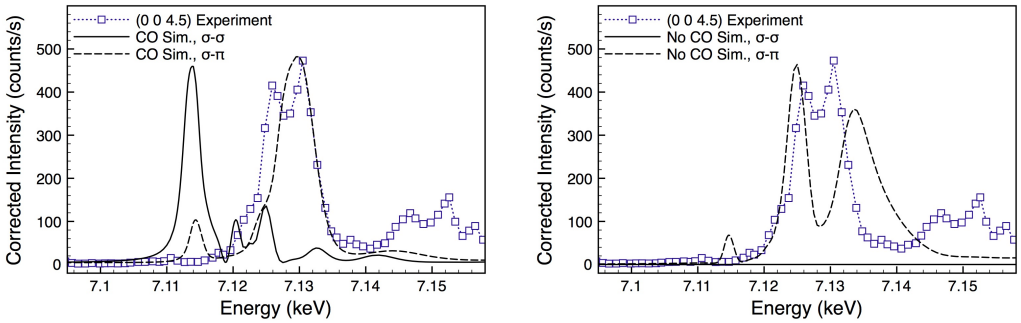

(a) (b)

Figure 2.22: The energy dependence of the $(0,\ 0,\ \frac{9}{2})_C$ reflection at 20 K in the σ-σ' channel, measured at fixed wavevector. The experimental dependence has been corrected for multiple scattering and absorption effects. The solid and dashed lines represent simulations with charge order (a) and without charge order (b). Although the dependence was measured in the σ-σ' channel, the leakthrough from the σ-π' channel was measured to be $\sim 0.92\%$, and so the σ-π' simulation is shown with an attenuation of $\sim 99.08\%$ relative to the σ-σ' simulation. The simulation axes have been re-scaled to obtain the best agreement, and the corrected intensity represents an order of magnitude estimate based on figure 2.14(a). Results collected on ID20, ESRF.

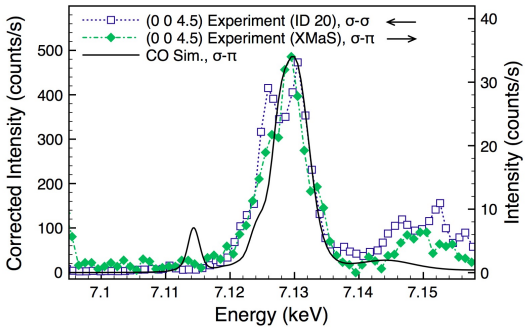

Figure 2.23: Energy scans at fixed wavevector of the $(0, 0, \frac{9}{2})_C$ reflection, measured in the σ-π' channel at XMaS (green diamonds) and the σ-σ' channel on ID20 (purple squares). The XMaS data has been shifted by 4.5 eV in order to coincide with the ID20 measurement. The simulation including charge order for the σ-π' channel is also included. Results collected on ID20 and XMaS, ESRF.

4.5 eV in order to coincide with the ID20 energy scan. However, this shift is most likely due to a difference in the energy calibration of the beamlines; it is unlikely that both the main feature and the broad high energy features would agree so well if this was not the case. We point out that the lower intensity of the σ-π' energy scan, despite measuring the σ-π' channel directly, is due to the lower intensity of the incident beam at XMaS and the lower crystallinity of the sample, which scatters over a larger range in θ. It is clear that the spectra are very similar in shape, confirming that the energy scan measured on ID20 is predominantly leakthrough from the σ-π' channel, as expected. The results of the simulations with and without charge order for the $(0, 0, \frac{1}{2})_C$ reflection are shown in figure 2.24. In this case the reflection was not later checked in the σ-π' channel on XMaS, however, given that both reflections are expected to have the same origins, it is a valid assumption that the σ-π' leakthrough is the dominant component once again.

For the $(0, 0, \frac{9}{2})_C$ reflection the charge ordered model clearly shows a much stronger agreement with experiment, while for the $(0, 0, \frac{1}{2})_C$ reflection the non-charge ordered model agrees slightly better. However, in both cases reflections are still present, both with and without charge order. It is thus clear that while the charge ordering clearly effects the shape of the spectra, it it not the origin of the reflections.

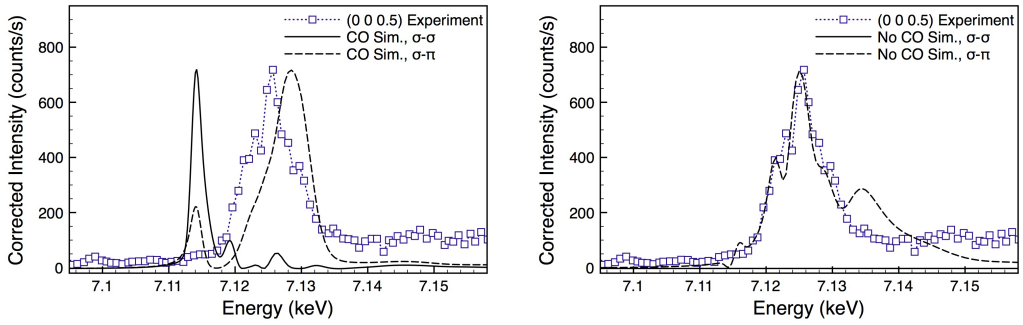

(a) (b)

Figure 2.24: The energy dependence of the (0, 0, $\frac{1}{2}$)$_C$ reflection at 20 K in the σ-σ' channel, measured at fixed wavevector. The experimental dependence has been corrected for multiple scattering and absorption effects. The solid and dashed lines represent simulations with charge order (a) and without charge order (b). Although the dependence was measured in the σ-σ' channel, the leakthrough from the σ-π' channel was measured to be $\sim 0.92\%$, and so the σ-π' simulation is shown with an attenuation of $\sim 99.08\%$ relative to the σ-σ' simulation. The simulation axes have been re-scaled to obtain the best agreement, and the corrected intensity represents an order of magnitude estimate based on figure 2.14(a). Results collected on ID20, ESRF.

As the models do not include orbital or magnetic order, it would therefore appear that the (0, 0, $\frac{2n+1}{2}$)$_C$ reflections are structural ATS (Templeton) reflections. This would explain not only the energy dependencies, but also the widths of the reflections. The widths suggest a correlation length close to that of the crystallographic order, which we expect to be equivalent for ATS reflections. The strong agreement between the charge ordered model and experiment for three of the reflections, and the fair agreement of the fourth, suggest that the system is indeed charge ordered. There is clearly not a perfect agreement between simulation and experiment, with the main reason being that the structure is not quite correct. One argument against the charge order simulations of figures 2.22(a) and 2.24(a) is that there does not appear to be any indication of the large pre-edge feature, predicted in both channels: the combined effect would be a feature that we would expect to be dominant. The results of the calculation reveal that the pre-edge features in the simulations for both (0, 0, $\frac{2n+1}{2}$)$_C$ type reflections primarily originate from the tetrahedral sites,

while the feature which is higher in energy (corresponding to the measured signal) originates almost entirely from the octahedral sites. We note here that the spectra of the (0, 0, $\frac{2n+1}{2}$)$_C$ type reflections are highly sensitive to the crystallographic structure, and so it is not particularly surprising that the simulation does not fully replicate the experimental data.

By studying the polarisation dependencies of the reflections it is possible to confirm their origins. For the (0, 0, $\frac{9}{2}$)$_C$ reflection both a simplified model and the charge ordered Cc structure, simulated using FDMNES, is shown in figure 2.25. The $Pmca$ model is highly simplified, and assumes that the scattering factors from each site are equal. This model is generated by considering the site symmetry of each iron site, and producing a scalar and a rank two tensor (for non-magnetic E1-E1 scattering) for each inequivalent site, which is invariant under its own site symmetry. This tensor is then translated between the equivalent sites by rotations and reflections, producing additional tensors, which are then summed together in a structure factor equation (as in equation 1.6). This produces the terms from equation 1.23. In the $Pmca$ structure the iron sites have three different site symmetries: m_{yz} (A1, A2, B3 and B4); $\bar{1}$ (B1); 2_y (B2). Of course for reflections of the type (0, 0, $\frac{2n+1}{2}$)$_C$ the scalar terms cancel (as the reflection is forbidden), while for the rank two tensors the B2 components cancel, but the rest have allowed contributions, producing tensors of the form

$$f^{(0,\,0,\,\frac{2n+1}{2})_C} = 0; \;\; \hat{S}_{ATS}^{(0,\,0,\,\frac{1}{2})_C} = \begin{pmatrix} 0 & 0 & 0 \\ 0 & 0 & Q_{yz} \\ 0 & Q_{yz} & 0 \end{pmatrix}. \tag{2.7}$$

For the (0, 0, $2n+1$)$_C$ reflections the resulting tensors are

$$f^{(0,\,0,\,2n+1)_C} = f^0; \;\; \hat{S}_{ATS}^{(0\;0\;1)_C} = \begin{pmatrix} Q_{xx} & 0 & 0 \\ 0 & Q_{yy} & 0 \\ 0 & 0 & Q_{zz} \end{pmatrix}, \tag{2.8}$$

with all sites having allowed contributions. An important result is that we see that

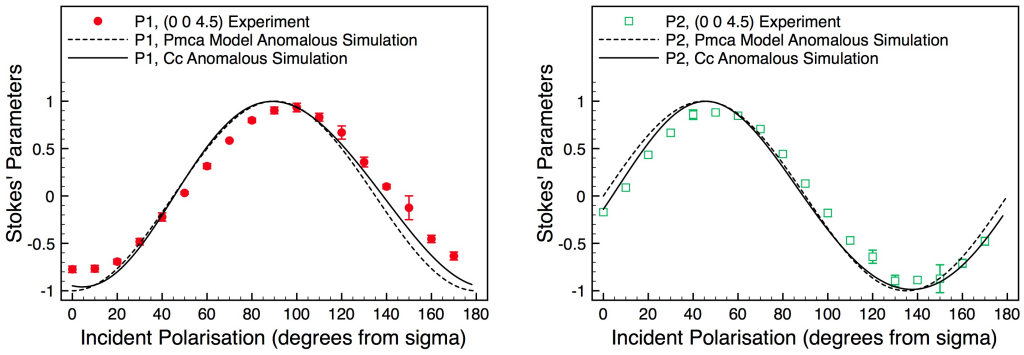

(a) (b)

Figure 2.25: The polarisation dependence of the (0, 0, $\frac{9}{2}$)$_C$ reflection at 20 K, with the energy tuned to 7.120 keV. The dashed line represents the simplified ATS scattering model in the $Pmca$ unit cell which neglects the different scattering factors between each site. The solid line represents an FDMNES simulation produced using the full Cc structure. Results collected on ID20, ESRF.

there are allowed contributions to the resonance from both scalar and tensor components for the (0, 0, $2n + 1$)$_C$ reflections.

As we see from figure 2.25, both models agree well with the experimental data. The fact that the simple $Pmca$ model agrees so well is evidence that the interpretation of the origin of the reflection as a structural ATS reflection is correct. However, it is interesting to examine the non-linear, *pseudo* P_3, component of the scattered polarisation, figure 2.26(a). A significant proportion of the scattered light has become non-linearly polarised, and although the FDMNES simulation has failed to fully predict the observed phenomena, it has replicated the general trend. This component is circularly polarised, and the associated P_3 component shown in figure 2.26(b) is significant. The measured component is too large to be from any non-linear polarisation effects at the phase plate, or from any interference from magnetic scattering at the iron K edge, where the iron atoms have magnetisation of $\approx 4.2\ \mu_{\mathrm{B}}$. Furthermore, at the extremes of the figure, the phase plate is most efficient, and operating at close to 100% conversion.

The principle behind the production of circularly polarised light is that the inequivalent iron sites possess subtly different scattering factors at the absorption

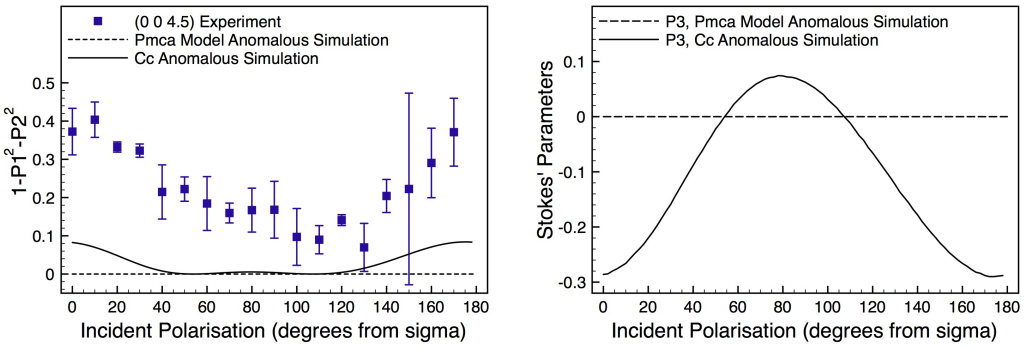

(a) (b)

Figure 2.26: (a) The square of the non-linear component of the polarisation dependence of the (0, 0, $\frac{9}{2}$)$_C$ reflection at 20 K, with the energy tuned to 7.120 keV. The dashed line represents the simplified ATS scattering model in the $Pmca$ unit cell which neglects the different scattering factors between each site. The solid line represents an FDMNES simulation produced using the full Cc structure. (b) The corresponding P_3 components from both models. Results collected on ID20, ESRF.

edge, which introduce different complex coefficients into the structure factor. This can be seen through the simplified model (dashed line) which by assuming each site has the same anisotropic scattering factor, fails to predict any non-linearly polarised component. Indeed, we have found that by taking a simple high symmetry structure, and introducing different distortions around each (previously) equivalent site, thus creating slightly different environments for each new sublattice, the effect can be replicated in FDMNES simulations for other systems.

In figure 2.27 we see that for the (0 0 5)$_C$ reflection, the dominant contribution is from isotropic charge scattering, as expected. In this case the $Pmca$ model is not explicitly shown, as the isotropic scattering models are equivalent and all terms are zero except the diagonal terms, which are equal, $Q_{xx} = Q_{yy} = Q_{zz}$. In this case the models are almost indistinguishable from each other, and agree reasonably well with experiment. However, the difference becomes clear when we again consider the non-linearly polarised components. The non-linearly polarised component shown in figure 2.28(a) is much larger this time, and again such a large non-linear polarisation can not be due to losses caused by the phase plate. Although difficult to see in figure 2.28(a), the simulation does indeed predict a definite circular

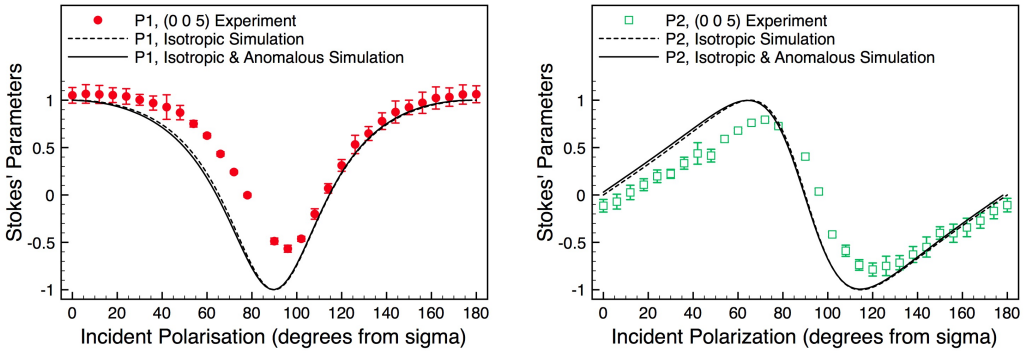

(a) (b)

Figure 2.27: The polarisation dependence of the $(0\ 0\ 5)_C$ reflection at 20 K, with the energy tuned to 7.120 keV. The dashed line represents purely isotropic scattering, while the solid line represents scattering produced using both isotropic and anomalous components. Both simulations were produced using the full Cc structure in FDMNES. Results collected on ID20, ESRF.

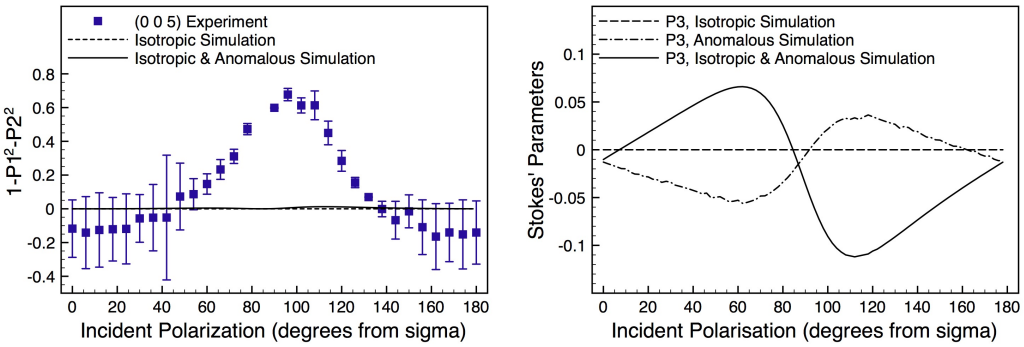

(a) (b)

Figure 2.28: (a) The square of the non-linear component of the polarisation dependence of the $(0\ 0\ 5)_C$ reflection at 20 K with the energy tuned to 7.120 keV. The dashed line represents the purely isotropic scattering, while the solid line represents scattering produced using both isotropic and anomalous components. Both simulations were produced using the full Cc structure in FDMNES. (b) The corresponding P_3 components of the isotropic and anomalous components. Results collected on ID20, ESRF.

component, as is seen in figure 2.28(b) when the P_3 component is considered explicitly. The circularly polarised components produced by the simulation are generated through the anomalous terms, as for the $(0\ 0\ \frac{9}{2})_C$ reflection. However, it is interesting to note that the addition of the Thomson isotropic terms to the simulation results in small changes to the simulation. Figure 2.29 reveals that the circular components are large, and that the right and left components are very similar, resulting in the small P_3 values in the simulation in figure 2.28(b). Again the simulations do not fully replicate the experimental observations, and this is again expected to be the consequence of the applied structure being incorrect. In this case the result is that the anomalous contribution is under estimated, and so the isotropic linearly polarised components dominate.

It is now reasonable to ask whether it is possible to progress any further without either a more accurate structure or a larger number of reflections? In this case there is still some additional information that can be gleaned by considering the $P2/c$ extension to the simplified $Pmca$ structure. When the symmetry is reduced to the $P2/c$ unit cell, additional Q_{xy} terms become allowed in equation 2.7. However, these terms are expected to be small, as they result from the small monoclinic distortion and so are effectively attenuated by a factor of $\sim |\cos(\beta)| = 0.00411$. Even so, what happens when we allow such terms to exist? When comparing to the self normalised Stokes' parameters within the $P2/c$ model, it is only the ratio of $Q_{yz} : Q_{xy}$ which is relevant. Here, we find that a ratio of $1 : 0.2i$ produces a better agreement, with any real component on the right hand side having to remain small in order to maintain the similarity to the data. We therefore conclude that the Q_{xy} components must have a large contrast between related sites on one (or more) of the iron sublattices in order to be detectable despite the large attenuating factor introduced by the structural constraints.

This is indeed what is expected in the orbital order models of Leonov *et al.*, and Jeng *et al.*, on the B1 sites. These sites have alternating d_{xz} and d_{yz} orbitals, thus producing a large contrast in the xy-plane. However, we are not directly probing the $3d$ orbitals at the iron K edge, as we excite into the $4p$ band, and we are only

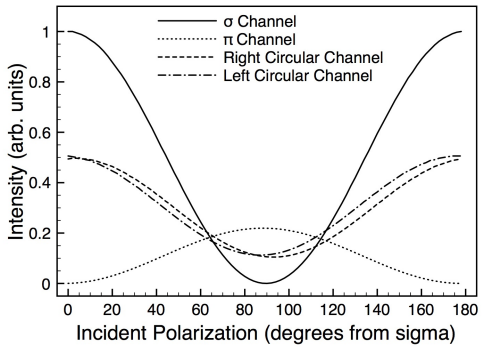

Figure 2.29: Normalised intensity showing the behaviour of each polarisation state. The simulation includes both the anomalous and isotropic components.

sensitive to the orbital occupation through the local iron environment [98]. It is known from the current structural refinements that it is the B3 and B4 octahedra which face the most distortion below T_{V}, and so it is unlikely that the B1 sites could make such a large contribution. As we have already demonstrated that the iron sublattices interfere, it is instead more likely a result of the contrast between B3 and B4 sites. In this regard an orbitally ordered model is not required to explain the observed result, as the sites are structurally and electronically inequivalent. We finally emphasise that while we are able to obtain a better agreement with the data by including the Q_{xy} terms, the vast majority of the detected signal may be explained simply by considering the Q_{yz} terms.

2.6 Conclusions

On the basis of our energy and polarisation dependencies we believe that the appearance of the (0, 0, $\frac{1}{2}$)$_C$ type reflections can be explained as a result of the structural phase transition at T_{V} with no need to invoke any charge or orbital order models. This is the same conclusion reached in the recent soft x-ray study by Wilkins *et al.* [80]; however, the soft x-ray study by Schlappa *et al.* [79] uses the appearance of the reflection as evidence for orbital ordering, which is not necessarily the case. Nevertheless, as the appearance of ATS reflections at a first-order phase transition

is a result of some local symmetry breaking, this may raise orbital degeneracy and so be linked to orbital order.

Interference between the inequivalent iron sites results in a significant contribution becoming non-linearly polarised. We would thus expect to see this effect at other reflections in alternative materials which also contain the same elements in different (crystallographic and electronic) environments. To the best of the author's knowledge, this is the first report of such a mechanism producing this phenomenon.

By applying a simplified model we have demonstrated that there is a large quadrupolar moment in the xy-plane. However, again this is not an indication of orbital order, but a demonstration of the contrast between distortions on different sites within the plane. The (0, 0, $2n + 1$)$_C$ type resonant reflections are due to charge order (in agreement with hard [77] and soft [79] x-ray studies), and contain significant components from the isotropic and anomalous terms. The appearance of a large non-linearly polarised component is in part due to the interference of the anomalous terms from inequivalent iron sites, however, the interference of the isotropic component *with* this is also important.

Finally we note that while our simulations do not fully replicate the experimental data in every aspect, they provide an acceptable approximation and indicate the physical processes involved in producing the experimental result. In this case it is an incomplete knowledge of the structure of magnetite that leads to the disagreements between the experimental and simulated data. Magnetite is a ferociously complex material, and here we have shown that simply by applying the previously reported electronic structure, reality can be approximated to a high degree. This demonstrates the difficulty in understanding the low temperature electronic structure of magnetite, even by using the most discriminating techniques.

Chapter 3

Iron Oxyborate, Fe_2OBO_3

3.1 Background

The question of whether the phenomenon of charge ordering in materials is driven through electrostatic repulsion (Wigner crystallisation [19]) or through electron-lattice coupling (principally, cooperative Jahn-Teller distortions [99, 100]) has been the subject of considerable interest in recent years. This is particularly true for the case of perovskite manganites, where a competition between the two phenomena apparently helps determine the charge configuration [11, 12, 21]. Iron oxyborate is a fascinating material when addressed in this context, as it appears to show characteristics of a model Wigner system [101, 102]. Due to the presence of boron, iron oxyborate possesses a different structure to magnetite, despite the similarities of their chemical formulae; namely Fe_2OBO_3 and Fe_3O_4. Fe_2OBO_3 instead possesses a warwickite structure, figure 3.1. The formula for such materials may instead be written $MM'OBO_3$ [103], where M and M' occupy crystallographically different sites, and are expected to be occupied by ions with different valencies. In the case of Mn_2OBO_3 this is true, and the charge ordering is apparently driven by the large Jahn-Teller distortions present [101, 103, 104]. Fe_2OBO_3 on the other hand, appears to show a more complex charge ordered structure.

Above 317 K Fe_2OBO_3 is orthorhombic, with $Pmcn$ (No. 62) structure [101] and lattice parameters $a = 3.1779$ Å, $b = 9.3945$ Å, $c = 9.2495$ Å at 337 K. The

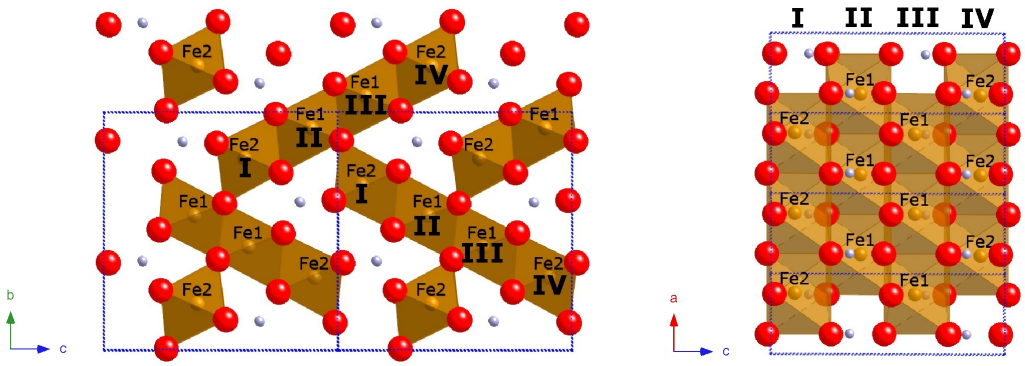

(a) (b)

Figure 3.1: Crystal structure of Fe_2OBO_3 in the high temperature orthorhombic phase. The iron, oxygen and boron atoms are shown as orange, red and grey spheres respectively. The blue dashed lines represent the high temperature unit cell. (a) Chains of four octahedra are linked in an edge sharing network, containing two crystallographically distinct sites. (b) Each chain continues infinitely along the a-axis.

structure consists of chains of four octahedra, which are linked indefinitely along the a-axis, and where at high temperature chains I & IV and II & III are crystallographically equivalent. At around 317 K the system experiences a first-order phase transition [105], and the resistivity increases by a factor of $\sim$3, figure 3.2. The transition is hysteretic, with a loop in resistivity extending over 55 K. Unlike Fe_3O_4, this transition is a semiconductor to semiconductor transition, and the conductivity remains proportional to e^{-E_a/k_BT} on both sides of the transition [101]. Mössbauer spectra [101, 105] have indicated that between 270 K and 400 K there exists a mix of static and delocalised sites, as Fe^{2+}, Fe^{3+} and $Fe^{2.5+}$ states are all observed. However, below 270 K the fluctuations cease, and the spectra suggest that the divalent and trivalent ions are equally distributed over the two crystallographically different sites. The distribution of the different valences over different sites appears to result in the slight ferrimagnetic character of the system [102, 105]. The magnetic ordering takes place at $\sim$155 K, and is clearly visible in magnetic susceptibility and specific heat measurements, figure 3.3 [106]. The system is an L-type ferrimagnet, with ferromagnetic Fe1 and Fe2 chains antiferromagnetically aligned

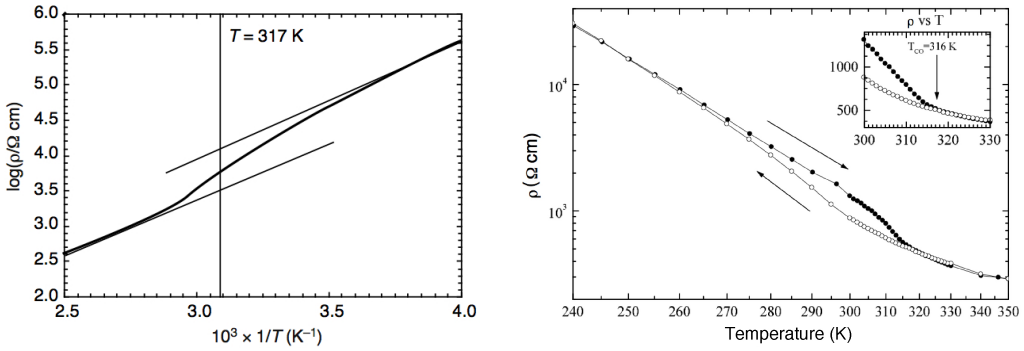

(a) (b)

Figure 3.2: (a) Inverse temperature versus log of the resistivity, showing a transition around 317 K, by Attfield *et al.* Reprinted by permission from Macmillan Publishers Ltd: Nature, reference 101, copyright 1998. (b) Inverse temperature (plotted as temperature) versus log of the resistivity, showing the transition at ∼316 K and the hysteresis indicating a first-order phase transition, by Douvalis *et al.* Reprinted with permission from IOP Publishing: J. Phys.: Condens. Matter, reference 105, copyright 2000.

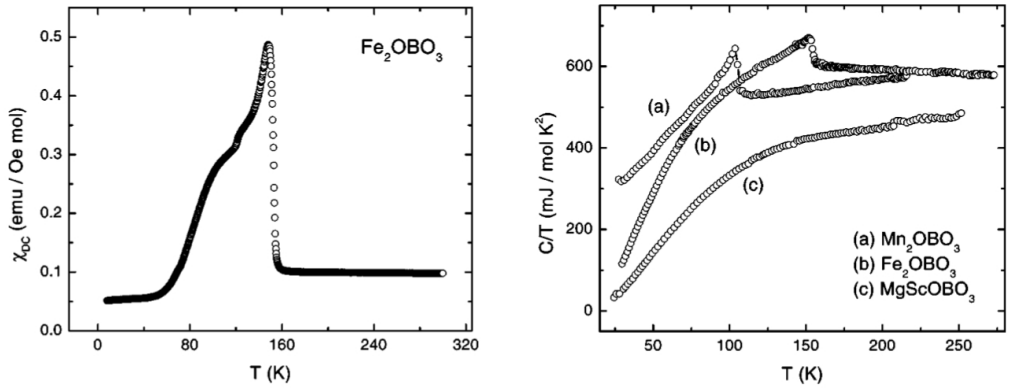

(a) (b)

Figure 3.3: (a) Zero field cooled magnetic susceptibility (DC), measured in a field of 500 Oe by Continentino *et al.* (b) Specific heat (given as C/T) against temperature for several oxyborates, measured by Continentino *et al.* Reprinted figures with permission from reference 106. Copyright 2001 by the American Physical Society.

predominantly along the a-axis [107], figure 3.4. There is a small net magnetic moment of 0.03 μ_{B} per iron atom, whereas manganese oxyborate is antiferromagnetic at low temperatures [103].

In the charge ordered phase the structure becomes monoclinic with a maximum monoclinic angle of $\sim$90.2° at $\sim$190 K, and a doubled a-axis supercell, as predicted by Attfield *et al.* [101, 102]. The original proposed charge ordered structure is shown in figure 3.5. It was speculated that the breaking of the mirror symmetry in this charge ordered structure, which requires tilting of the octahedra, results in *nanocrystal* domains. Confirmation of this charge ordered structure through powder diffraction was found to be unfeasible, and the average structure over high temperature equivalent sites was instead obtained. The problem was suggested to be that because the charge ordered domains were on the nanometer scale, they were too poorly correlated to detect.

LSDA+U calculations have predicted the same charge ordered structure as the Attfield *et al.* configuration, as well as correctly predicting the size of the ferrimagnetic moment and the size of the band gap [108]. As the Fe ions sit in the centre of octahedra, their orbitals are split into the e_g and t_{2g} band, meaning the Fe^{2+} ions have an orbital degree of freedom, which the LDA+U calculations by Leonov *et al.* predict are predominantly of d_{xy} type in the local cubic frame [108], figure 3.6. Leonov *et al.* [108, 109] predict a total segregation of $\sim$0.8 e^- between conventionally 2+ and 3+ sites. However, as for magnetite, they predict that screening results in a total $3d$ band difference of 0.34 e^-. Leonov *et al.* go on to suggest that contrary to the supposition of Attfield *et al.*, Fe_2OBO_3 can not be regarded as the ideal example of charge order driven by electrostatic repulsion, as in their calculations it appears that the electron-lattice mechanism is the driving force. However, it is clear that the Jahn-Teller distortions apparent in Mn_2OBO_3 are significantly (if not entirely) reduced in Fe_2OBO_3 . We note here, that although this theoretical analysis has faced debate [110], the study appears to be rigourous, and agrees with the experimental results in all key points.

Recently the growth of single crystals of Fe_2OBO_3 has become possible, open-

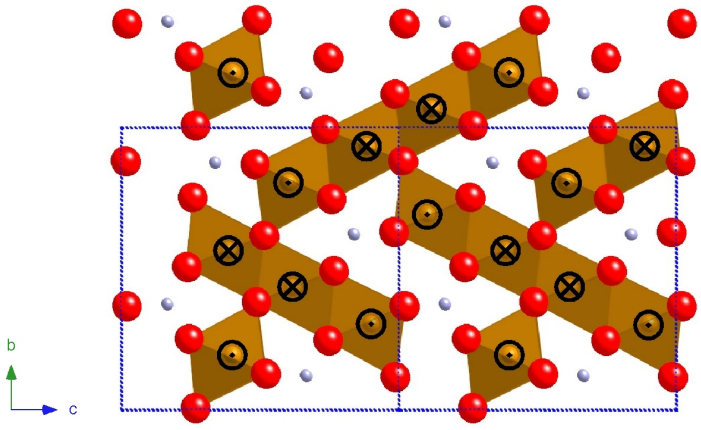

Figure 3.4: The magnetic structure, of Fe_2OBO_3 . The spins are predominantly into and out of the page, although there is $\approx 5^\circ$ canting along the c-axis.

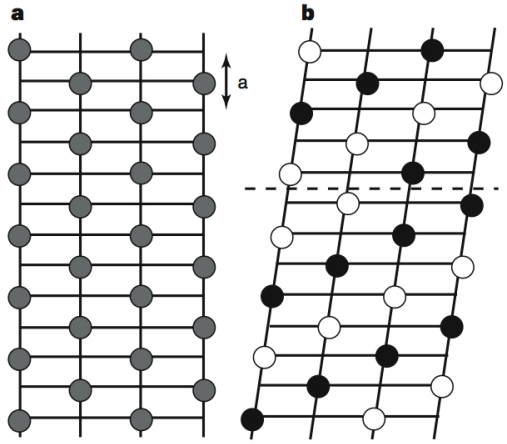

Figure 3.5: (a) The high temperature structure of Fe_2OBO_3 , where the grey spheres show Fe ions with an average $2.5+$ valence. (b) The original proposed charge ordered structure, where the white and black spheres represent Fe^{2+} and Fe^{3+} . The dashed line shows an antiphase boundary, which preserves the direction of the monoclinic distortion. Figures by Attfield *et al.* Reprinted by permission from Macmillan Publishers Ltd: Nature, reference 101, copyright 1998.

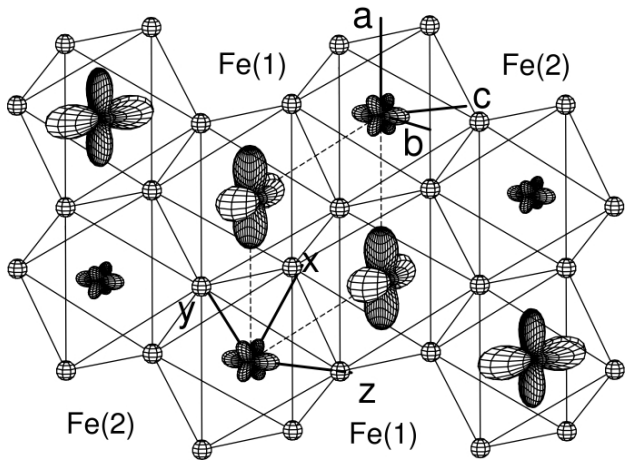

Figure 3.6: Arrangement and occupancy of the $3d$ iron orbitals, as predicted by LSDA+U calculations by Leonov *et al.* Reprinted figure with permission from reference 108. Copyright 2005 by the American Physical Society.

ing up the possibility for new diffraction studies. Recent experiments have identified charge order reflections at low temperatures, at a wavevector of ($h + \frac{1}{2}$, k, l), confirming the doubled a-axis of the supercell [111]. Further experiments have identified that the commensurate charge order only persists to 280 K, at which point the charge order reflections are visible at ($h + \frac{1}{2}$, k, $l \pm \tau$) positions, figure 3.7. Here, τ is temperature dependent, and is reported to vary between $0.25 < \tau < 0.4$ with increasing temperature, until 340 K where the reflections become significantly broader and only short range correlation exists [112].

Despite now being able to observe the charge order reflections, confirming the charge configuration in the commensurate phase has still proven difficult. The problem arises due to the twinning of the charge domains within the crystal, resulting in a charge domain average structure being observed [111], figure 3.8. The average structure obtained through diffraction does include some fascinating results however, as the bond valence sum values appear to indicate that the system is close to true Fe^{2+}/Fe^{3+} valence. This average structure is expected to be the result of equal *up* and *down* diagonal stripes, figure 3.9(a) and (b). The application of further GGA+U studies to this problem has confirmed that the *up-down* diagonal charge

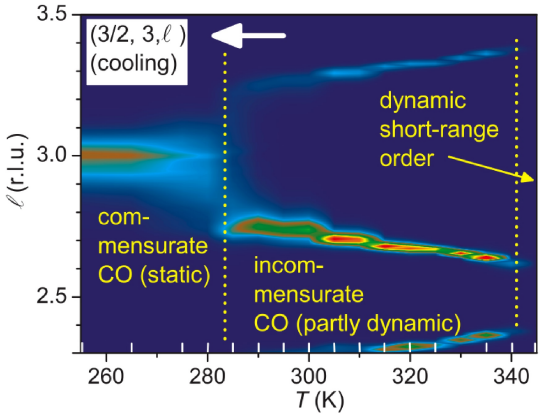

Figure 3.7: A temperature map by Angst *et al.* of the $(\frac{3}{2}, 3, l)$ reflection, showing the commensurate and incommensurate reflections. Reprinted figure with permission from reference 112. Copyright 2007 by the American Physical Society.

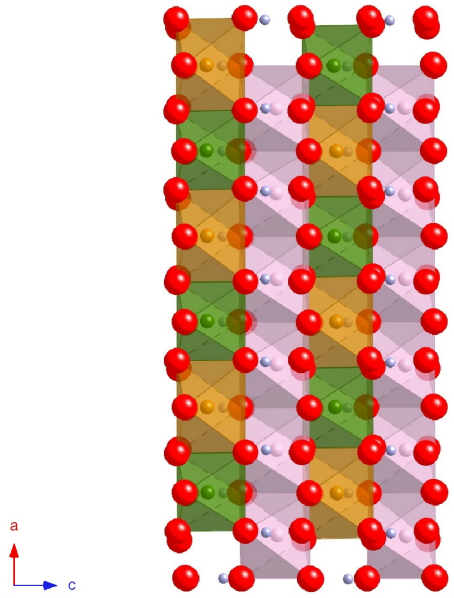

Figure 3.8: The charge domain averaged low temperature structure of Fe_2OBO_3. The orange sites are Fe^{2+}, the green sites are Fe^{3+}, and the pink sites are $Fe^{2.5+}$.

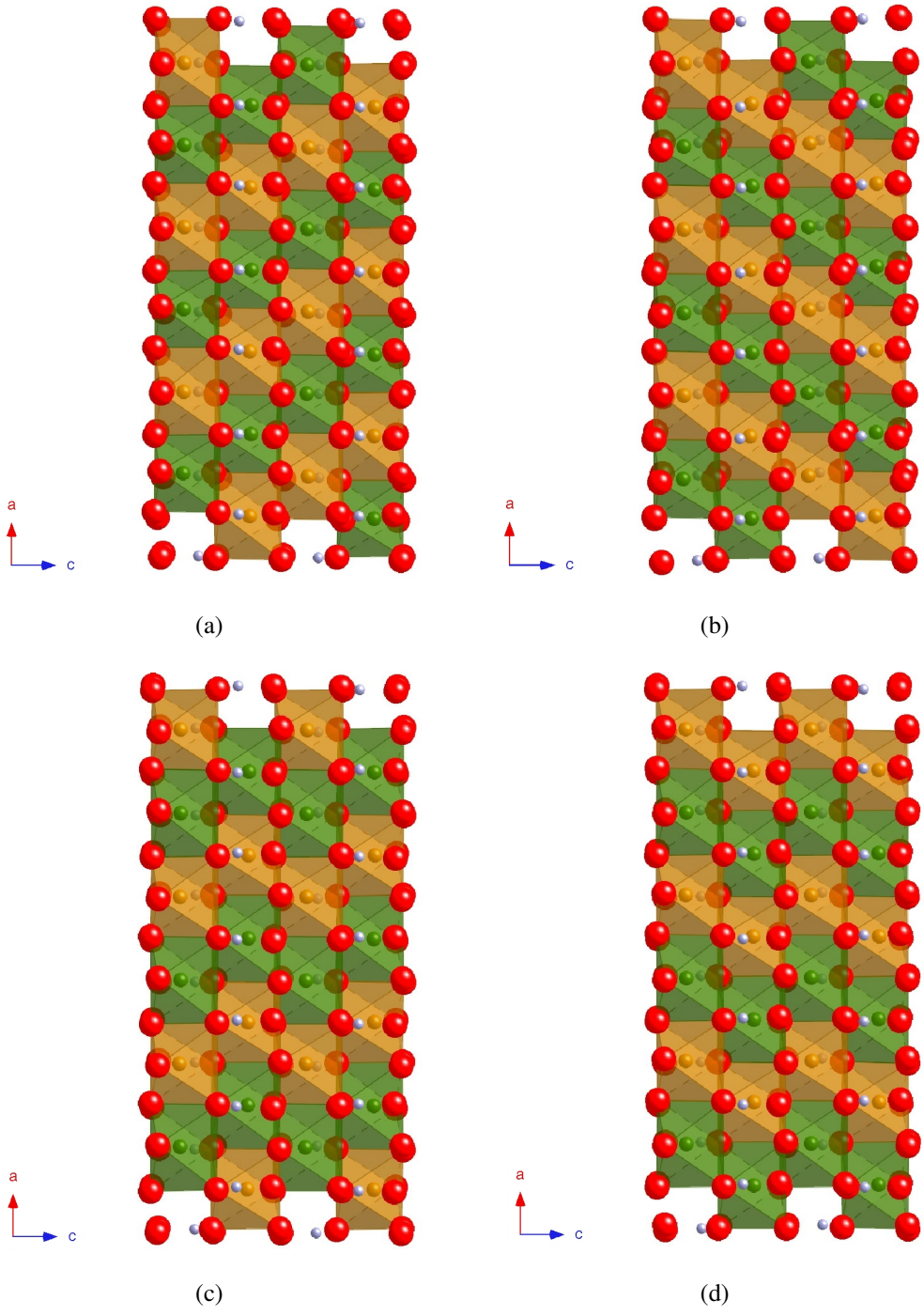

Figure 3.9: A single iron chain, with the (a) *up* & (b) *down* and (c) *zig* & (d) *zag* charge ordered structures. The orange sites are Fe^{2+}, while the green sites are Fe^{3+}.

configuration predicted previously is the favourable solution. However, an alternative *zig-zag* domain structure, which can also possess two symmetrically opposite domains, is only slightly less energetically favourable, figures 3.9(c) and (d). It is this small separation in the energy of generating the different charge order states that has been proposed to produce the incommensurate modulations at high temperature, as the geometrical frustration of the situation causes antiphase domain boundaries to form, which contain fluctuating electron states [112]. Alternatively, the formation of antiphase stripes along the c-axis has also been proposed as a mechanism for the incommensurability, as these antiphase domains are periodically arranged, producing some additional superstructural order [113]. The widths of the reflections are narrow along the H direction compared to the L direction [112]. This is the result of the small size of the different domains along the c-axis, which extend much further along the a-axis [114].

The motivation behind our study was two-fold. Firstly, we wished to combine RXD and simulations in order to obtain an estimate of the size of charge disproportionation without using empirical methods, such as BVS calculations. Such a study is vital, if iron oxyborate is to be considered a model Wigner crystal. Secondly, we wished to test whether it was possible to witness the phenomenon of linearly to non-linearly polarised light, as reported in the previous chapter.

3.2 Sample Preparation and Experimental Technique

The crystal was produced using the flux growth technique, based on the successful approach of Balaev *et al.* [115] in producing $Fe_{1.91}V_{0.09}BO_4$. Fe_2O_3 and B_2O_3 were used as the starting ingredients which were added to the flux, and upon cooling crystals of Fe_2OBO_3 precipitated in the form of long needles, approximately 0.2 mm wide and 0.1 mm thick. The needles were extended along the a-axis, and different samples displayed different facets as their wide surface, with [0 1 1] and [0 0 1] orientations being present. The chosen sample was reduced in length by breaking, in an attempt to produce a sample which was close to being square. The

resulting sample measured approximately 0.1 mm $\times$ 0.2 mm $\times$ 0.7 mm. The sample was then attached to a copper puck using silver paint, with the natural facet being surface normal. In this case the sample did not require any further preparation in the form of polishing, as a natural facet is smoother than could be achieved using mechanical methods. An attempt was made to align the sample using a backscattering Laue camera, however, due to the small size of the crystal and the large size of the incident x-ray beam, no signal was observable above background. Instead the sample was aligned on the beamline, revealing the [0 0 1] direction to be surface normal. Throughout the experiment, the sample was orientated such that the [1 0 0] direction was in the scattering plane.

The x-ray measurements were again collected on ID20, using the vertical scattering diffractometer, with additional measurements being carried out on XMaS. In both cases a Displex cryostat was used without a radiation shield, allowing temperatures in the range ≈ 20 K to 350 K to be reached. Two experiments were performed on ID20. In the first experiment the machine was operated in *16 bunch* mode and in the latter *7/8 + 1* mode, giving ring currents of 90 and 200 mA respectively. In 7/8 + 1 mode, $\frac{7}{8}$ of the ring are filled with 868 bunches, with the final $\frac{1}{8}$ filled with a single bunch [88]. The measurements on XMaS were performed with the machine in *hybrid* mode with a ring current of 200 mA.

An MgO (2 2 2) analyser was again used for post-scatter polarisation analysis, and was found to operate with a maximum channel leakthrough of approximately 0.6%. The diamond phase plate stage was used inside a separate vessel, allowing the phase plate to be operated under vacuum, in order to reduce absorption and hence improve intensities. In this case the phase plate rotated in the opposite sense to the Fe_3O_4 experiment; however, when presented in the next section, the sense of rotation has been changed such that figure 2.12 remains correct. In the first experiment the 720 μm phase plate was used, and calibrated to operate with a minimum polarisation conversion (neglecting absorption losses) of 91% in half-wave plate mode. As the intensities were reasonably large, even while using the phase plate, a thicker 1200 μm phase plate was used for the second experiment. In this case the phase

plate was calibrated to operate with a minimum polarisation conversion (neglecting absorption losses) of 99% in half-wave plate mode. The full polarisation analysis of the main beam in both cases is shown in figure 3.10. During the second experiment, the 1200 μm phase plate was also operated in quarter-wave plate mode, to produce right handed circularly polarised light. After careful alignment of the phase plate for circular polarisation, the resultant beam was found to be $\approx 95\%$ circularly polarised. The linear polarisation dependence of the main beam is shown in figure 3.11.

3.3 Results

After mounting and aligning the sample, the polarisation analyser was installed and the commensurate $(-\frac{1}{2}, 0, 6)$ reflection identified. This index refers to the high temperature structure, and this notation is used throughout. The sample was then warmed to 320 K, the top of the hysteretic region, and the incommensurate $(-\frac{1}{2}, 0, 6 \pm \tau)$ reflections were observed. The sample was then cooled to base temperature over approximately two hours, before warming to 220 K, above the magnetic transition. However, it quickly became apparent that the sample had been cooled too rapidly, freezing in incommensurate components and resulting in very broad commensurate reflections. This was not entirely unexpected however, as similar results have previously been observed in prior studies [114]. The sample was then re-warmed to 320 K, and cooled to 220 K at a rate of 0.4 K/minute. This slow cooling resulted in a significantly better result, with much sharper commensurate features, and none of the $\pm \tau$-reflections being visible at 220 K. As can be seen in figure 3.12, when the commensurate charge order initially forms it is poorly correlated along the L-axis, with well correlated regions condensing out upon further cooling. However, as the structural dynamics are greatly reduced at low temperatures, the development of large correlated regions takes some time. This is demonstrated in figure 3.12, as it is clear that after several days of being cold, the diffuse background has disappeared, and the reflection has become truly commensurate.

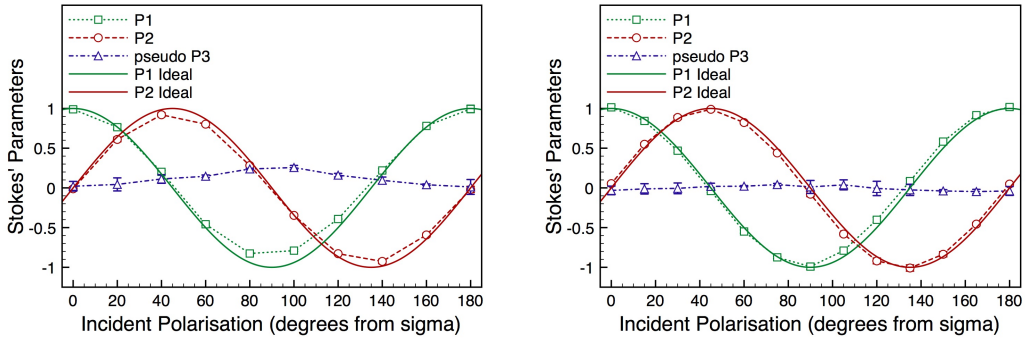

Figure 3.10: Linear polarisation analysis of the main beam, using the (a) 720 μm and (b) 1200 μm thick phase plates, in half-wave plate mode. The lines represent the ideal case for complete conversion. Results collected on ID20, ESRF.

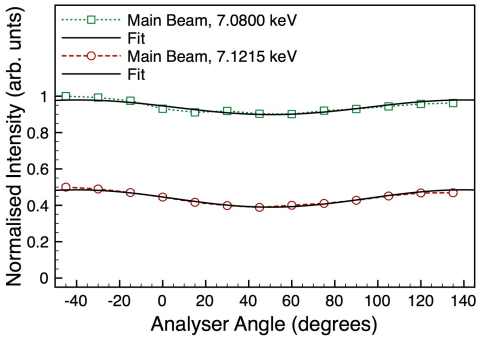

Figure 3.11: Stokes' curve (equation 2.4) fit of the main beam for incident circular polarisation. The two energies are offset for comparison. Results collected on ID20, ESRF.

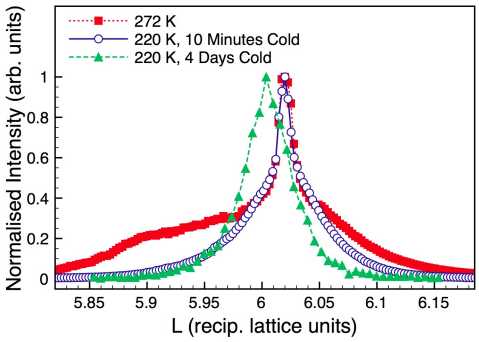

Figure 3.12: Scans along the L direction for the ($\frac{1}{2}$, 0, 6) reflection in the σ-σ' channel using an energy of 7.123 keV. The scan at 272 K was measured on cooling from the high temperature phase, after cooling at a rate of 0.4 K/minute. The scan at 220 K was measured after further cooling at the same rate. The final scan was measured after holding the sample at 220 K for four days. Results collected on ID20, ESRF.

Several other reflections were also measured after being held at 220 K for several days, and scans along the L and H directions are shown in figures 3.13 and 3.14 respectively. In the case of figure 3.14, several crystallites were observed (as seen by the split reflections), and so only the dominant contribution was fitted. The corresponding widths and correlation lengths along the L and H directions are shown in tables 3.1 and 3.2 respectively. It important to point out that the values reported in these tables represent minimum correlation lengths; hence the difference in the lengths derived from the ($-\frac{3}{2}$, 2, 6) and ($\frac{1}{2}$, 0, 6) reflections. These results indicate that all reflections are approximately equally well correlated along the a-axis,

Table 3.1: Widths and correlation lengths for reflections along the c-axis. Measured at 7.123 keV at 220 K.

Reflection	FWHM (r. l. u.)	Inv. Corr. Len. (Å^{-1})	Corr. Len. (Å)
(0 0 6)	0.00120 ± 0.00001	0.0004078 ± 0.0000330	3387 ± 28
($\frac{1}{2}$, 0, 6)	0.00515 ± 0.00085	0.00180 ± 0.00029	79 ± 2
($-\frac{3}{2}$, 2, 6)	0.08525 ± 0.00365	0.02900 ± 0.00120	48 ± 2
(0 0 7)	0.00257 ± 0.00009	0.0008734 ± 0.0000306	1582 ± 55

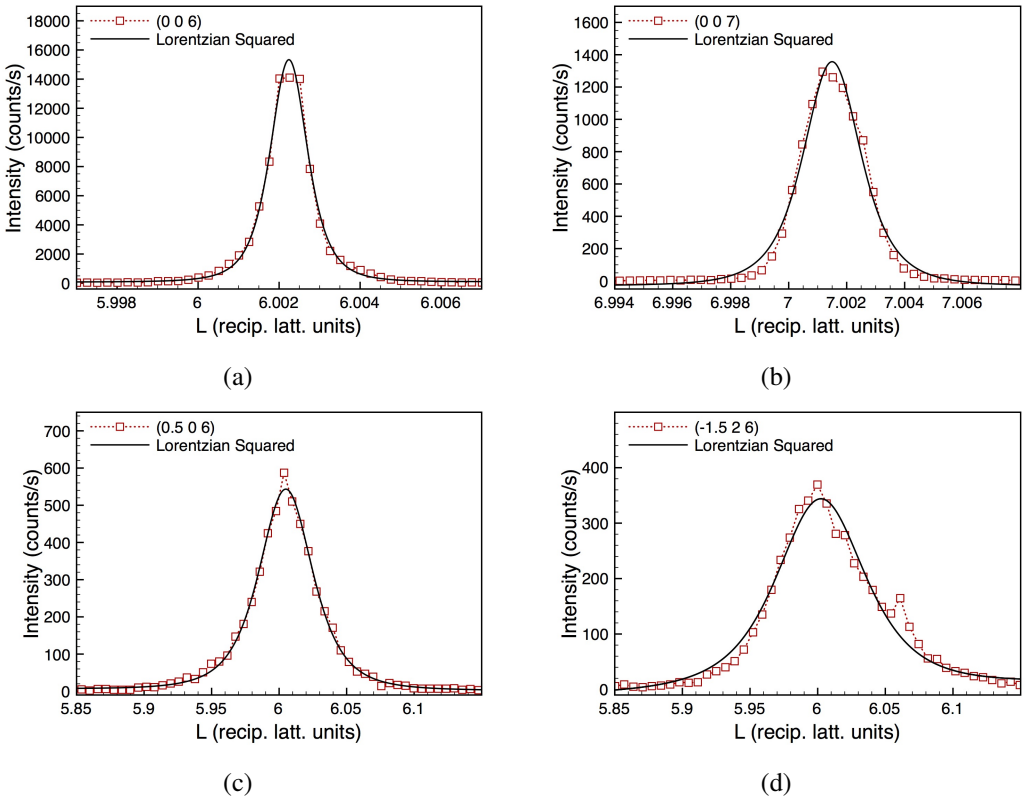

Figure 3.13: Scans along the L direction for several reflections, measured at 220 K, at 7.123 keV. Reflections (a), (c) and (d) were measured in the σ-σ' channel while (b) was measured in the σ-π' channel. The measurements were taken after the sample had been held at 220 K for four days. Results collected on ID20, ESRF.

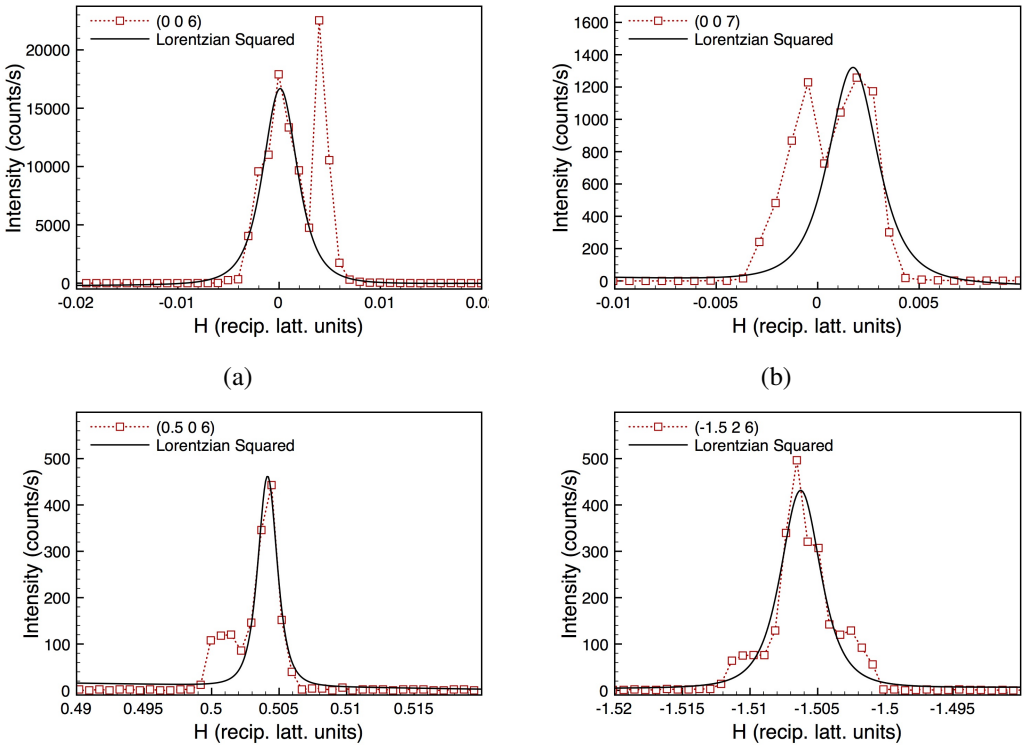

Figure 3.14: Scans along the H direction for several reflections, measured at 220 K, at 7.123 keV. Reflections (a), (c) and (d) were measured in the σ-σ' channel while (b) was measured in the σ-π' channel. The measurements were taken after the sample had been held at 220 K for four days. Results collected on ID20, ESRF.

but with the (0 0 6) and (0 0 7) reflections more correlated along the c-axis. This is not surprising as the (0 0 7) is expected to be an ATS (Templeton) reflection which is also allowed in the high temperature phase. Scans along the K direction for the (0 0 6) and (0 0 7) reflection revealed the sample to have rather poor crystallinity along the b direction, as the reflections consisted of many sharp features. Scans of the half-integer reflections were fruitful however, as the correlation length of these reflections was smaller than the individual crystallites. The resulting scans are shown in figure 3.15, with the correlation lengths given in table 3.3. There is some disagreement between the widths of the reflections measured on ID20 and XMaS, however, in all cases an accurate order of magnitude estimate is obtained.

Numerous ($\frac{2n+1}{2},\ k,\ l$) reflections were surveyed, with several displayed in figure 3.16. All scans were repeated at an offset azimuthal position in order to confirm that none of the features at the absorption edge were from multiple scattering. However, the low energy features in figures 3.16 (a) and (c) were confirmed to be multiple scattering. In addition the ($\frac{1}{2}$, -1, 7), ($-\frac{1}{2}$, 2, 7), ($-\frac{1}{2}$, 3, 6), ($-\frac{1}{2}$, 3, 7), ($-\frac{3}{2}$, 1, 6) and ($-\frac{3}{2}$, 2, 6) reflections were collected, which again did not show any multiple scattering contributions close to the absorption edge. For comparison the (0 0 4) Bragg reflection is shown in figure 3.17, as measured on the XMaS beamline. By consideration of the Bragg reflection it is possible to see that even the small feature present in the energy scan shown in figure 3.16(b) is a real resonant enhancement.

To examine the temperature dependence of the charge order reflections, the sam-

Table 3.2: Widths and correlation lengths for reflections along the a-axis. Measured at 7.123 keV at 220 K.

Reflection	FWHM (r. l. u.)	Inv. Corr. Len. (Å^{-1})	Corr. Len. (Å)
(0 0 6)	0.00438 $\pm$ 0.00021	0.00430 $\pm$ 0.00021	320 $\pm$ 16
($\frac{1}{2}$, 0, 6)	0.00183 $\pm$ 0.00019	0.00180 $\pm$ 0.00019	763 $\pm$ 83
($-\frac{3}{2}$, 2, 6)	0.00381 $\pm$ 0.00030	0.00380 $\pm$ 0.00029	368 $\pm$ 29
(0 0 7)	0.00313 $\pm$ 0.00043	0.00310 $\pm$ 0.00042	448$\pm$ 61

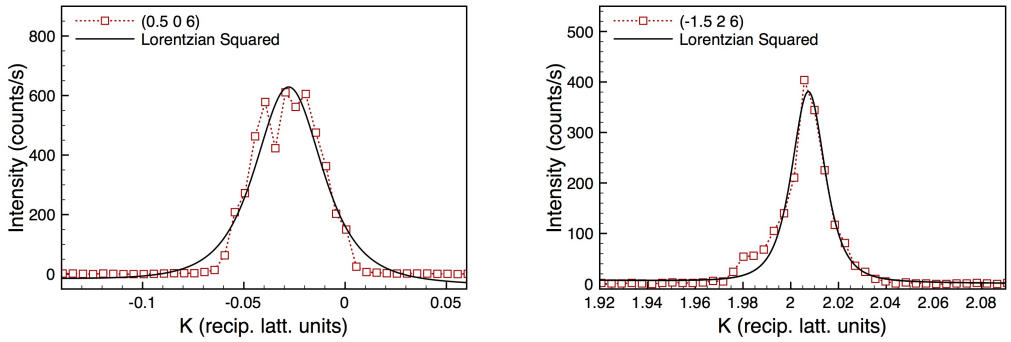

(a) (b)

Figure 3.15: Scans along the K direction for several reflections, measured at 220 K, at 7.123 keV in the σ-σ' channel. The measurements were taken after the sample had been held at 220 K for four days. Results collected on ID20, ESRF.

ple was studied on the XMaS beamline. Due to the reduced θ range available, it was not possible to reach as many reflections as on ID20 without changing the sample geometry, although several were within range. After aligning the sample, it was rapidly warmed to 350 K and then cooled to 220 K at a rate of 0.2 K/minute. The sample was then re-aligned and the MgO (2 2 2) polarisation analyser installed. Unfortunately, perhaps due to the much larger incident beam size on the small sample on XMaS, we suffered from a great deal of contamination from powder reflections; presumably originating from the copper puck or the silver paint. However, we were able to study the $(-\frac{1}{2}, 3, 7)$ reflection with minimal problems. The reflection was then repeatedly aligned and measured, as the sample was warmed in stages at a rate of 0.2 K/minute. The result of this temperature dependence can be seen in figure 3.18, where we see a large difference between the resonant and non-resonant components of the signal. This is made apparent in figure 3.19(a), where the sharp

Table 3.3: Widths and correlation lengths for reflections along the b-axis. Measured at 7.123 keV at 220 K.

Reflection	FWHM (r. l. u.)	Inv. Corr. Len. (Å^{-1})	Corr. Len. (Å)
$(\frac{1}{2}, 0, 6)$	0.04270 ± 0.00295	0.01440 ± 0.00099	96 ± 7
$(-\frac{3}{2}, 2, 6)$	0.01798 ± 0.00083	0.00610 ± 0.00028	228 ± 11

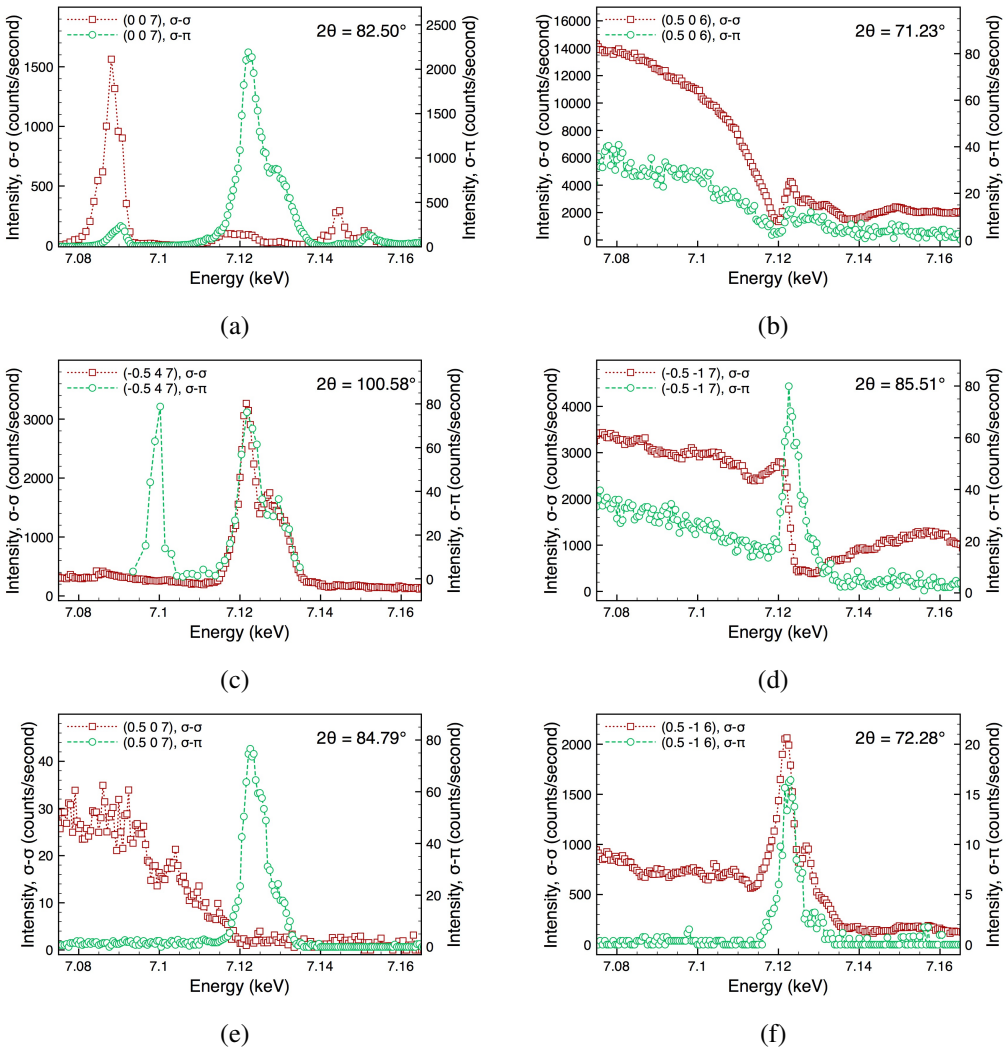

Figure 3.16: A selection of the energy scans measured in Fe_2OBO_3 at 220 K at fixed wavevector. The low energy features in (a) and (c) were confirmed to be multiple scattering. The 2θ values shown are for an energy of 7.12 keV. Results collected on ID20, ESRF.

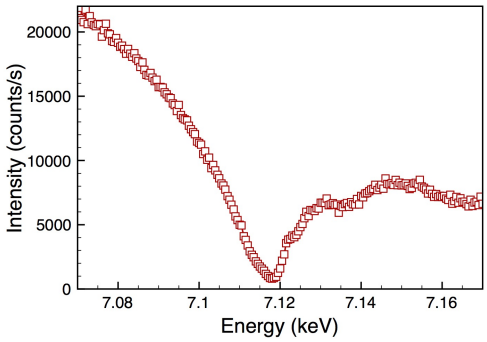

Figure 3.17: Energy scan of the (0 0 4) Bragg reflection, measured at 220 K at fixed wavevector. Results collected on XMaS, ESRF.

spike on top of the broad background is seen off-resonance, while on-resonance only the broad background is clear. The widths associated with the curves fitted to figure 3.19 are given in table 3.4. The slightly incommensurate nature of the reflections is again apparent, and by comparing to figure 3.19(b), it is clear that this is not just the result of a poor alignment matrix. Energy scans of the reflection were collected during the warming, and show a gradual reduction in the resonant/non-resonant ratio, figure 3.20(a). This trend continued into the incommensurate phase, with a greatly diminished resonant feature, as seen in figure 3.20(b). To study the hysteretic effects and the incommensurate region, the sample was again warmed to 350 K, before cooling at a continuous rate of 0.2 K/minute while constantly performing scans along the L direction, figure 3.21. The sample was then immediately warmed at the same rate, while performing the same scans, figure 3.22. Figure 3.21 is in good agreement with the temperature dependence measured by Angst *et*

Table 3.4: Widths for $(-\frac{1}{2}, 3, 7)$ and (0 0 6) measured on- and off-resonance at XMaS, at 220 K along the c-axis.

Reflection	FWHM	Inv. Corr. Len. (Å^{-1})	Corr. Len. (Å)
(0 0 6)	0.00412 ± 0.00009	0.001400 ± 0.000031	987 ± 22
$(-\frac{1}{2}, 3, 7)_{\text{off res.}}$	0.01887 ± 0.00161	0.006400 ± 0.000547	215 ± 18
$(-\frac{1}{2}, 3, 7)_{\text{on res.}}$	0.07960 ± 0.00528	0.02710 ± 0.00180	51 ± 3

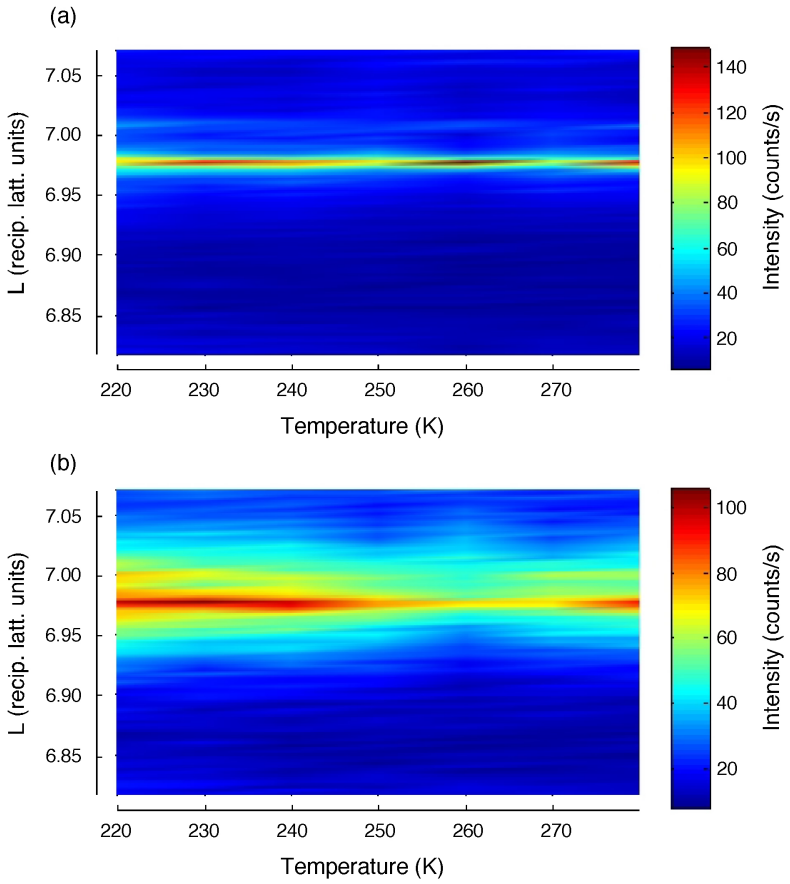

Figure 3.18: Temperature dependence on warming of the $(-\frac{1}{2}, 3, 7)$ reflection in the σ-σ' channel, measured (a) off-resonance and (b) on-resonance at 7.070 keV and 7.123 keV respectively. The sample was warmed at a rate of 0.2 K/minute. Results collected on XMaS, ESRF.

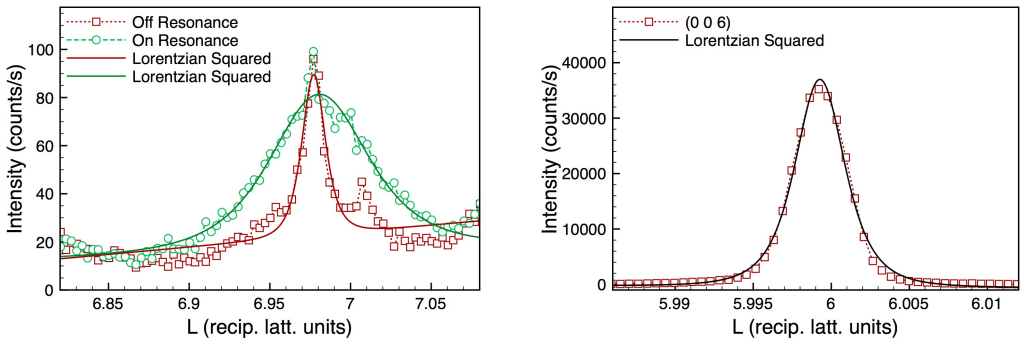

(a) (b)

Figure 3.19: Scans along the L direction for (a) the $(-\frac{1}{2}, 3, 7)$ reflection and (b) the (0 0 6) Bragg reflection, measured in the σ-σ' channel at 220 K. The former reflection was measured at 7.070 keV (off-resonance) and 7.123 keV (on-resonance). Results collected on XMaS, ESRF.

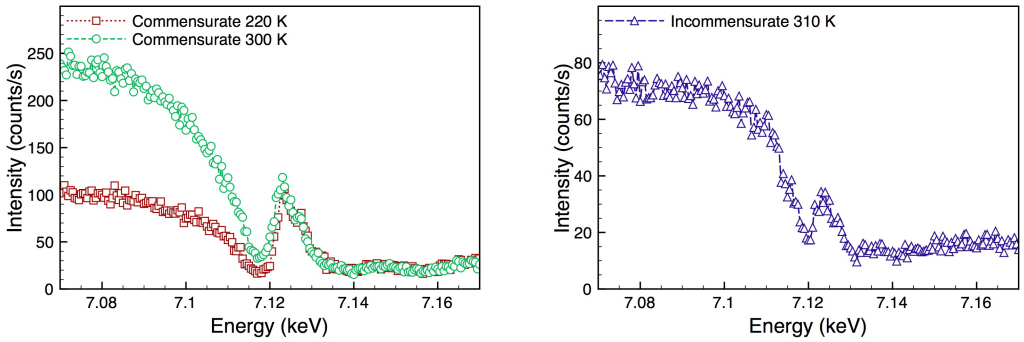

(a) (b)

Figure 3.20: Energy scans of the (a) $(-\frac{1}{2}, 3, 7)$ and (b) $(-\frac{1}{2}, 3, 7+\tau)$ reflections in the σ-σ' channel, measured at fixed wavevector. The shape of the incommensurate reflection remained constant in energy over the whole incommensurate temperature range. Results collected on XMaS, ESRF.

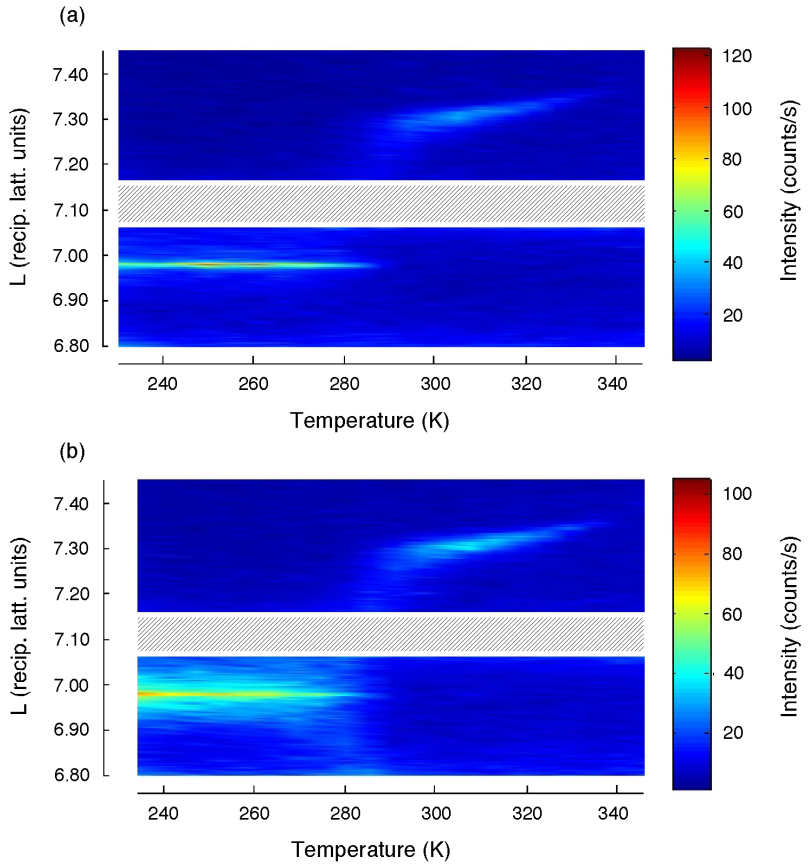

Figure 3.21: Temperature dependence on cooling of the $(-\frac{1}{2}, 3, 7)$ and $(-\frac{1}{2}, 3, 7+\tau)$ reflections in the σ-σ' channel, measured (a) off-resonance and (b) on-resonance at 7.070 keV and 7.123 keV respectively. The sample was cooled at a rate of 0.2 K/minute. The hashed area contains contamination from a powder reflection. Results collected on XMaS, ESRF.

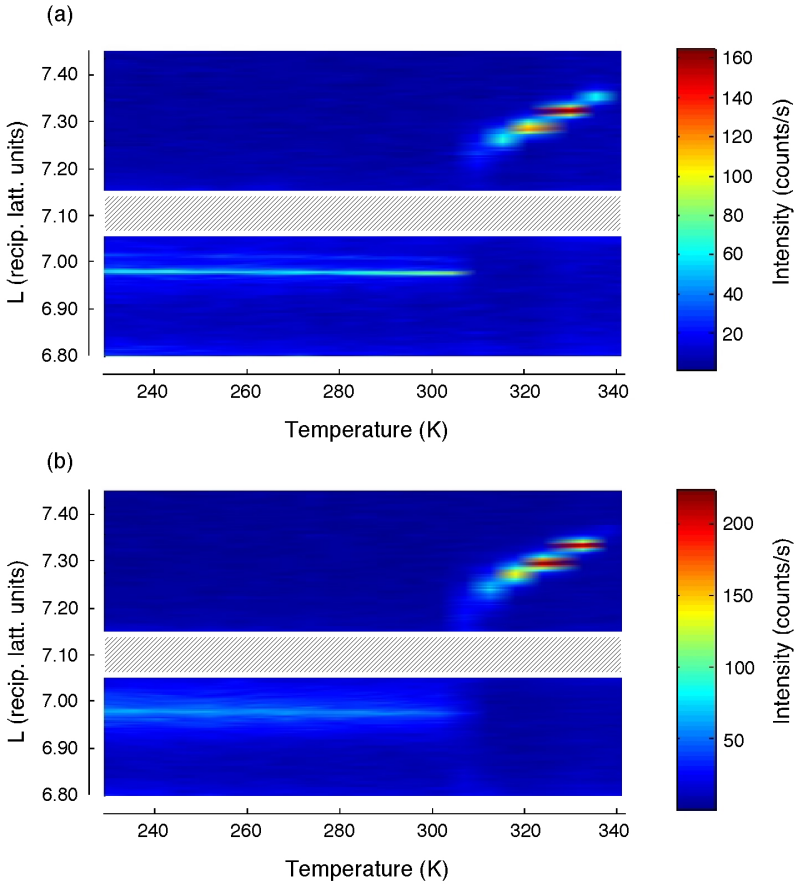

Figure 3.22: Temperature dependence on warming of the $(-\frac{1}{2}, 3, 7)$ and $(-\frac{1}{2}, 3, 7+\tau)$ reflections in the σ-σ' channel, measured (a) off-resonance and (b) on-resonance at 7.070 keV and 7.123 keV respectively. The sample was warmed at a rate of 0.2 K/minute. The hashed area contains contamination from a powder reflection. Results collected on XMaS, ESRF.

al. [112], with $T_{\rm CO}$ = 340 K and the commensurate-incommensurate transition, $T_{\rm CM-ICM}$ = 290 K. Figure 3.22 clearly establishes $T_{\rm CM-ICM}$ on warming as 310 K. This behaviour is consistent with the hysteretic behaviour observed in resistivity measurements [112]. The sample was not given any additional time to equilibriate as in the ID20 experiment, and so even in the *commensurate* phase, a slight incommensurability remains.

3.3.1 Polarisation Analysis

By considering the maximum analyser leakthrough of 0.6% we find that for all reflections, except ($\frac{1}{2}$, 0, 6), the resonant component measured in the π' channel is not merely leakthrough, but contains a component genuinely from this channel. This also appears to apply to the (0 0 7) reflection, in which the dominant component is the rotated σ-π' channel, but in which there appears to be some genuine σ-σ' component. To assess this apparent anisotropy several reflections were subjected to full polarisation analysis. In the first experiment, using the thinner phase plate, the (0 0 7), ($\frac{1}{2}$, 0, 6) and ($-\frac{3}{2}$, 2, 6) reflections were studied, with the results shown in figures 3.23 and 3.24. From figure 3.23 it is clear that almost all of the signal was in the rotated channel for the (0 0 7) reflection, and the small σ-σ' component evident from the energy scan is effectively negligible. Figure 3.24(a) confirms that the resonant ($\frac{1}{2}$, 0, 6) reflection was entirely isotropic, and that the rotated component was analyser leakthrough as expected. Meanwhile figure 3.24(b) for the ($-\frac{3}{2}$, 2, 6) reflection displays a very different behaviour, demonstrating a shift away from the centre, and a large non-linearly polarised component at 75°. It is important to point out that while this shifted non-linearly polarised component may be real, we do not believe that the large non-linearly polarised component seen in figure 3.24(a) at 90° is a genuine non-linear component, as we are scattering close to 90° in 2θ. As the intensity in the π' channel for isotropic scattering has a $\cos^2(2\theta)$ dependence, the genuine intensity is very low when 2θ is close to $90°$, and a systematic error is introduced into the measurement. This also applies to the polarisation dependencies which follow.

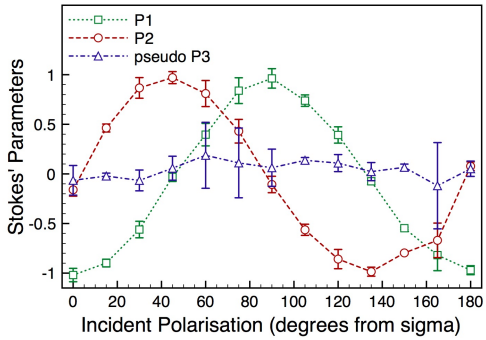

Figure 3.23: Linear polarisation analysis for the (0 0 7) reflection, measured at 220 K at 7.122 keV (on-resonance), using a 720 μm phase plate. Results collected on ID20, ESRF.

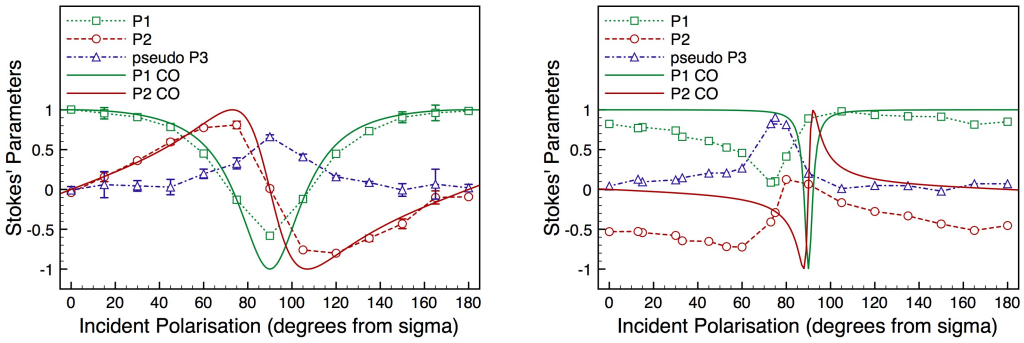

(a) (b)

Figure 3.24: Linear polarisation analysis of (a) the ($\frac{1}{2}$, 0, 6) and (b) the ($-\frac{3}{2}$, 2, 6) reflections, measured on-resonance at 220 K using the 720 μm phase plate, at 7.122 keV and 7.1243 keV respectively. The solid lines show the expected behaviour for isotropic charge scattering. Results collected on ID20, ESRF.

To fully characterise the polarisation dependence, the sample was studied a second time, using the thicker phase plate. In this case the sample was studied both at the resonant energy, and at a lower energy, far from the absorption edge. The sample was also studied using circular polarised light, in order to firmly establish the phenomena of linear to circular conversion. The results for linearly polarised light are shown in figures 3.25 and 3.26. Here, it is clear that the central non-linearly polarised component is an artefact of working at 2θ angles close to 90°, as it is present off-resonance for all reflections. It is also clear that for all non-resonant reflections, the isotropic scattering model accurately describes the data. This is also true for two of the superlattice reflections observed on-resonance. However, the $(-\frac{1}{2}, 3, 7)$ reflection clearly shows a different polarisation dependence on-resonance, with a similar behaviour to the $(-\frac{3}{2}, 2, 6)$ reflection. Unfortunately it was not possible to collect high quality data for all reflections at both resonant and non-resonant energies using incident circularly polarised light. Nevertheless, data was successfully recorded for the (0 0 6) Bragg reflection and the anomalous $(-\frac{1}{2}, 3, 7)$ reflection, as shown in figures 3.27 and 3.28 respectively. The corresponding Stokes' parameters are given in table 3.5, as are the expected values for isotropic charge scattering. For incident circular polarisation, which is composed of σ and π light 90° out of phase, we expect that scattering close to a 2θ value of 90° will reduce the π' component significantly and result in a highly elliptically polarised scattered beam. In this case we see that below the resonant energy we obtain exactly the result that we expect. However, on-resonance we find that the scattered light is displaced, producing elliptically polarised light rotated away from the σ'-plane.

3.4 Analysis and Discussion

To address the question of charge ordering, the FDMNES code was implemented, using multiple scattering mode as in the previous chapter. Unfortunately, like magnetite, the issue of an unknown exact crystal structure at low temperature presents a problem. As discussed in regard to magnetite, the spectra can be very sensitive to

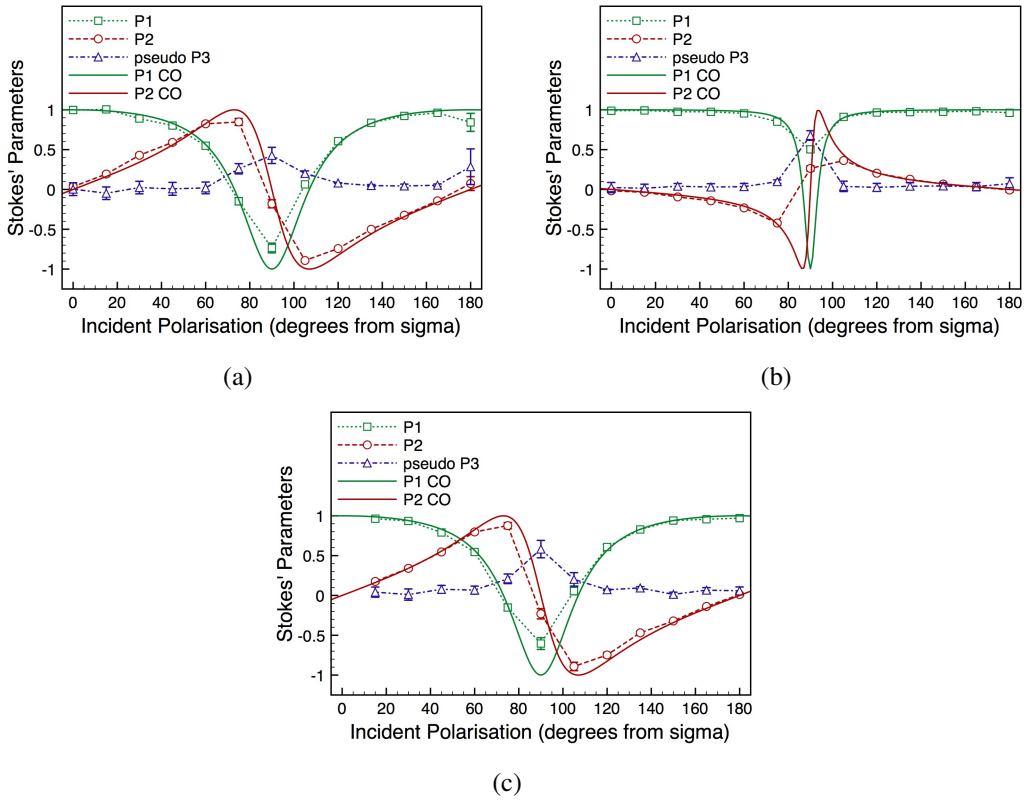

Figure 3.25: Linear polarisation analysis of the (a) ($\frac{1}{2}$, 0, 6), (b) ($-\frac{1}{2}$, 3, 7) and (c) ($\frac{1}{2}$, -1, 6) reflections, measured at 220 K, off-resonance at 7.0812 keV using the 1200 μm thick phase plate. The solid lines show the expected behaviour for isotropic charge scattering. Results collected on ID20, ESRF.

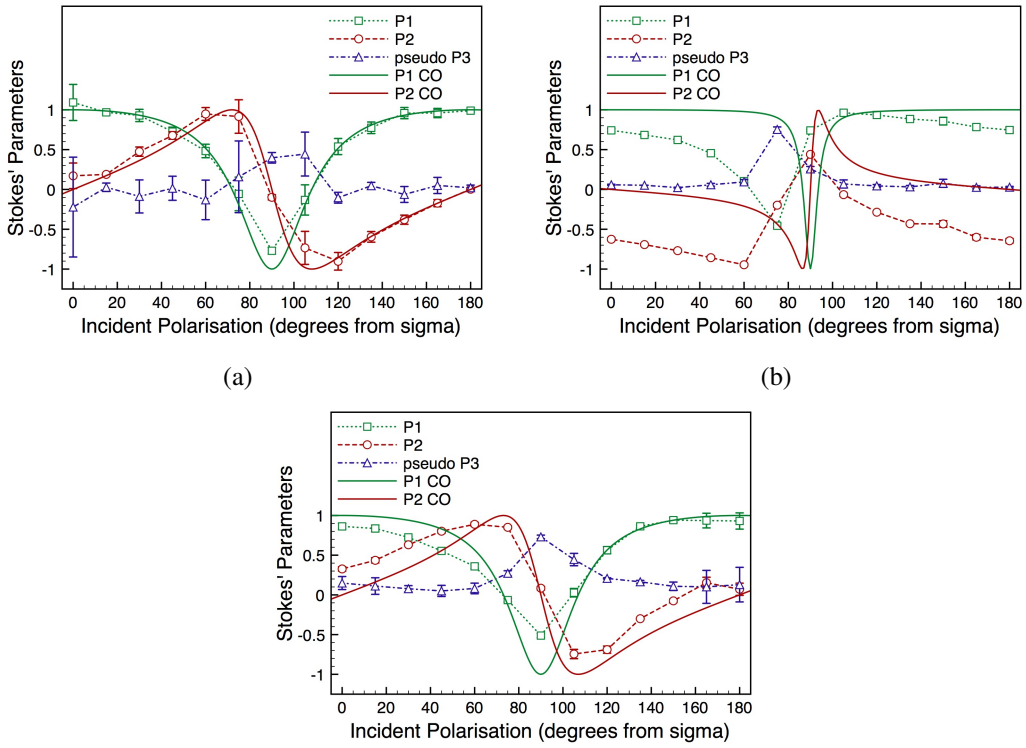

Figure 3.26: Linear polarisation analysis of the (a) ($\frac{1}{2}$, 0, 6), (b) ($-\frac{1}{2}$, 3, 7) and (c) ($\frac{1}{2}$, -1, 6) reflections, measured on-resonance at 220 K using the 1200 μm thick phase plate. Reflections (a) and (b) were measured at 7.1227 keV while (c) was measured at 7.1212 keV. The solid lines show the expected behaviour for isotropic charge scattering. Results collected on ID20, ESRF.

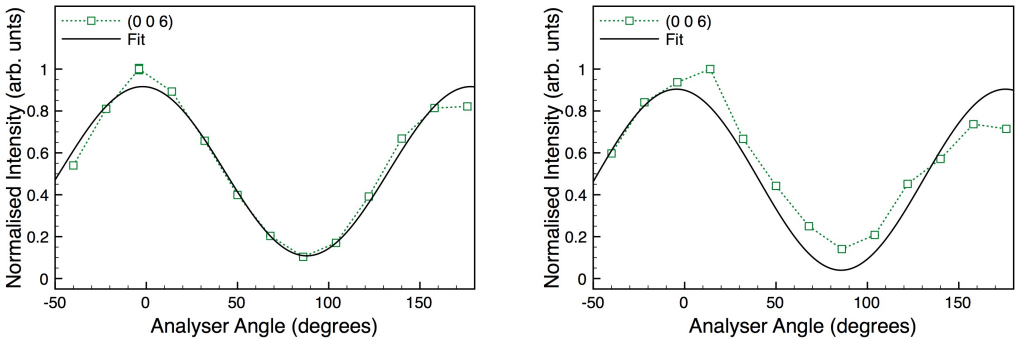

(a) (b)

Figure 3.27: Stokes' curve (equation 2.4) fit of the (0 0 6) Bragg reflection for incident circular polarisation, measured at 220 K (a) off-resonance and (b) on-resonance, at 7.08 keV and 7.1215 keV respectively. Results collected on ID20, ESRF.

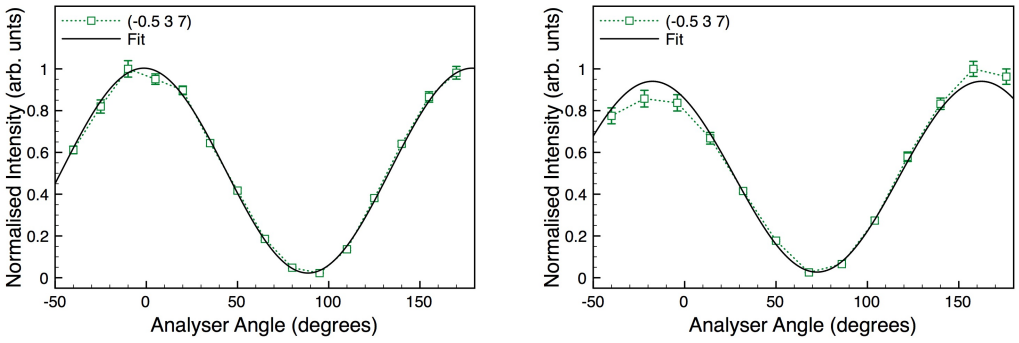

(a) (b)

Figure 3.28: Stokes' curve (equation 2.4) fit of the $(-\frac{1}{2}, 3, 7)$ reflection for incident circular polarisation, measured at 220 K (a) off-resonance and (b) on-resonance, at 7.0812 keV and 7.1227 keV respectively. Results collected on ID20, ESRF.

Table 3.5: Stokes' parameters for incident circular polarisation, measured off-resonance at 7.0812 keV and on-resonance at 7.1227 keV. The expected values for isotropic charge scattering are also shown.

Reflection	Measured P_1	Measured P_2	Iso. P_1	Iso. P_2
7.080 keV				
Main Beam	0.0081 ± 0.0069	-0.0420 ± 0.0064	0	0
(0 0 6)	0.786 ± 0.057	-0.056 ± 0.047	0.777	0
$(-\frac{1}{2}, 3, 7)$	0.955 ± 0.022	-0.0455 ± 0.017	0.989	0
7.121 keV				
Main Beam	0.0088 ± 0.0041	-0.0499 ± 0.0038	0	0
(0 0 6)	0.688 ± 0.087	-0.008 ± 0.073	0.787	0
$(-\frac{1}{2}, 3, 7)$	0.772 ± 0.054	-0.544 ± 0.050	0.993	0

the exact crystal structure as well as the charge disproportionation, and so without a highly accurate structure all of the predicted spectra are unlikely to simultaneously agree with all the experimental data. However, we can still expect to obtain compelling results regarding the physics of the system.

In this case the crystal structure obtained from x-ray diffraction experiments is an average over oppositely distorted charge ordered domains, and so not correct for either individual structure. In order to proceed we have thus applied the *up* and *zig* structures obtained from GGA+U calculations, provided by M. Angst *et al.* [112, 114]. An initial implementation of the FDMNES code using these structures, with full (1 e^-) and with no (0 e^-) charge disproportionation revealed some interesting results. When comparing to the observed reflections, we found that although all spectra did not agree well for any individual model, the *up* model was successful in predicting the existence of all the reflections. Indeed many of the resonant features were found to exist even in the absence of charge order, revealing some of them to have structural Templeton (ATS) components: in some cases almost entirely so. Specifically, resonances in the rotated σ-π' channel were routinely observed in the absence of charge order, while in the σ-σ' channel resonant features were sometimes present, but typically small. For the *zig* structure however, the simulations failed

to produce the ($\frac{1}{2}$, 0, 6) reflection σ-σ' component, while predicting a significant σ-π' component. These simulations also predicted a large non-resonant ($\frac{1}{2}$, 0, 7) reflection σ-σ' component and missed the resonant σ-π' component. The failure to correctly predict the existence/absence of these features is not a result of the exact structure being slightly incorrect, but demonstrates that the *zig/zag* structures with or without charge disproportionation cannot be correct.

In proceeding, only the *up* structure was studied, as the only plausible crystallographic structure. However, the magnitude of the oxygen distortions predicted by the GGA+U calculations is known to be approximately 10 $\%$ smaller than that observed in moving from the high temperature phase into the commensurate charge ordered phase. To produce a more accurate structure the oxygen positions were thus manually displaced away from their predicted positions, producing the best available structure. The simulations using this structure revealed that while some reflections were only weakly sensitive to charge order, and some only experienced changes of shape in the spectra with/without charge disproportionation, other reflections experienced much larger changes. Specifically the presence of any resonant enhancement was found to be almost entirely due to the charge disproportionation for the ($\frac{1}{2}$, 0, 6), ($-\frac{1}{2}$, 4, 7), ($\frac{1}{2}$, -1, 7), ($-\frac{1}{2}$, 3, 7) and ($-\frac{3}{2}$, 1, 6) reflections. In these initial simulations it became apparent that the size of the charge disproportionation is related to the relative size of the resonant feature in the σ-σ' channel, with large disproportionations producing a more pronounced resonant enhancement. From this perspective the observation of a decreasing resonant feature upon warming for the ($-\frac{1}{2}$, 3, 7) reflection, relative to the non-resonant component, suggests that the size of the charge disproportionation decreases on warming. This is in agreement with the increased electron hopping observed in prior studies. This also explains the difference in some of the results between the experiments carried out on ID20 and XMaS. As shown in figure 3.29 there is a distinction between the energy spectra of the ($-\frac{1}{2}$, 3, 7) reflection, with the resonant feature being significantly less prominent in the spectra measured at XMaS. This difference is most likely a result of the extremely slow dynamics associated with this system. During the experiments on

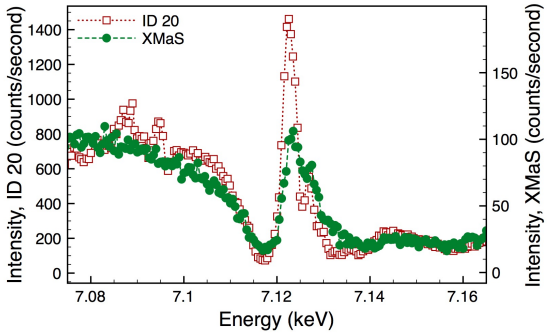

Figure 3.29: Energy scans of the $(-\frac{1}{2}, 3, 7)$ reflection in the σ-σ' channel, measured at 200 K at fixed wavevector. Results collected on ID20 and XMaS, ESRF.

ID20 the sample was given adequate time to equilibriate, whereas time restrictions during the XMaS experiment meant that measurements were taken immediately after cooling. If the resonance is a result of the charge order, as we believe it is for the $(-\frac{1}{2}, 3, 7)$ reflection, then the reduced intensity of the resonance relative to the non-resonant pre-edge demonstrates that the maximum charge disproportionation takes time to form. This is exactly what is expected based upon the observed change in the widths of the charge order reflections with time, figure 3.12, and explains the difference in correlation lengths between the ID20 and XMaS experiments. We also note that the gradual development of the charge order ground state is seen in the position of the reflections, which only become fully commensurate after an extended period of time.

One interesting result is the difference in the peak profiles along the L direction, below and at the resonant energy, figures 3.19(a). Of course there is often a broadening of reflections across an absorption edge, due to the reduction in the attenuation length of the incident x-rays. However, in this case we expect the attenuation length below and above the edge to be 33 μm and 5 μm respectively. This is considerably greater than the correlation lengths reported in table 3.4. The broadening on-resonance could therefore be a result of one of two phenomena. Either the charge order that we are specifically sensitive to on-resonance is less correlated than the structural distortion, or the charge order is less correlated within the first 5 μm

of the surface than it is in the bulk of the crystal. The second option is the far more likely, as the crystal distortions and the charge order are fundamentally linked, and it is doubtful that the two phenomena would have such different correlation lengths.

Of the five reflections whose spectra show a large dependence on the charge order, four were selected for use in estimating the charge disproportionation. The $(\frac{1}{2}, -1, 7)$ reflection was omitted as the experimental spectra differed from all others, by having a resonance that was lower in energy: a result which was not predicted by simulation. The simulations used a 6 Å cluster radius, containing approximately 91 atoms, and only the E1-E1 excitation channel was included. It was found that a 6 Å radius provided an adequate compromise between accuracy and time, while the E1-E2 and E2-E2 components were found to have no noticeable effects. The two formally Fe^{3+} ions were constrained to have equal disproportionations, and were allowed to vary between $Fe^{2.5+}$ and Fe^{3+}, while the formally Fe^{2+} ions were also constrained together and allowed to vary between Fe^{2+} and $Fe^{2.5+}$, simultaneous to the Fe^{3+} ions. The result of the simulations is shown in figure 3.30. In all cases the intensities have been normalised to the off-resonant components, and the energy is calibrated using the fluorescence measurement, figure 3.31. Here we can see that while the full 1 e^- disproportionation typically overestimates the resonant contribution, removing the charge order underestimates it. Applying a charge segregation of $\delta = 0.2$ produces a reasonable agreement with experiment, but still underestimates the resonance in several cases. Allowing the program to vary the charge order results in the best fit when $\delta = 0.37$, the results of which are shown in figure 3.32. It is clear that the fitted spectra do not perfectly match the experimental spectra, as the ratio between the resonant and non-resonant features is not exact, and in all cases the higher energy feature is over estimated. However, there is clearly a strong agreement between simulation and experiment. The key features are replicated, and only in the case of the $(-\frac{3}{2}, 1, 6)$ reflection is the resonant enhancement over estimated. As a result we are unable to determine an exact charge disproportionation between the formally Fe^{2+} and Fe^{3+} sites. However, we are able to estimate the upper and lower bounds of the disproportionation as 0.4 e^-

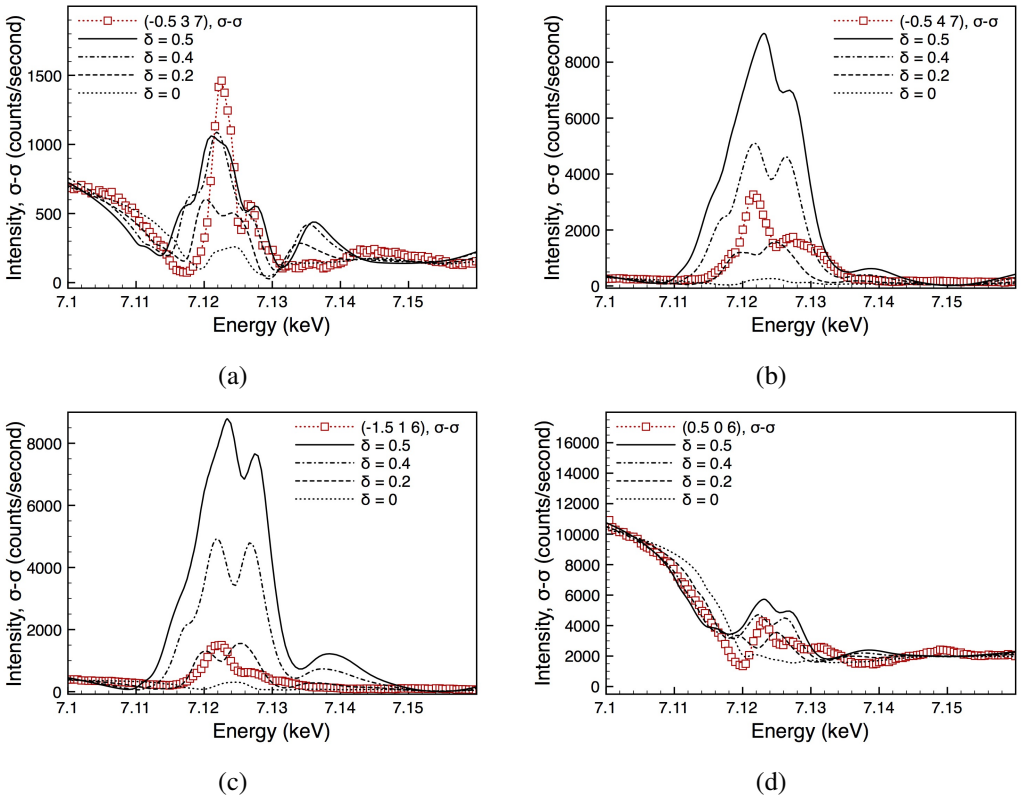

Figure 3.30: FDMNES simulations of the (a) $(-\frac{1}{2}, 3, 7)$, (b) $(-\frac{1}{2}, 4, 7)$, (c) $(-\frac{3}{2}, 1, 6)$ and (d) $(\frac{1}{2}, 0, 6)$ reflections, showing the effect of charge disproportionation on the resonance. The simulations use the *up* structure, and apply iron valencies of $+2.5 \pm \delta$. Results collected on ID20, ESRF.

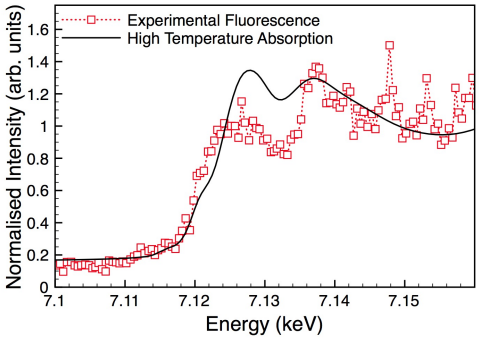

Figure 3.31: Fluorescence measurement across the iron K edge. The measurement was not ideal, but still allows the edge position to be determined accurately, as can be seen when compared to the FDMNES predicted room temperature absorption spectrum. Results collected on ID20, ESRF.

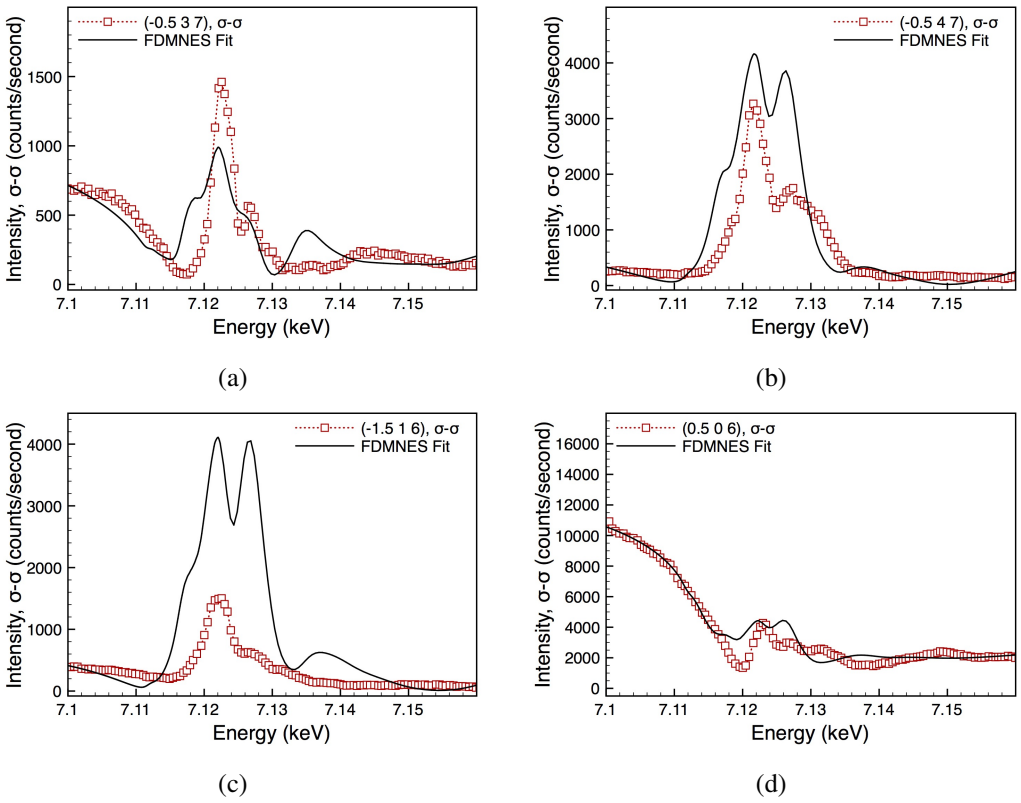

Figure 3.32: FDMNES simulations of the (a) $(-\frac{1}{2}, 3, 7)$, (b) $(-\frac{1}{2}, 4, 7)$, (c) $(-\frac{3}{2}, 1, 6)$ and (d) $(\frac{1}{2}, 0, 6)$ reflections, showing the best simultaneous fit to all four reflections. The simulations use the *up* structure, and apply iron valencies of $+2.5 \pm 0.366$. Results collected on ID20, ESRF.

and 0.8 e^- ($0.2 \leq \delta \leq 0.4$). Thus Fe_2OBO_3 is not a fully ionically charge ordered system, although the charge disproportionation appears to be larger than the majority of other charge ordered iron oxides, such as magnetite and the perovskite ferrates [27].

Considering the polarisation dependencies, we first turn to the (0 0 7) reflection, which we believe to be an ATS reflection, due to the width of the reflections matching the Bragg peaks, the rotation of the incident polarised light, and the fact that we can predict the existence of the reflection using FDMNES in all phases regardless of charge order. In the high temperature $Pmcn$ orthorhombic structure the site symmetry at the two inequivalent iron sites is the m_x mirror plane. Equivalent iron sites are related by two-fold rotations around axes parallel to the three orthorhombic axes. The resultant scattering tensor for the (0 0 7) reflection is then given by,

$$\hat{S}_{ATS}^{(0\ 0\ 7)C} = \begin{pmatrix} 0 & 0 & 0 \\ 0 & 0 & Q_{yz} \\ 0 & Q_{yz} & 0 \end{pmatrix}. \tag{3.1}$$

Upon reduction to the monoclinic $P2_1/c$ structure of Attfield *et al.*, the iron site symmetry is lost and the scattering tensor is modified to

$$\hat{S}_{ATS}^{(0\ 0\ 7)C} = \begin{pmatrix} 0 & Q_{xy} & 0 \\ Q_{xy} & 0 & Q_{yz} \\ 0 & Q_{yz} & 0 \end{pmatrix}. \tag{3.2}$$

Figure 3.33 clearly demonstrates that the high temperature structure is sufficient in explaining the polarisation dependence of the (0 0 7) reflection, as using only the Q_{yz} components in the model accurately reproduces the experimental result. This is of course not surprising as the monoclinic distortion is not large, and so any distortion in the xy-plane would have to be big in order to have an effect. This is in contrast to the case of Fe_3O_4, where the additional terms were required, indicating that in magnetite these terms were substantial, while in Fe_2OBO_3 they are not. Obviously the charge ordered *up* structure has even lower symmetry than the Attfield *et*

al. structure, however it is not necessary to consider the lowest symmetry structure in relation to the polarisation dependence of the (0 0 7) reflection, as it is clear that the higher symmetry structure is sufficient.

For the remainder of the reflections, we have found that off-resonance all of the reflections demonstrate a clear isotropic charge scattering dependence, figure 3.25. This is exactly what we expect for scattering from the scalar Thomson terms. At the resonant energies, we see that for the majority of reflections, isotropic scattering still provides an excellent description of the measured dependence, figures 3.24 and 3.26. This is again expected, as on-resonance we expect the dominant terms to be the isotropic resonant components, along with an isotropic non-resonant (Thomson) contribution. However, as described in the last section, the contribution in the π' channel is often larger than expected for isotropic scattering, even though this contribution is still very small. For the $(-\frac{3}{2}, 2, 6)$ reflection a deviation is seen from the isotropic behaviour, but it is only when studying the $(-\frac{1}{2}, 3, 7)$ reflection, where the polarisation dependencies at and below the resonant energy are compared using both linear and circular light, that such a difference can fully be appreciated. Why is it that such a phenomenon is seen for these two reflections, and not the others surveyed? Although all of the reflections surveyed have high 2θ values, ranging from $2\theta \approx 70 - 90°$, the specific reflections in question have $2\theta \approx 90°$. Thus, for these reflections the isotropic scattering components are highly attenuated in the π' scattered channel, allowing the anisotropic terms to be observed. It is the interference between these terms which results in the unconventional dependence. Simulations using the FDMNES code using the charge disproportionantion determined above, of $\delta = 0.37$ produced a good agreement with the observed result shown in figure 3.34. Interestingly, figure 3.34 reveals that such an effect is not reliant on the charge disproportionation, although in this case the simulation including charge disproportionation clearly produces a better agreement. Figure 3.35 confirms that the off-resonance component behaves exactly as expected, while the charge ordered structure closely replicates the measured non-linearly polarised contribution.

Using FDMNES we have found that the biggest single change to the non-

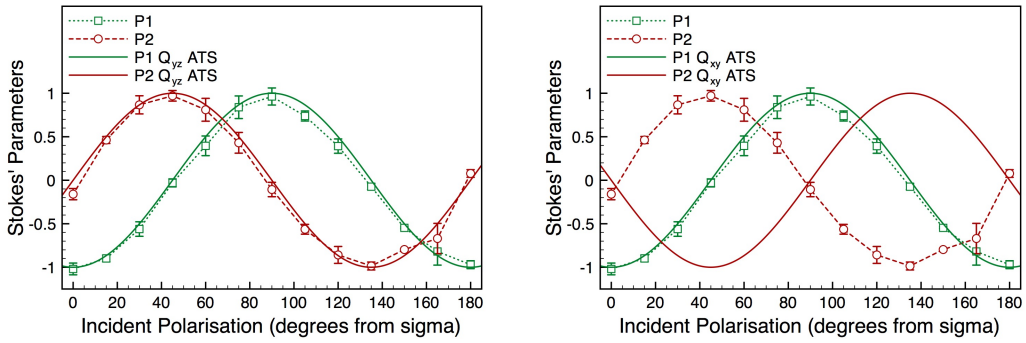

(a) (b)

Figure 3.33: Linear polarisation analysis for the (0 0 7) reflection, measured at 220 K at 7.122 keV, using the 720 μm phase plate. The solid lines show the expected behaviour for an ATS reflection in the high temperature structure, with either the (a) Q_{yz} or (b) Q_{xy} components only. Results collected on ID20, ESRF.

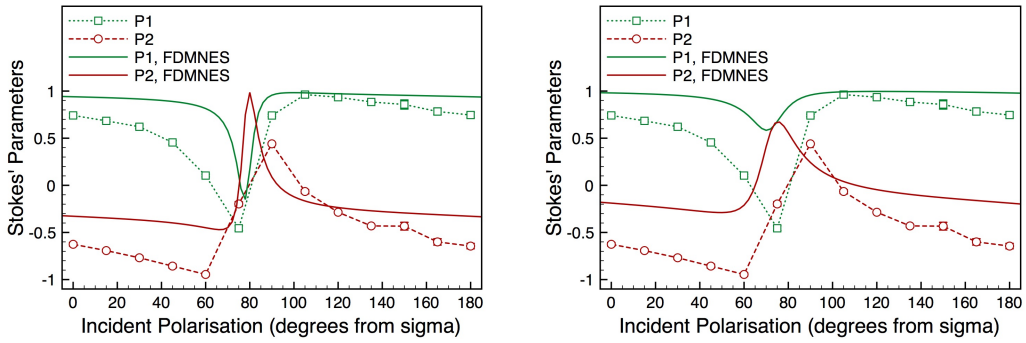

(a) (b)

Figure 3.34: Comparison between the experimental and simulated polarisation dependencies for the $(-\frac{1}{2}, 3, 7)$ reflection (a) with and (b) without charge ordering, with both simulations at 7.1227 keV (on-resonance). Results collected on ID20, ESRF.

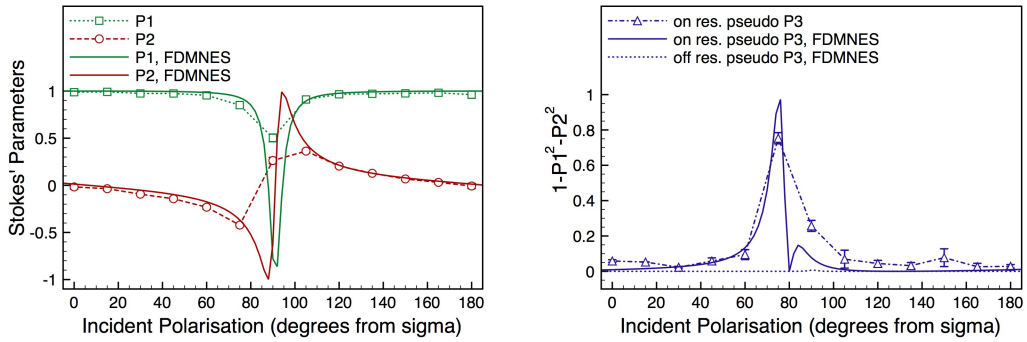

(a) (b)

Figure 3.35: FDMNES simulations of (a) the polarisation dependence of the $(-\frac{1}{2}, 3, 7)$ reflection off-resonance and (b) the *pseudo* P_3 component both on- and off- resonance at 7.1227 and 7.0917 keV respectively. Results collected on ID20, ESRF.

linearly polarised contribution occurs when the non-resonant component is excluded from the simulation. This indicates that interference between the anomalous and Thomson terms has the dominant role in the conversion of linearly to non-linearly polarised light. Even without the Thomson terms, we still find a significant non-linearly polarised signal. The effect which is still present even when individual sublattices are considered. In fact, we find that the only way to suppress the non-linearly polarised component entirely is to artificially remove the structural anisotropy around the resonating sites by removing the surrounding oxygens. We therefore surmise that there is some contribution to the non-linearly polarised scatter due to interference between the anomalous isotropic and anisotropic components. Of course we expect the interference between the four iron sublattices to play a part; however, unlike for the $(0, 0, \frac{9}{2})_C$ reflection in magnetite, this is clearly only one of several contributions.

3.5 Conclusions

In this comprehensive study of Fe_2OBO_3 at the iron K edge a number of important results have become apparent. Before this analysis it was clear that there were nu-

merous effects associated with the rate of warming and cooling: namely the *freezing in* of incommensurate reflections and the hysteretic nature of the resistivity. Here, we have demonstrated hysteresis of the charge order reflections and observed the development of slightly incommensurate reflections within the formally commensurate phase, which eventually condense into commensurate reflections. We have also observed the resonant enhancement of a feature almost entirely associated with charge order diminish with respect to the Thomson scattering on warming. This indicates that there is a reduction in the magnitude of the charge disproportionation, up until the system enters the incommensurate phase. Beyond this point the disproportionation remains constant until the charge order breaks down at high temperatures.

Using simulations generated by the FDMNES code we have found that the *zig* (*zag*) structure cannot generate all of the observed reflections, while the *up* (*down*) structure can be used to qualitatively simulate all results. Although we have been unable to assign an accurate value to the charge segregation, we are able to estimate the disproportionation as being between 0.4 and 0.8 e^-. Thus we have demonstrated that despite some previous reports to the contrary, Fe_2OBO_3 is indeed charge ordered, but not fully ionic. As in the case of magnetite, we have demonstrated that under certain conditions we can observe a non-linearly polarised component to the scattered beam. We have confirmed this using incident circularly polarised light. Through simulations we find that the effect appears to primarily result from interference between the Thomson and anomalous components; however, like magnetite, interference between the sublattices plays an important role, and the local anisotropy is critical.

We are unable to replicate the spectra exactly due to the uncertainty of the exact low temperature crystal structure, however, our results replicate the key features. We stress that this is the first RXD study of iron oxyborate, which is a comparatively understudied material. Once the structure can be determined more accurately, the data contained herein may be re-examined, to more exactly determine the charge disproportionation.

Chapter 4

Bilayer Manganite, $Pr(Sr_{0.1}Ca_{0.9})_2Mn_2O_7$

4.1 Background

There has been intense interest in the manganite perovskites due to the wealth of phenomena they demonstrate. As discussed in Chapter 1, these materials belong to the Ruddlesden-Popper series, with perhaps the most famous member being the colossal magnetoresistive compound $(La_{0.4}Sr_{0.6})_3Mn_2O_7$ [6]. Here, the resistivity can be forced to decrease by two orders of magnitude through the application of a magnetic field. The key principle responsible for this change in resistivity, is the double exchange (DE) mechanism, although competition from other phases also plays a key part [6, 116]. The double exchange mechanism was proposed in these materials by Zener [117], and extended by Anderson and Hasegawa [118] and De Gennes [119]. The mechanism allows conduction across the manganese ions by allowing them to hop from one to another, via an oxygen ion with which they are strongly hybridised. It is the e_g electrons, which are directed toward the oxygen atoms (see figure 1.4) that take part in this, and so the rate of hopping is related to the orbital occupation in the system. However, such an effect is only possible if the spins on the two manganese ions are parallel, and hence the application of a

magnetic field can result in DE mediated conduction.

Charge order and orbital order represent the other key topics within the manganite systems. Again, the layered materials are of particular interest as they are highly two-dimensional systems, with a long c-axis measuring approximately 20 Å. By doping in divalent elements, such as strontium, holes are added, which aid the conductivity and allow charge ordering at sufficient concentrations. As discussed in Chapter 1, the checkerboard charge and orbital stripe patterns are generally the most stable within the tetragonal structure of the layered manganites. In these materials the direction of the equivalent orbital stripes is split between domains, with ordering wavevectors of ($\frac{1}{4}$, $\frac{1}{4}$, 0) and ($-\frac{1}{4}$, $\frac{1}{4}$, 0) [120]. Due to its orthorhombic structure, $Pr(Sr_{1-y}Ca_y)_2Mn_2O_7$ instead experiences preferential orbital stripe orientation. The most studied of this series is the $y = 0.9$ compound, in which the orbital stripes were first detected. The structure of this material in the charge disordered phase is shown in figure 4.1. Unlike the majority of bilayer perovskites, this material is orthorhombic in all phases, with spacegroup $Amam$ (No. 63) and lattice parameters $a = 5.410$ Å, $b = 5.462$ Å and $c = 19.277$ Å above 370 K [121]. For simplicity all indexing is performed with respect to this structure.

Below 370 K the material enters the so-called CO1 phase, in which the material becomes charge ordered and the structure changes to $Pbmn$ (No. 53) with lattice parameters $a = 5.411$ Å, $b = 10.921$ Å and $c = 19.234$ Å. This transition is clear in resistivity measurements, as shown in figure 4.2(a). Bond valence sum calculations indicate that the charge disproportionation between the formally Mn^{3+} and Mn^{4+} is 39% [122]. X-ray and optical conductivity measurements have detected the simultaneous formation of orbital stripes with the charge order [121]. As shown in figure 4.3, additional spots with a wavevector of (0, $\frac{1}{2}$, 0) appear below T_{CO1}, associated with the Jahn-Teller distortions coupled to the orbital order. No additional spots are associated with the charge order, as the charge ordered unit cell is equivalent to the high temperature crystallographic unit cell, due to the orthorhombic structure.

Below 300 K on cooling (or 315 K on warming) the material enters the CO2 phase, and the structure changes to $Am2m$ (No. 38) with lattice parameters $a =$

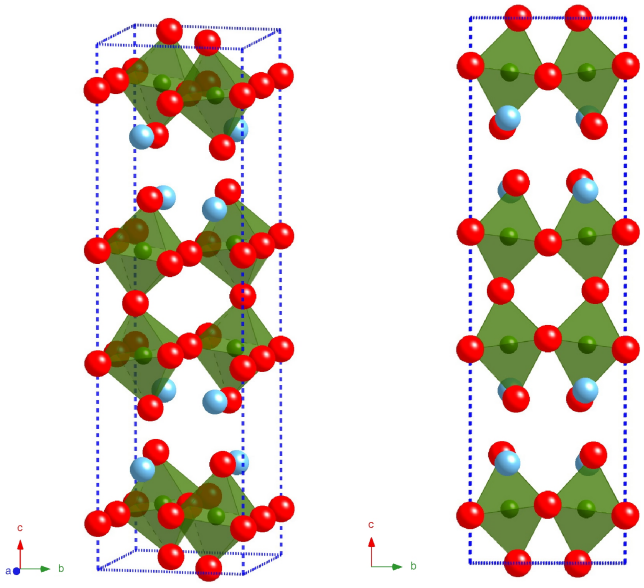

(a) (b)

Figure 4.1: Crystal structure of $Pr(Sr_{0.1}Ca_{0.9})_2Mn_2O_7$ above the charge ordering transition. The manganese sites are green, the oxygen sites are red, and the Pr/Sr/Ca sites are blue. The tilting of the octahedra around the a-axis and along the b-axis, is clearly visible in (b). There is no such tilting around the b-axis.

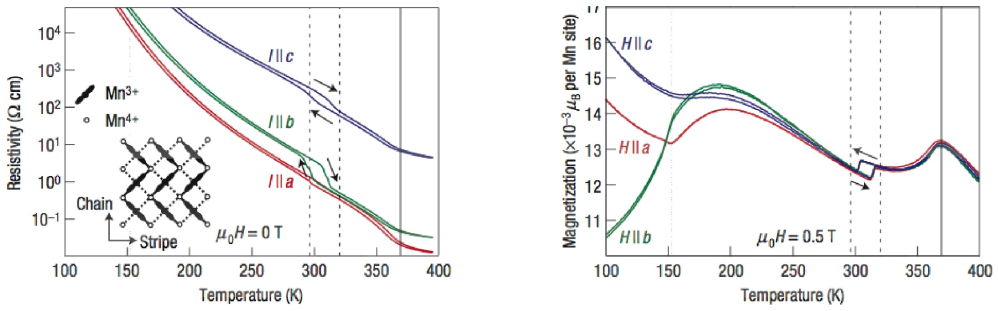

(a) (b)

Figure 4.2: The temperature dependence of (a) the resistivity and (b) the magnetisation in a field of 0.5 T in $Pr(Sr_{0.1}Ca_{0.9})_2Mn_2O_7$, measured by Tokunaga *et al.* Reprinted by permission from Macmillan Publishers Ltd: Nature Materials, reference 121, copyright 2006.

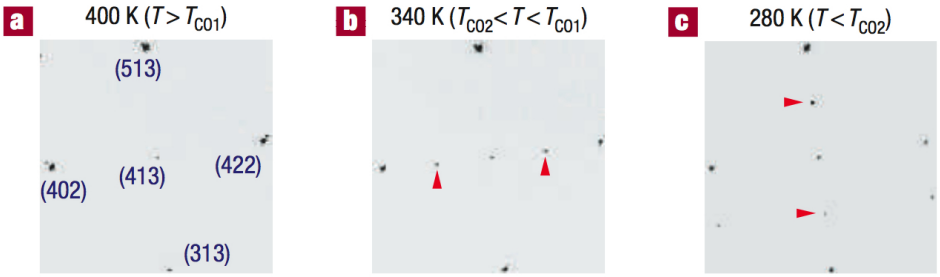

Figure 4.3: X-ray oscillation photographs of $Pr(Sr_{0.1}Ca_{0.9})_2Mn_2O_7$, taken (a) above and (b & c) within the charge-orbital ordered phases, by Tokunaga *et al.* Superlattice spots from the orbital stripe phases are indicated. Reprinted by permission from Macmillan Publishers Ltd: Nature Materials, reference 121, copyright 2006.

10.812 Å, $b = 5.475$ Å and $c = 19.203$ Å. The change in lattice parameters, and the transitions for different dopings are shown in figure 4.4. As is clear by comparing figures 4.3(b) and (c), the superlattice spots move to different directions. The new spots possess a wavevector of $(\frac{1}{2}, 0, 0)$, indicating a switch in the direction of the orbital stripes. The charge order remains unchanged however, maintaining the checkerboard configuration with a charge disproportionation of 39 % [122]. Two further transitions occur at $T_N = 153$ K and $T_S \approx 90$ K. At T_N the system becomes a CE-type antiferromagnet, and at T_S undergoes a structural transition [121]. So far little has been reported about the transition at T_S, other than an apparent change from an orthorhombic to monoclinic structure, due to a rotation of the MnO_6 octahedra [121].

For $y \leq 0.4$ only short range charge order is present, while at all dopings of $y > 0.4$ long range charge and orbital order is present. The preferential orbital occupation appears to be of $3x^2 - r^2/3y^2 - r^2$ type orbitals (*i.e.* $3d_{x^2}/3d_{y^2}$ ordering) [124], using the nomenclature of the local cubic frame, as shown schematically in figure 4.5. The transition into the CO2 phase is clearly visible in magnetisation and resistivity measurements, figure 4.2. In the resistivity measurements a significant anisotropy is evident, as the largest jumps in resistivity are along the a and b-axes at T_{CO1} and T_{CO2} respectively. This indicates that current flow along the stripes

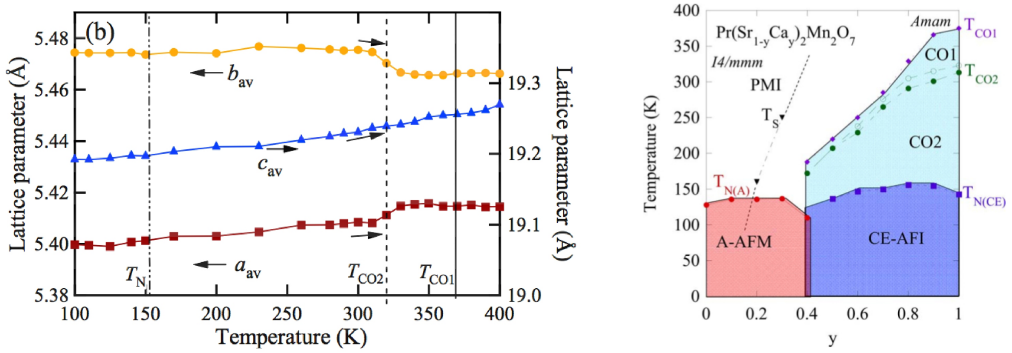

(a) (b)

Figure 4.4: (a) Variation of the lattice parameters with temperature around the charge and orbital order transitions in $Pr(Sr_{0.1}Ca_{0.9})_2Mn_2O_7$ by Tokunaga *et al.* (b) Phase diagram of the $Pr(Sr_{1-y}Ca_y)_2Mn_2O_7$ series, principally based upon resistivity and magnetisation measurements, by Tokunaga *et al.* T_s shows the tetragonal to orthorhombic structural transition. CE-AFI and A-FM refer to insulating and metallic antiferromagnetic phases respectively. Reprinted figures with permission from references 123 and 124 respectively. Copyright 2008 by the American Physical Society.

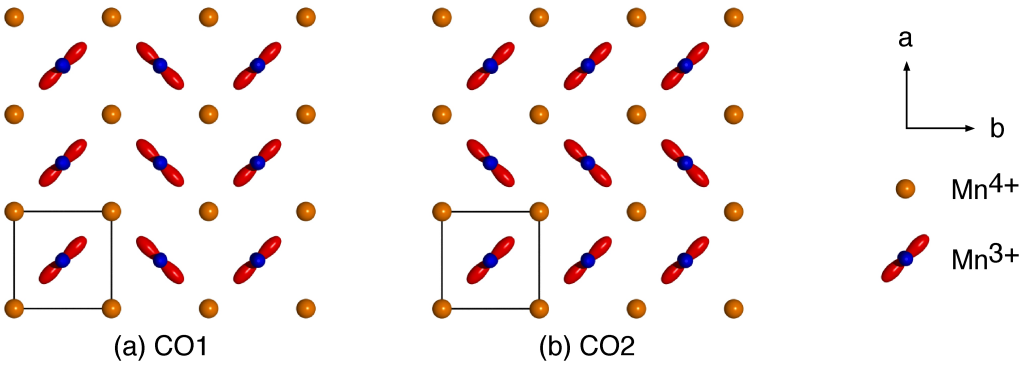

Figure 4.5: The direction of the orbital stripes in the (a) CO1 and (b) CO2 phases in $Pr(Sr_{0.1}Ca_{0.9})_2Mn_2O_7$. The solid line shows the high temperature crystallographic unit cell.

is generally more difficult than along the zig-zag chain direction, which is unsurprising when we consider the directions of the orbital lobes and the DE interaction [116]. The optical conductivity also shows a dramatic anisotropy, as shown in figure 4.6. While there is clearly no directional dependence at high temperatures, the anisotropy is clear below T_{CO1}, as is the reversal between the CO1 and CO2 phases. As pointed out by Lee *et al.*, this must be a result of the orbital stripe rotation, rather than the structural change, as the differences in the lattice between CO1 and CO2 are small, with the a-axis being smaller than the b-axis in all phases (when indexed in the $Amam$ setting) [125].

In contrast to the majority of results, recent TEM measurements performed by Li *et al.* have found evidence for the coexistence of both $(\frac{1}{2}, 0, 0)$ and $(0, \frac{1}{2}, 0)$ reflections between T_{CO1} and T_{CO2} in a non-twinned sample [126]. This was assigned to the formation of a checkerboard orbital phase. Below T_{CO2} only $(\frac{1}{2}, 0, 0)$ reflections survive, indicating the conventional stripe orbital order.

To understand the effect of the mismatched a and b lattice parameters on the orbital rotation, the sample has also been studied under uniaxial stress applied along the b-axis [123]. Here, it was found that by applying stress, the stability of the CO2 phase could be altered, as shown in figure 4.7. The lack of effect on T_{CO1} is not surprising, as there is only a small change in lattice parameters along the b-axis at T_{CO1}. Meanwhile, there is a larger change in lattice parameters at T_{CO2}, resulting in a significant effect on T_{CO2} when stress is applied. Nevertheless T_{CO2} remains below T_{CO1}, even when the b-axis is forced to be the shorter axis above ≈ 75 MPa [123].

As is clear in figure 4.1(b), there is significant tilting of the octahedra along the b-axis, as a result of the small average size of the A-site cations [121]. This distortion is key to stabilising the charge and orbital order, as it impedes the DE electron hopping [121, 123]. However, in combination with the charge order, the distortion also leads to an electric polarisation, as shown in figure 4.8. Within the CO1 phase $Pr(Sr_{0.1}Ca_{0.9})_2Mn_2O_7$ becomes antiferroelectric, while in the CO2 phase the material becomes ferroelectric. Below T_{N} the material is thus multiferroic. As the

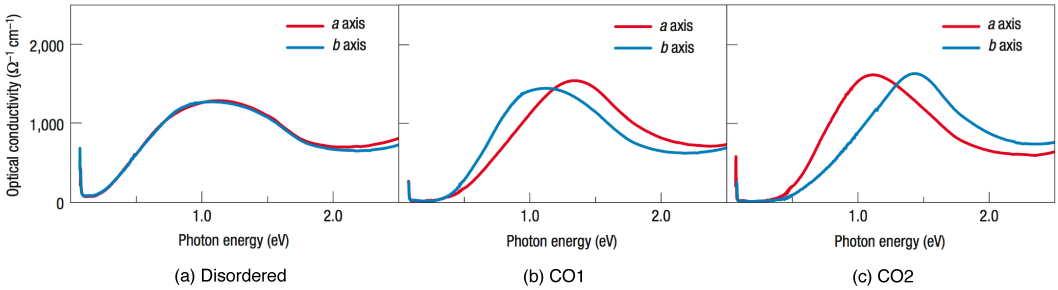

Figure 4.6: Measurements of the anisotropy in the optical conductivity in $Pr(Sr_{0.1}Ca_{0.9})_2Mn_2O_7$, taken (a) above and (b & c) within the charge and orbital ordered phases, at 424, 323 and 320 K respectively, by Tokunaga *et al.* Reprinted by permission from Macmillan Publishers Ltd: Nature Materials, reference 121, copyright 2006.

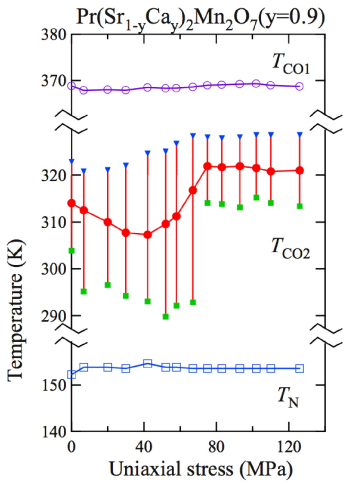

Figure 4.7: Dependence of the phase transition temperatures with uniaxial stress applied along the b-axis in $Pr(Sr_{0.1}Ca_{0.9})_2Mn_2O_7$ by Tokunaga *et al.* The filled triangles and squares represent the transition temperatures on cooling and warming, determined from magnetisation measurements. The filled circles represent the centre of the thermal hysteresis. Reprinted figure with permission from reference 123. Copyright 2008 by the American Physical Society.

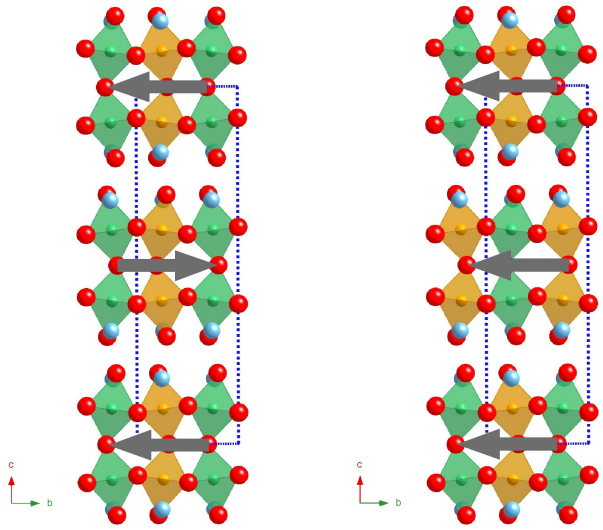

(a) (b)

Figure 4.8: Structure of $Pr(Sr_{0.1}Ca_{0.9})_2Mn_2O_7$ in the (a) CO1 and (b) CO2 phases in $Pr(Sr_{0.1}Ca_{0.9})_2Mn_2O_7$. The Mn^{3+} sites are green, the Mn^{4+} sites are orange, the oxygen sites are red, and the Pr/Sr/Ca sites are blue. The grey arrows show the polarisation direction of each bilayer.

ferroelectric polarisation is coupled to the distortion, inverting the lattice parameters through uniaxial stress leads to a switching of the ferroelectric polarisation direction [124]. Recently polar domains have been found to form in bulk samples of the material, separated by domain walls which are charged due to the antiparallel arrangement of the domains [127].

The purpose of our study was to directly confirm the presence of orbital order within $Pr(Sr_{0.1}Ca_{0.9})_2Mn_2O_7$ by using the technique of soft x-ray resonant diffraction. By doing so we hoped to confirm the orbital structure, as well as assess any changes to the structure and size of the charge disproportionation. Such changes may be important to the multiferroicity in this compound, and so a full understanding of the local structure around the manganese ions is vital.

The following results have previously been published in references 128 and 129.

4.2 Sample Preparation and Experimental Technique

The techniques used to study the orbital and structural order in $Pr(Sr_{0.1}Ca_{0.9})_2Mn_2O_7$ were highly contrasting soft x-ray resonant diffraction and high energy non-resonant x-ray scattering methods.

Soft x-rays, typically defined in the 125 eV to 2500 eV region, are strongly absorbed by air. These experiments must be carried out under ultra high vacuum, and ideally with no absorbing elements between the source, the sample and the detector. This generally takes place in a vacuum of below 1×10^{-7} mbar in order to avoid the problem of ice formation on the sample surface at low temperatures. The principal problem with soft x-ray diffraction is the small size of the Ewald sphere, which greatly limits the number of reflections which are accessible. In fact, for the majority of transition metal oxides this means that only one or two superlattice reflections can be accessed, while no Bragg reflections can be reached unless at least one of the lattice parameters is exceptionally large. Samples to be used in soft x-ray diffraction experiments must therefore be carefully aligned using hard x-rays prior to a soft x-ray experiment, such that the superlattice reflections can be found relatively quickly. The favoured technique is to prepare the crystal with the desired reflection perpendicular to the back of the sample, such that once the sample is fixed down, the required wavevector is normal to the mounting surface. The scattering surface is ideally prepared such that there is a small ($\approx 5^\circ$) miscut from the back of the sample, such that any specular scattering will not directly coincide with the required reflection.

The sample of $Pr(Sr_{0.1}Ca_{0.9})_2Mn_2O_7$ was grown using the floating zone method, and aligned on a rotating anode generator. The sample was found to be twinned such that the a and b-axes were parallel in separate domains. However, rather than attempt to separate the twins into independent crystals, the sample was prepared such that both axes could be studied together. A small miscut was ground into the sample, several degrees away from being perpendicular to the twinned a/b-axis, to avoid the specular reflection. The sample was then polished using diamond suspensions, down to 0.25 μm, to produce a high quality surface for scattering.

To study the twin populations, hard x-rays were used on XMaS to characterise the prepared sample. There was some population difference of the two twins, found by scanning over the sample surface with a small beam, although the total populations appeared approximately equal. Typical scans over the sample are shown in figure 4.9.

The beamlines ID08 at the ESRF, and I06 at DLS (Diamond Light Source) were used to perform the soft x-ray experiments. ID08 typically uses two APPLE II undulators to generate x-rays at any arbitrary polarisation, through the use of four independent undulator jaws, with a tuneable energy between 0.3 and 1.6 keV [130]. However, only a single undulator was used in this experiment. Hard x-rays are then rejected by a silicon double-bounce mirror, before the soft x-rays are focussed horizontally and vertically [131]. Alternative mirrors can be used to improve harmonic rejection, depending on the energies used, and the intensities required. A diffraction grating acts as a monochromator, the resolution of which is primarily determined by the slit size before and after the grating [131]. When measuring the incident spectra the energy resolution was increased to ~ 0.2 eV, but at all other times was relaxed to ~ 0.5 eV. The beam size at the sample measured up to $1300\ \mu$m $\times\ 150\ \mu$m with open slits. The I06 branch beamline is similar, offering a slightly wider energy range between 0.08 and 2.1 keV, but with similarly selectable polarisation states [132]. The beam is monochromated and focussed, with a much smaller beam, in the region of $200\ \mu$m $\times\ 20\ \mu$m. At the ESRF the machine was operated in *7/8 + 1* mode, with a current of 200 mA [88], while at DLS the machine was operated in a 600 bunch custom mode, with a current of 225 mA.

The ID08 diffraction chamber is shown in figure 4.10. The chamber houses a five-circle diffractometer which possesses the standard four motions, plus a γ translation of the detector out of the diffraction plane. The sample is cooled using a helium flow cryostat, which is attached to the sample mounting block via a copper braid. This allows temperatures down to ≈ 17 K to be reached. At I06 the Daresbury diffraction chamber was used [133]. The Daresbury chamber contains only the vertical θ and 2θ circles, with an additional γ translation out of the diffraction

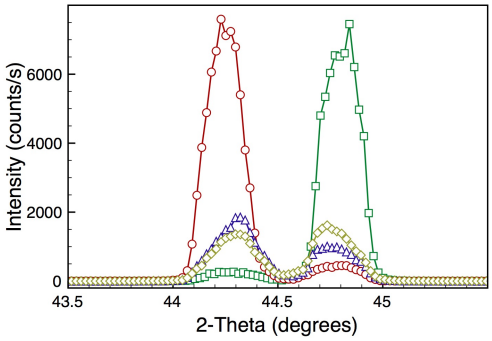

Figure 4.9: θ-2θ scans through the (0 8 0) and (8 0 0) Bragg reflections in the twinned sample of $Pr(Sr_{0.1}Ca_{0.9})_2Mn_2O_7$ measured at room temperature using an energy of 9.26 keV, at different points on the sample surface, using a 100 μm $\times$ 300 μm beam. Results collected on XMaS, ESRF.

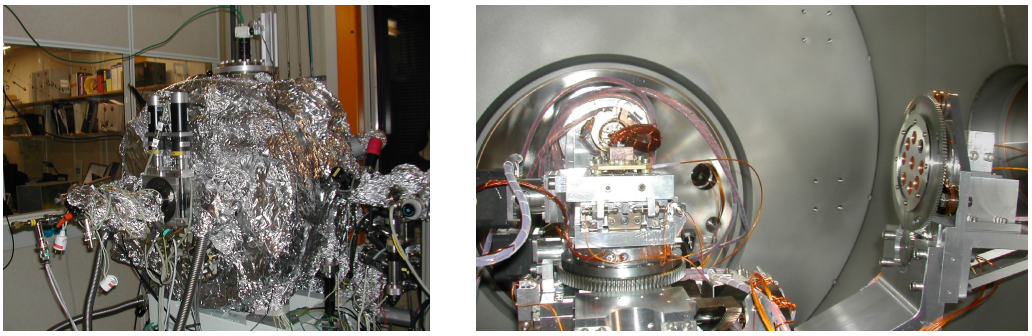

(a) (b)

Figure 4.10: (a) The ID08 diffraction chamber and (b) the *in-vacuo* diffractometer. The sample is located on the copper block on the left side of (b), while the detector slits and the 2θ arm are visible on the right.

plane. However, for this experiment an attocube piezorotator was added to provide a ϕ rotation. The sample was cooled using a Joule-Thomson closed-cycle Displex helium cryostat, providing a minimum sample temperature of ≈ 100 K whilst using the attocube. A photodiode was used as a detector, in both chambers. Unfortunately photodiodes are not ideal, due to their low efficiency in the soft x-ray region. Only small currents generated by the incident x-rays, meaning that the electronic noise inherent to the system can be problematic. There is also the problem of visible light contamination to contend with, hence all view ports into the chamber must be well covered while measurements are being taken. However, once a reflection has been located and maximised, these problems are generally manageable.

Additional structural measurements were carried out at the high energy x-ray beamline BW5, at HASYLAB. The beamline uses a wiggler on the DORIS III ring to produced x-rays in the range 60-150 keV [134, 135]. DORIS III is a 4.45 GeV machine, which operates with a maximum current of 140 mA, using positrons rather than electrons. The beamline is shown in figure 4.11. A copper absorber between the wiggler and the beamline absorbs all energies below ~ 50 keV, before a silicon monochromator selects the required energy. In this study a Si/Ge graded monochromator was used instead, in order to reduce the energy resolution, but improve the incident x-ray flux. After scattering from the sample a silicon analyser is then used to remove fluorescence while simultaneously providing high spatial resolution. A germanium solid-state detector was then used, to provide actual photon counting of the diffracted signal.

X-rays with an energy of 100 keV were used in this study, which have a very high penetration depth. Therefore most of the scattering takes place within the bulk of the crystal, as x-rays penetrate the whole of the sample with ease. This also removes the problem of being obstructed by the horizon of the crystal, which together with the huge size of the Ewald sphere, means a large number of reflections can easily be reached at these energies. The sample was mounted beneath an aluminium dome and radiation shield, on a four-circle Huber diffractometer, connected to a Joule-Thomson closed-cycle Displex helium cryostat.

4.3 Results and Discussion

Through consideration of previous soft x-ray studies on bilayer manganites, the ($\frac{1}{2}$, 0, 0) orbital order reflection was searched for and found at an energy of 652 eV, at room temperature. The sample was then warmed into the CO1 phase, and the (0, $\frac{1}{2}$, 0) reflection was found. As can be seen in the inset of figure 4.17, the twinning of the crystal means that both reflections can be accessed, and easily resolved due to the separation of the reflections in 2θ. Due to the large incident beam size on ID08, a large area of the sample surface was illuminated, meaning that the twins were approximately equally probed, and so the relative intensities may be used comparatively. The sample was then warmed above T_{CO1}, over the hysteretic region. Energy scans of the reflections were collected in each phase, as shown in figure 4.12(a). It is immediately obvious from figure 4.12(a) that there is no dramatic change of the spectra at any temperature. Critically we see that the changes between the CO1 and CO2 phases are small, indicating there is no change in the type of occupied orbital during the rotation. It is clear there are some changes in the spectra, especially at low temperatures. However, all of the changes are gradual, and so rather than corresponding to any specific transition, the changes reflect small changes in the structure on cooling.

Castleton and Altarelli [136] have used atomic multiplet calculations to demonstrate the power of soft x-ray resonant diffraction in disentangling scattering contributions. By changing the magnitude and sign of the crystal field parameters, X^{400}, X^{420} and X^{220}, they have demonstrated that not only the type of orbital order, but also the size of the Jahn-Teller contribution to the scattering could be deduced. Such a change is shown for $La_{0.5}Sr_{1.5}MnO_4$ in figure 4.13, where the reduction of the Jahn-Teller distortion quickly suppresses the intense feature at the L_3 edge, while leaving the L_2 edge relatively unchanged apart from shifting the energy.

Wilkins *et al.* have studied the orbital and magnetic reflections in the bilayer manganite $LaSr_2Mn_2O_7$ [137]. In this study it was found that the Jahn-Teller distortion was small, with an extremely low value of the tetragonal crystal field parameter providing the best result, figure 4.14. The value used for X^{220} in figure 4.14

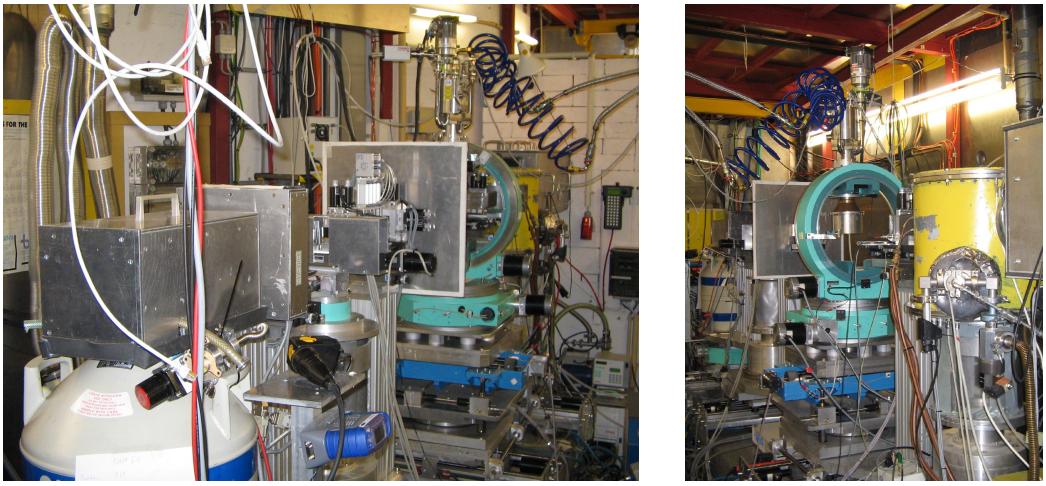

(a) (b)

Figure 4.11: The BW5 beamline viewed from (a) the detector and (b) the source ends. In (a) the liquid nitrogen dewar required to cool the germanium detector is prominent, while in (b) the diffractometer and the yellow chamber housing the monochromator are clear.

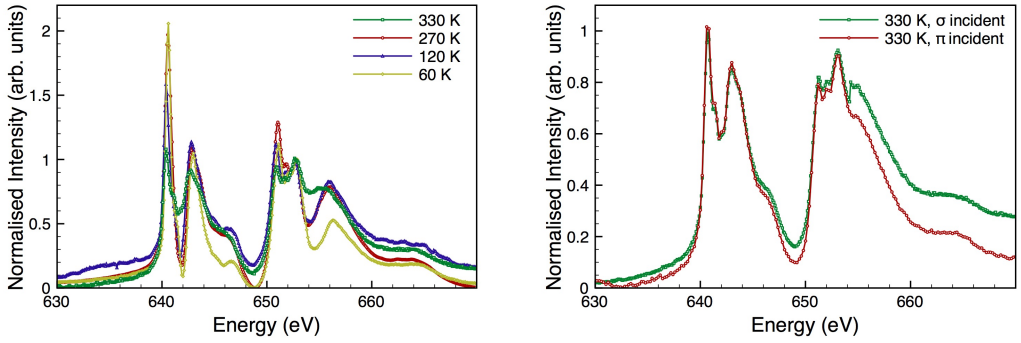

(a) (b)

Figure 4.12: (a) Energy scans at fixed wavevector of the (0, $\frac{1}{2}$, 0) reflection at 330 K and the ($\frac{1}{2}$, 0, 0) reflection at all other temperatures in $Pr(Sr_{0.1}Ca_{0.9})_2Mn_2O_7$ in the σ incident polarisation channel. (b) Normalised energy scans at fixed wavevector of the (0, $\frac{1}{2}$, 0) reflection in the σ and π incident polarisation channels, measured consecutively. Results collected on ID08, ESRF.

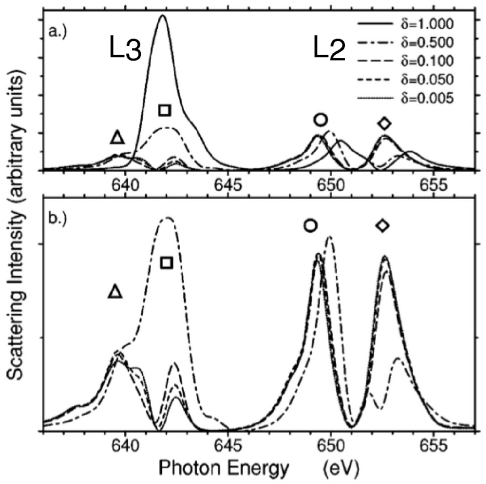

Figure 4.13: Change in the predicted spectra for an orbitally ordered manganite by Castleton and Altarelli. As δ approaches zero the size of the Jahn-Teller distortion decreases, while the system remains orbitally ordered as long as δ remains finite. Figure (b) is an enlargement of the smaller δ results shown in (a). Reprinted figure with permission from reference 136. Copyright 2000 by the American Physical Society.

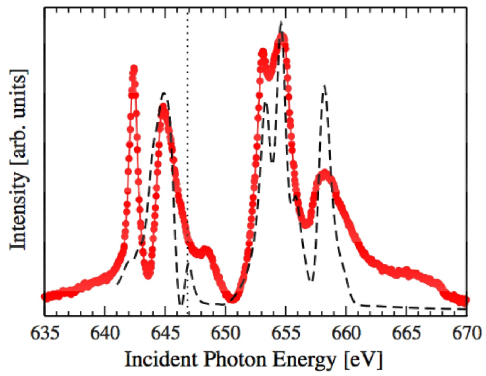

Figure 4.14: Energy scan at the orbital order/Jahn-Teller wavevector in $LaSr_2Mn_2O_7$ by Wilkins *et al.* The simulation is shown as a dashed line, while the experiment is shown as red circles. Reprinted with permission from IOP Publishing: J. Phys.:Condens. Matter, reference 137, copyright 2006.

was positive, which may indicate $x^2 - z^2/z^2 - y^2$ rather than $3x^2 - r^2/3y^2 - r^2$ orbital order. However, the authors comment that the value used was very small, such that the crystal field was almost cubic, and so an accurate determination of the orbital occupation was not possible in this case. As is clear in figure 4.15, the spectra observed in $Pr(Sr_{0.1}Ca_{0.9})_2Mn_2O_7$ are incredibly similar to the orbital order reflections measured by Wilkins *et al.* in $LaSr_2Mn_2O_7$, and so it is reasonable to extrapolate that the Jahn-Teller distortions in $Pr(Sr_{0.1}Ca_{0.9})_2Mn_2O_7$ are also small. Unfortunately deducing the type of orbital order is again equally inaccurate. However, we are able to say that the reflections are predominantly due to orbital order in both phases. By comparing the σ and π incident polarisation channels, figure 4.12(b), we can confirm that there is no additional charge or magnetic component to the scattering, as the spectra are almost identical, apart from a small change in intensity.

In order to confirm the orbital origin of the reflections, the azimuthal dependence was studied in both phases. The sample was visually aligned within the diffraction chamber such that at $\phi = 0, \theta = 0$ the c-axis of both twins was in the same direction as the incident x-ray beam. Each reflection was then maximised and scanned at each azimuthal position, with the resultant integrated intensity shown in figure 4.16. The anisotropy of the reflections is expected to be principally due to the shape of the orbital lobe, rather than the surrounding ion coordination, as we would expect at the manganese K edge. As such, rather than construct the scattering tensor from crystallographic symmetry constraints, we may simply apply the scattering tensor for a non-magnetic anisotropic uniaxial environment (such as for the $3x^2 - r^2/3y^2 - r^2$ orbitals). This is given by Blume [46] as

$$\hat{S}^0 = \begin{pmatrix} n_a^2 - \frac{1}{3} & n_a n_b & n_a n_c \\ n_a n_b & n_b^2 - \frac{1}{3} & n_b n_c \\ n_a n_c & n_b n_c & n_c^2 - \frac{1}{3} \end{pmatrix}, \tag{4.1}$$

where $\mathbf{n}$ gives the optical axis. These tensors for each site can then be substituted

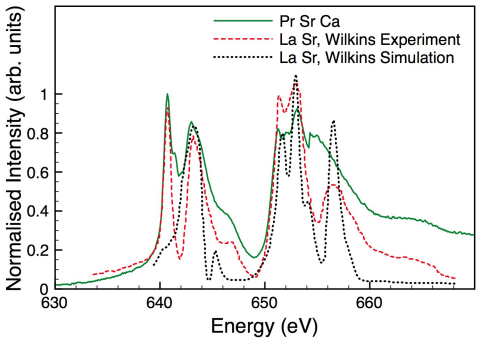

Figure 4.15: Comparison between the energy spectra measured in our study of $Pr(Sr_{0.1}Ca_{0.9})_2Mn_2O_7$ and $LaSr_2Mn_2O_7$ by Wilkins *et al.* [137]. The green solid line shows the measurement of $Pr(Sr_{0.1}Ca_{0.9})_2Mn_2O_7$ at 330 K, using σ incident polarisation. Results collected on ID08, ESRF. The red and black lines show the experimental and calculated results for $LaSr_2Mn_2O_7$ [137]. The data sets have been normalised in intensity and shifted in energy for comparison.

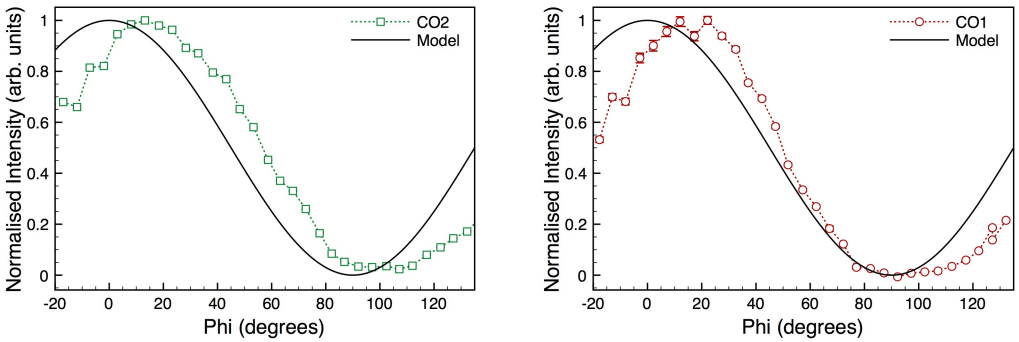

(a) (b)

Figure 4.16: Azimuthal dependence of (a) the $(\frac{1}{2}, 0, 0)$ reflection and (b) the $(0, \frac{1}{2}, 0)$ reflection, measured at 652 eV with σ incident polarisation at 140 K and 327 K respectively. The solid lines represent models of the orbital stripe structures. Results collected on I06, DLS.

into the structure factor to give

$$\hat{S}_{OO}^{(0,\,\frac{1}{2},\,0)/(\frac{1}{2},\,0,\,0)} = \begin{pmatrix} 0 & Q_{xy} & 0 \\ Q_{xy} & 0 & 0 \\ 0 & 0 & 0 \end{pmatrix}, \tag{4.2}$$

for both reflections. Hence the models in figure 4.16 based on the CO1 and CO2 structures are identical. The azimuthal dependencies demonstrate that the reflections possess the expected anisotropy originating from orbital order. Several scans were also conducted using π incident polarisation, producing identical results, as expected. However, there is clearly some offset between the expected and experimental behaviour in figure 4.16, of approximately 10-15°. This is almost certainly a systematic error resulting from the incorrect alignment of the sample, which was performed optically and manually, from the side of the chamber. The alternative possibility is that the difference is genuine, although this would suggest that there is some canting of the orbitals away from a high symmetry direction, which is unlikely.

The temperature dependence of both orbital order reflections was then measured on warming and cooling, at an energy of 652 eV, figure 4.17. The onset of CO1 is visible at approximately 360 K: 10 K lower than the previously established T_{CO1} temperature. However, this is most likely due to the low intensity of the reflection, making exact determination difficult. Surprisingly, we observe some coexistence of the CO1 and CO2 reflections down to T_{CO2}. This may correspond to the checkerboard orbital order speculated by Li *et al.* [126]; however, we doubt such a checkerboard structure, as we would expect this orbital arrangement to have a wavevector of $(\frac{1}{2}, \frac{1}{2}, 0)$ rather than simultaneous $(\frac{1}{2}, 0, 0)$ and $(0, \frac{1}{2}, 0)$ reflections. An alternative possibility is that the coexistence could be the result of the thermal gradient across the sample. However, it is unlikely that such a large temperature gradient could be present over the sample for such an extended period. Instead, the more likely explanation is of some microscopic phase separation [138], where small regions of each phase coexist in competition within discrete regions of the crystal, in the absence of

any appreciable thermal difference.

Aside from the change in T_{CO2} on warming and cooling, small differences in the relative intensity on cooling and warming are also apparent, indicating that the thermal history is not solely limited to the 310-315 K region. However, the most important differences in intensity are those between the CO1 reflection and the CO2 reflection at low temperature. As discussed above, the large beam size means that both twins are probed (approximately) equally, meaning the difference is a real observation, and not an artefact from the twinning. The diffraction signal represents the contrast in the density of states between orbitally ordered sites. A greater occupancy of the formally Mn^{3+} $3d$ orbitals can cause such an increased contrast. Now, when we also consider that there are no large changes in the spectra with temperature, indicating no significant changes in the orbital-type or local manganese environments, it becomes clear that this change in intensity represents a change in the valence of the orbitally ordered sites. The previous BVS calculations [122] which saw a 39% charge disproportionation in both phases were conducted just above and below T_{CO2}, and so it is not necessarily surprising that such a change has not been reported before.

Despite not being directly sensitive to the charge disproportionation at this wavevector, as it is only the orbital order (on the formally Mn^{3+} sites) which we probe, a greater charge disproportionation is implied, as a higher electron density on the formally Mn^{3+} sites implies a lower electron density on the formally Mn^{4+} sites. Like magnetite and iron oxyborate, we do not expect full ionic charge disproportionation, and so such a change is not necessarily unexpected. If this is the case, then the formally Mn^{4+} sites also possess some e_g character, and we may expect these orbitals to also be ordered. However, such a contribution is expected to be smaller than from the formally Mn^{3+} contribution, due to the smaller contrast between orbital states. Finally we point out that the temperature dependence of the intensity appears to agree well with the temperature dependence of the second-harmonic generation measured by Tokunaga *et al.* [121], indicating that the orbital order is the order parameter responsible for the ferroelectric polarisation

At low temperatures the sample is well correlated, with a correlation length of ≈ 600 Å up to T_{CO2}, at which point the correlation length of the CO2 phase drastically reduces by approximately halving. As we see from figure 4.18, both orbital structures are relatively stable on warming, and both possess smaller correlation lengths than the CO2 structure below T_{CO2}. The CO1 structure shows a sharp drop in correlation length at T_{CO1}, which is in contrast to the gradual transition seen in regard to the intensity, figure 4.18(b). This indicates that the transition is not associated with a melting of the charge/orbital order, but a genuine decrease in the charge contrast until total collapse at T_{CO1}.

As soft x-rays have a low penetration depth, it is important to consider whether the value of 600 Å reported above is a real measurement, or an artefact of the high attenuation length of soft x-rays. In this case, the attenuation length of x-rays above the manganese L_2 edge is ~ 850 Å, meaning that the observed correlation length is not limited in this manner. However, the peak lineshapes possess a lineshape which is slightly more Lorentzian in shape, as opposed to the Lorentzian squared expected for a signal which is limited by the correlation length. For a signal limited by the optics of the beamline we expect a Gaussian lineshape. The Lorentzian lineshape observed in this case indicates that the signal is close to being limited by the beamline optics. Nevertheless, the observed lineshape still provides an accurate measurement of the correlation length.

The intensity and width of a CO2 type reflection were also studied on BW5 using high energy (100 keV) x-rays. Figure 4.19(a) shows the temperature dependence of the ($\frac{5}{2}$, 0, 0) reflection, which shows some surprising results when compared to the ($\frac{1}{2}$, 0, 0) reflection measured with soft x-rays. Although these are different reflections, they are along the same direction, and so we expect the results to be equivalent. Firstly the integrated intensity shows a maximum at ~ 225 K, secondly, the intensity shows a far more gentle decrease than seen with soft x-rays, and thirdly the correlation length appears much shorter than previously determined. The lineshapes appear to be Gaussian, indicating that they are limited by the resolution of the beamline, thus explaining the reduced correlation length. This is

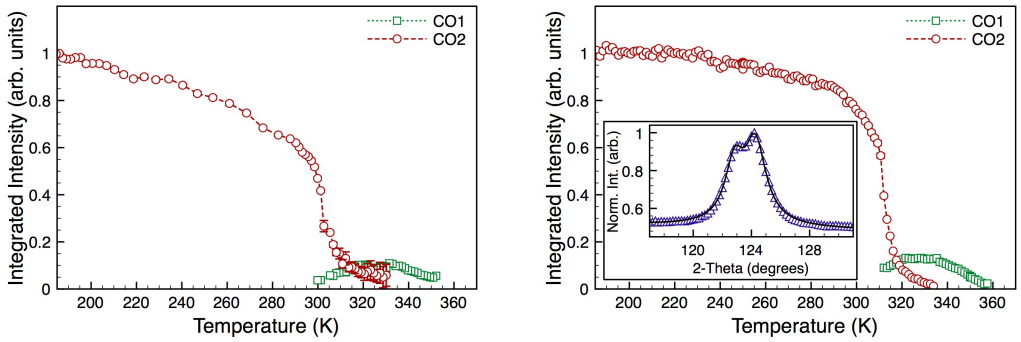

(a) (b)

Figure 4.17: Temperature dependence of the ($\frac{1}{2}$, 0, 0) and (0, $\frac{1}{2}$, 0) reflections, measured at 652 eV on (a) cooling and (b) warming. Inset: θ-2θ scan through the CO1 (0, $\frac{1}{2}$, 0) and CO2 ($\frac{1}{2}$, 0, 0) reflections at 316 K on warming. The solid lines show Lorentzian fits. Results collected on ID08, ESRF.

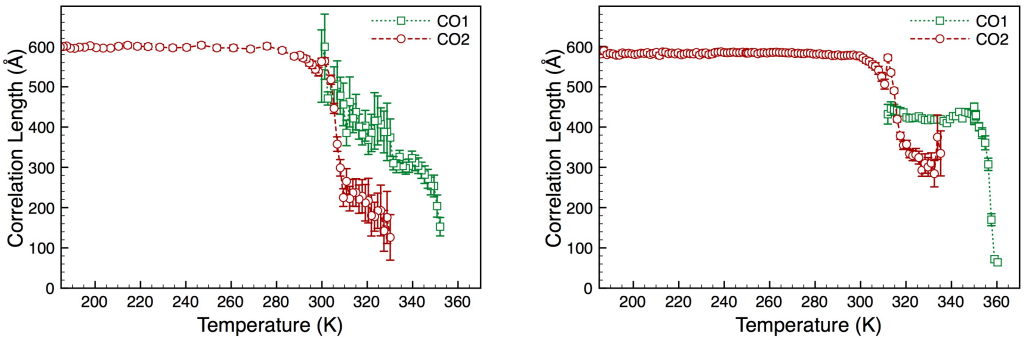

(a) (b)

Figure 4.18: Temperature dependence of the correlation length of the CO1 (0, $\frac{1}{2}$, 0) and CO2 ($\frac{1}{2}$, 0, 0) reflections, measured at 652 eV on (a) cooling and (b) warming. Results collected on ID08, ESRF.

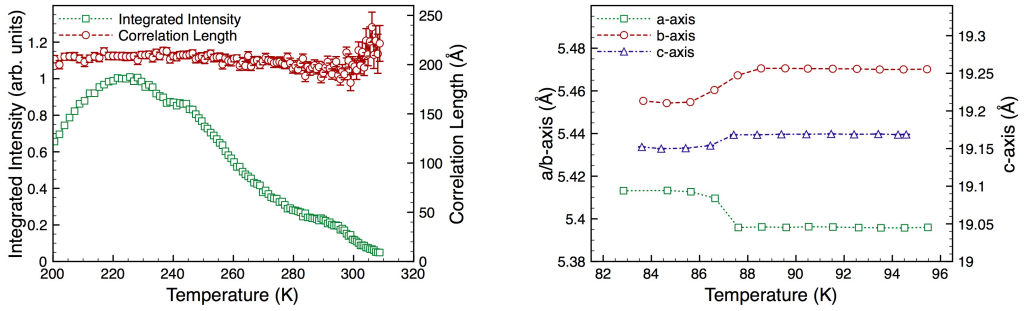

(a) (b)

Figure 4.19: (a) Temperature dependencies of the integrated intensity and correlation length of the ($\frac{5}{2}$, 0, 0) reflection on warming. (b) Temperature dependencies of the lattice parameters on warming through the T_S transition. Both dependencies were measured using high energy x-ray diffraction. Results collected on BW5, HASYLAB.

unsurprising as the graded monochromator used to improve intensities greatly reduces the resolution compared to the pure silicon monochromator. This does not explain the unexpected intensity dependence though. It is possible that the measurement is genuine, as at high energies (and off-resonance) we no longer probe the orbital order directly, but instead probe the weak Jahn-Teller distortions. However, the Jahn-Teller distortions should be closely coupled to the orbital occupation, and so such a large difference is unlikely. A remaining possibility is of experimental error, although no such problem is obvious.

Finally we studied the low temperature structural transition, using both hard and soft x-rays. The change in lattice parameters is shown in figure 4.19(b), where below T_S we see a contraction and expansion of the b and a-axes respectively. This is the opposite to what has previously been observed in cooling through T_{CO2}. The question we must then ask is: does this change in lattice parameters result in a return to the CO1 orbital structure? Our measurements suggest not. In figure 4.20(a) we see that there is a small change in intensity on cooling through T_S, but the biggest change is in the reflection position. Unlike the transition at T_{CO2} we see no evidence of two competing phases, and the change in 2θ is gradual, and not large enough to correspond to a change to the CO1 wavevector. We note that there is a

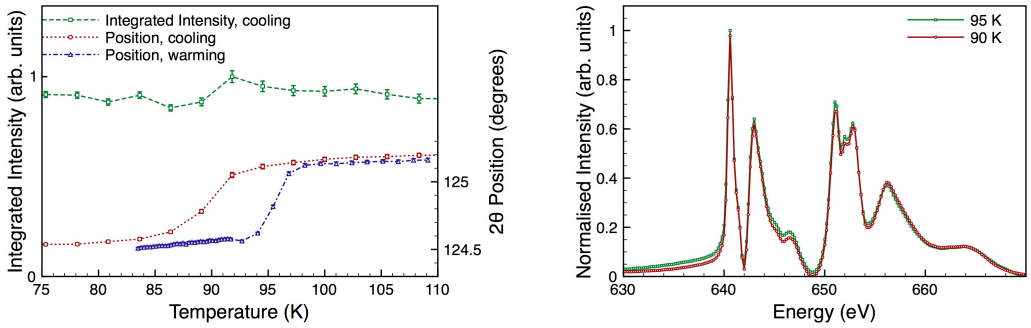

(a) (b)

Figure 4.20: (a) Temperature dependence of the integrated intensity and position of ($\frac{1}{2}$, 0, 0) reflection around T_{S}, measured at 652 eV. (b) Energy scans at fixed wavevector of the ($\frac{1}{2}$, 0, 0) reflection, measured either side of T_{S} on cooling. Results collected on ID08, ESRF.

small offset between the temperature dependencies in figures 4.20(a) and 4.19(b) due to the placement of the temperature sensors. The sensor used in the soft x-ray study was closer to the sample, and so in the authors' opinion is the more reliable measure. Figure 4.20(b) indicates that there is no difference in the local electronic structure over the transition, confirming the lack of any significant change. Despite the relaxation of the CO2 orthorhombic distortion, the strain remains large enough to maintain the CO2 orbital structure at low temperatures. A significant amount of hysteresis is also clear. However, as there is no change in the orbital structure at all, this appears to be a purely structural effect, which is not coupled to the orbital occupation.

4.4 Conclusions

In summary, we have directly observed the orbital order and the orbital stripe rotation in $Pr(Sr_{0.1}Ca_{0.9})_2Mn_2O_7$ using soft x-ray resonant diffraction at the manganese $L_{2,3}$ edges. We have confirmed the hysteresis over the T_{CO2} transition, and found that there is a significant region of coexistence between the two orbitally ordered phases. We do not attribute this coexistence to the presence of a new orbital checkerboard structure, but to a phase separation of the established orbital stripe structures,

in which the CO2 phase is correlated over a much shorter range than at low temperatures.

The spectra at all temperatures are very similar to those previously observed in $LaSr_2Mn_2O_7$ [137], confirming that the reflections are predominantly from orbital order, and that the system is only weakly Jahn-Teller distorted. Our measurements of the azimuthal dependencies of both phases agree well with the expected behaviour for the established orbital stripe structures, despite a small offset which is most likely caused by experimental error. Below T_{CO2} we find a large increase of the intensity of the CO2 type reflections, which we attribute to an increase in the charge disproportionation at low temperatures. Finally, we observe the structural transition at T_{S}, which appears to have negligible effects on the orbital structure, which does not change in any noticeable way. Only small, gradual changes in the spectra are visible over the entire temperature range studied, suggesting there is no change in the type of orbital occupation at T_{CO2}, T_{N} or T_{S}.

Chapter 5

Lutetium Ferrate, $LuFe_2O_4$

5.1 Background

It is clear that the field of multiferroics has generated a significant amount of interest over the last ten years [139–145]. These materials are important as they posses more than one ferroic (and so switchable) property. While the subject initially revolved around a few select materials such as Cr_2O_3 [146, 147], the discovery of new multiferroic mechanisms and systems has greatly broadened the scope for research in recent years. Of particular interest are those materials which exhibit a coupling between two ferroic properties, as these materials may be technologically useful. The primary interest is in simultaneously ferroelectric and (anti)ferromagnetic substances due to the potential for electrically written and magnetically read storage media [148]. As noted by Hill ($n\acute{e}e$ Spaldin) [139], the materials are somewhat of a rarity. In the case of transition metal oxides this is because magnetism on the transition metal ions requires only partially occupied d shells for an uncompensated spin, whereas for ferroelectrics an empty d shell is usually required. With an empty d shell the metal ions are able to cause a distortion of their local environment through strong hybridisation with the oxygen ions. Unequal O-M-O bonding produces dipoles, which results in a net electric polarisation. However, the distortion is greatly reduced for transition metal ions not in this d^0 state, *i.e.* a partially filled d shell [149], due to Coulomb repulsion. Nevertheless such *proper* ferroelec-

tric multiferroics are possible, such as $BiFeO_3$ and $BiMnO_3$, where the bismuth $6s$ lone pairs make the necessary structural distortion possible [145, 150], while the Mn/Fe ions are magnetic. However, this mechanism is not available in the majority of systems, and so an alternative route to ferroelectricity is required. The so-called *improper* ferroelectric multiferroics rely on a separate mechanism to produce the ferroelectric (FE) order [145], such as; geometrical FE as in $YMnO_3$ [151, 152], where a dipole moment is induced through lattice distortions; magnetic FE as in $TbMnO_3$ [144, 153], where a magnetic spiral breaks the inversion symmetry and allows a dipole moment to develop; and charge ordered FE such as in $LuFe_2O_4$ [154–156] where charge ordering between inequivalent layers results in a dipole moment.

Those multiferroics which demonstrate a strong magneto-electric effect are the most interesting with regard to applications, as it is these materials which may provide the next generation of digital storage media. It is unsurprising that in the case of the magnetic FE materials, there is often a strong magneto-electric effect, as the two types of order are clearly strongly coupled. However, this phenomena is not limited to this class of multiferroic.

Lutetium ferrate is one of the most studied materials in the field of strongly correlated electron systems, due to the complexity of the system, which involves elaborate charge and magnetic structures. The high temperature crystal structure is well understood: the system is rhombohedral, belonging to the spacegroup ***R-3m*** (No. 166), with lattice parameters $a = 3.444$ Å and $c = 25.26$ Å in the hexagonal setting [157]. Within each unit cell are three sets of Fe ion *double layers*, arranged in a triangular pattern. The average iron valence is 2.5+, and each double layer is separated by a lutetium layer, figures 5.1 and 5.2.

Below 530 K [157, 158] $LuFe_2O_4$ enters into a two-dimensional charge ordered state within the iron layers, as evidenced by diffuse streaks along the L-axis around $(\frac{1}{3}, \frac{1}{3}, l)$ positions [158–160], as shown in figure 5.3(a). However, due to the triangular lattice, the system is charge frustrated. This frustration can be lifted through the exchange of electrons between the layers in each double layer. This results in

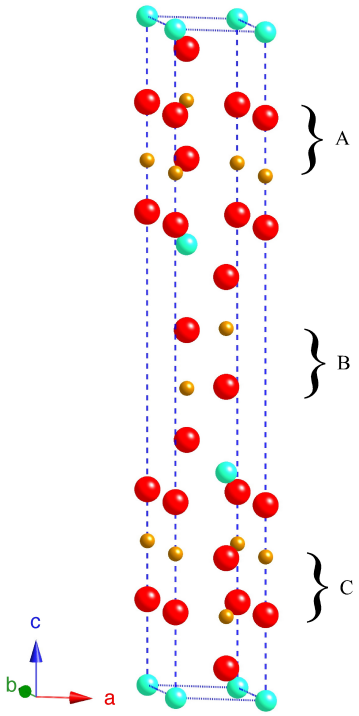

Figure 5.1: The crystal structure of $LuFe_2O_4$, showing the three iron double layers, A, B and C. The iron atoms are orange, the oxygen atoms are red and the lutetium atoms are turquoise.

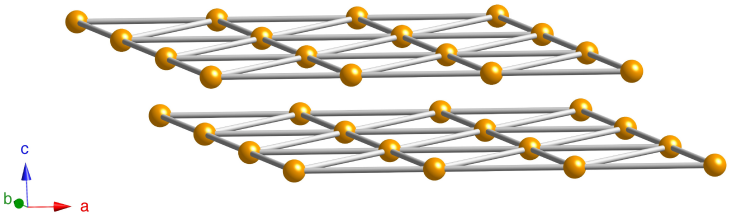

Figure 5.2: A triangular iron double layer from $LuFe_2O_4$.

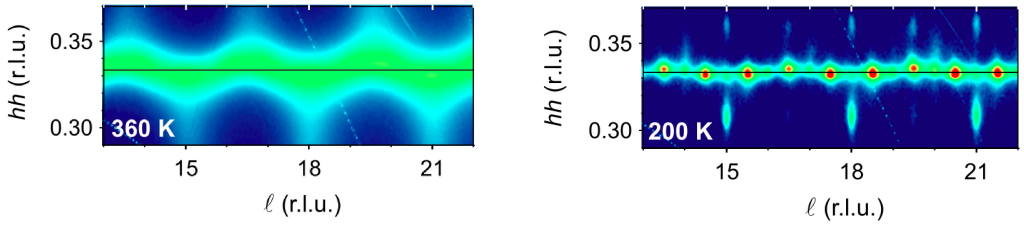

(a) (b)

Figure 5.3: Map of the scattered intensity in the $(h\ h\ l)$ plane, measured using non-resonant x-ray scattering at (a) 360 K and (b) 200 K by Angst *et al*. Reprinted figures with permission from reference 159. Copyright 2008 by the American Physical Society.

a dipole moment on each double layer, producing a two-dimensional ferroelectric layer [160]. In this phase the ordering remains two-dimensional, with a random arrangement of the polarisation directions between double layers [158, 160].

Upon cooling below 320 K three-dimensional charge ordering begins to form [158–160] with a wavevector close to $(\frac{1}{3}, \frac{1}{3}, \frac{1}{2})$. However, the reflections are slightly incommensurate, figure 5.3(b), with positions given by

$$\begin{aligned}
(h,\ h,\ l) + (\frac{1}{3}(1+\delta), \frac{1}{3}(1+\delta), \frac{3}{2}) :&\quad l = 3n \\
(h,\ h,\ l) + (-\frac{2}{3}(1+\delta), \frac{1}{3}(1+\delta), \frac{3}{2}) :&\quad l = 3n+1 \\
(h,\ h,\ l) + (\frac{1}{3}(1+\delta), -\frac{2}{3}(1+\delta), \frac{3}{2}) :&\quad l = 3n-1, \quad \delta \approx 0.0081.
\end{aligned} \tag{5.1}$$

Reflections also appear at positions given by

$$(h,\ h,\ l) \pm (\delta', \delta', \frac{1}{2}) :\quad l = 3n, \quad \delta' \approx 0.030 \tag{5.2}$$

which have been proposed to be third order harmonics of the first set of reflections [158]. Recently additional satellites at positions given by

$$(0,\ 0,\ \frac{3l}{2}) \pm (\tau, \tau, 0) :\quad l = 2n+1, \quad \tau \approx 0.028 \tag{5.3}$$

have also been reported, which demonstrate an inequivalent population distribution between equivalent directions [159], figure 5.4.

Upon cooling below ~ 350 K the system develops a spontaneous polarisation, as demonstrated by pyroelectric current measurements [154, 161], figure 5.5. Large steps in the dielectric constant are also observed, figure 5.6, which are believed to be due to the motion of the FE domain walls [161]. The presence of the three sets of satellites has been ascribed to the presence of three symmetry equivalent domains with each double layer [160]. Each domain consists of a doubly modulated three-dimensional CDW, with the domain populations being unequal in the samples studied to date [114]. Upon cooling into the charge ordered regime, one domain becomes dominant [159]. This has led to a commensurate approximation for the charge ordered structure for each domain [159], figure 5.7. However, in contrast to previous results, this charge ordered structure produces an antiferroelectric polarisation, which is further corroborated by DFT calculations. The DFT calculation performed above T_{CO}, within the two-dimensional charge ordered phase, indicates that in this phase there is a small bias toward FE ordering between layers. One proposed explanation of why previous studies have detected FE below T_{CO} is that the FE only results when an electric field is applied on cooling, thus stabilising the high temperature FE phase which is sustained at low temperatures [159].

Based on resonant hard x-ray results, the charge order in the three-dimensional CO phase is reportedly consistent with ideal Fe^{2+}/Fe^{3+} ionic ordering [162]. However, no fitting is provided to firmly establish the separation, and simulations for smaller charge disproportionations are not shown. Nevertheless, these results are at least partially supported by Mössbauer spectroscopy measurements [163], where Fe^{2+} and Fe^{3+} ions are detected, albeit with considerable fluctuations down to T_{LT} (discussed below). In the former x-ray study, it was also reported that the material exists as an orbital glass, as the observed reflections contained no anisotropic component to the scattering; however, we note here that such a *non-observation* is hardly evidence for such a claim.

Each iron site is surrounded by five oxygens, in a trigonal bipyramid coordina-

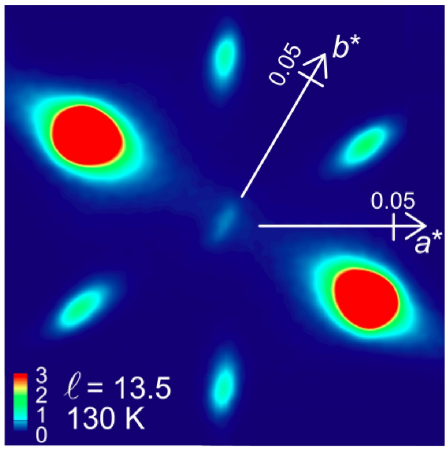

Figure 5.4: The $(0,\ 0,\ \frac{27}{2})$ reflection, and the surrounding $(\tau,\ \tau,\ 0)$ satellites, measured using non-resonant x-ray scattering at 130 K by Angst *et al*. For all samples measured, one domain appears dominant. Reprinted figure with permission from reference 159. Copyright 2008 by the American Physical Society.

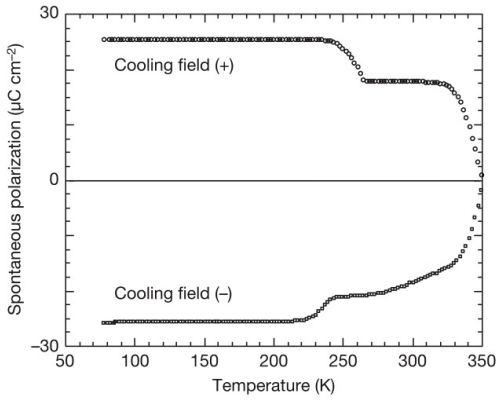

Figure 5.5: The temperature dependence of the spontaneous polarisation, obtained through pyroelectric current measurements by Ikeda *et al*. The sample was cooled in an applied field directed along the c-axis. Reprinted by permission from Macmillan Publishers Ltd: Nature, reference 154, copyright 2005.

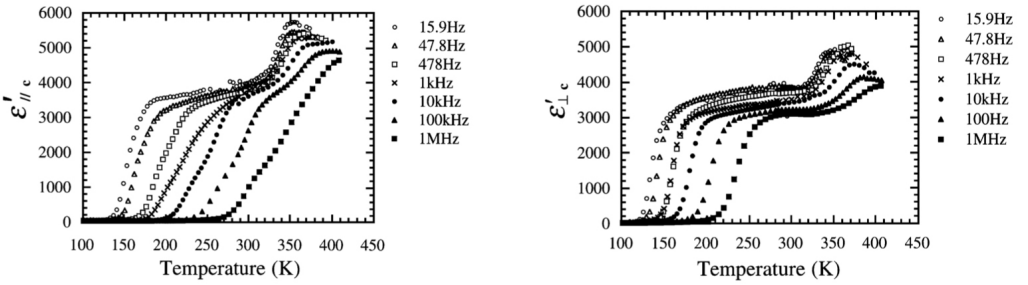

(a) (b)

Figure 5.6: The temperature dependence of the real part of the dielectric constant, parallel to (a) and perpendicular to (b) the c-axis by Ikeda *et al*. Reprinted with permission from the Physical Society of Japan: J. Phys. Soc. Jap., reference 161, copyright 2000.

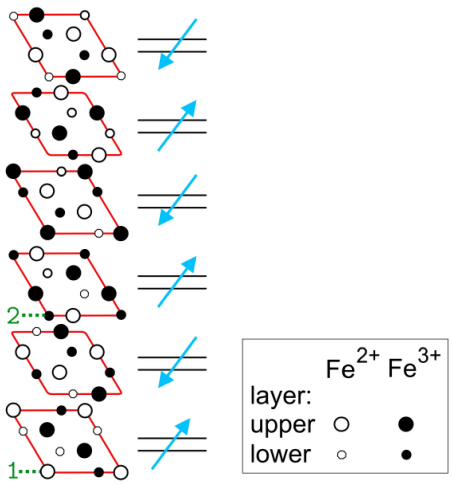

Figure 5.7: A commensurate approximation for the three-dimensional charge order structure, for one of the domains. The figure shows the six iron double layers within the $\sqrt{3} \times \sqrt{3} \times 2$ charge ordered cell, by Angst *et al*. Reprinted figure with permission from reference 159. Copyright 2008 by the American Physical Society.

tion, resulting in a splitting of the $3d$ orbitals into two doublets, and a higher energy singlet [164]. The Fe^{2+} ions therefore possess an orbital degree of freedom on the lowest energy orbital, of dominantly $d_{xy}/d_{x^2-y^2}$ character [165]. The theoretical analysis suggests that at low temperatures this may lead to a frustrated orbital order. The spin structure is also frustrated, when it becomes magnetically ordered at 240 K [166]. The system is ferrimagnetic, with the magnetisation axis directed along the c-axis. Although initial reports found the magnetic structure to be two-dimensional down to 4.2 K [166], more recent reports have found that magnetic reflections are present at positions ($\frac{1}{3}$, $\frac{1}{3}$, l) for L integer and half-integer. Again, three separate domains exist within the magnetic structure, with each shown in figure 5.8. In the recent study by Christianson *et al.* [167] it was found that there is a further transition at 175 K, referred to as T_{LT}. Below this temperature the intensity of the magnetic reflections weaken, figure 5.9, and the reflections become much broader. This has been attributed to a structural phase transition, with the broadening being the result of stacking faults arising in the material. X-ray diffraction results have indicated that this structural transition is the result of a monoclinic distortion, which is sensitive to magnetic field as well as temperature [163].

Importantly there has also been a recent report [168] of a *giant* magnetodielectric response in $LuFe_2O_4$, whereby applying a small magnetic field has significant effects on the real part of the dielectric constant. This is critical as it reveals that these types of multiferroics may indeed have real applications. This connection between the ferroelectricity and the magnetic structure is not unexpected however, as it has previously been predicted that the magnetic order may stabilise the charge ordering, due in part to the frustration of both order parameters [164]. Indeed, the previous values for the spontaneous polarisation maximise and saturate at T_{N} [161]. The effect of the magnetic ordering and the structural phase transition on the charge ordering is still a little unclear at present. Previous x-ray results have shown a slight increase in the intensity of the reflections at the charge ordering wavevector, while showing a slight decrease and increase at T_{LT}, depending on whether it is the commensurate or incommensurate reflection that is being studied [159]. The particular

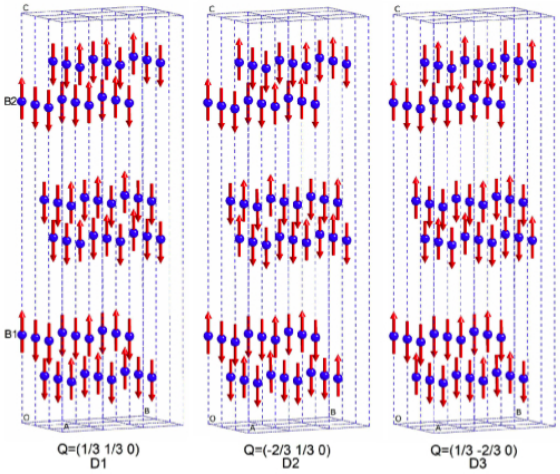

Figure 5.8: The magnetic structure of the three magnetic domains by Christianson *et al*. A single crystallographic unit cell is sufficient to describe the magnetic structure, as the fluctuation of the magnetic structure along the c-axis is believed to be due to the charge variation, rather than a separate modulation. Reprinted figure with permission from reference 167. Copyright 2008 by the American Physical Society.

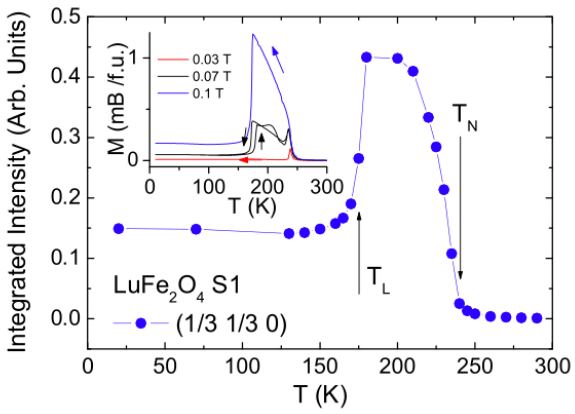

Figure 5.9: Temperature dependence of the magnetic scattering, as measured by neutron diffraction by Christianson *et al*. There is a structural transition at T_{LT}, below which the intensity drops, and the peaks become much broader. Inset: Field cooled magnetisation along the c-axis, showing the sharp feature at 240 K, indicative of high sample quality. Reprinted figure with permission from reference 167. Copyright 2008 by the American Physical Society.

problem in interpreting the data, is that the results principally represent structural distortions rather than the charge order directly. For clarity, the complete phase diagram incorporating the previously discussed results is presented in figure 5.10.

The motivation behind our study was to combine the techniques of hard and soft resonant x-ray scattering in a comprehensive study of a highly topical material. By applying both methods, we hoped to be able to overcome the limitations of the individual techniques and fully assess the local electronic structure within a complex material.

5.2 Sample Preparation and Experimental Technique

The sample was grown using the floating zone method, as described in reference 167, and came from the same high quality batch as used in previous x-ray, neutron and Mössbauer measurements [159, 163, 167]. A sample was chosen which measured approximately 2 mm $\times$ 1 mm $\times$ 0.5 mm, with the short direction being parallel to the c-axis. Due to the extremely long c-axis the sample easily cleaved perpendicular to this direction, providing a high quality surface for scattering. The sample was attached to a Cu puck using silver paint. The sample was removed from the puck after the first experiment, however, the sample cleaved during removal and so for all remaining experiments the sample was left on the same holder without removal. The crystal was pre-aligned on a four-circle diffractometer using a Cu rotating anode source. The τ-satellites were easily visible at room temperature during the alignment procedure, with modest counting times.

To confirm that the sample quality had not degraded, and was equivalent to the samples studied previously, a cleaved layer was subjected to magnetisation measurements, in a Quantum Design SQUID magnetometer (MPMS), figure 5.11. These measurements clearly show the same sharp feature at T_{N} as seen by Christianson *et al.*, as well as other features observed in previous comprehensive magnetisation studies [114]. The same sample was used for all hard and soft x-ray diffraction experiments, although a new surface was cleaved after the first scattering experi-

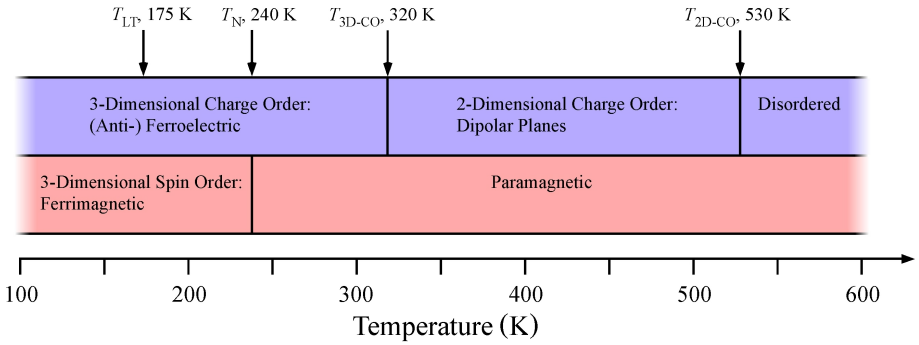

Figure 5.10: Phase diagram of $LuFe_2O_4$, showing the electronic, magnetic and structural transitions.

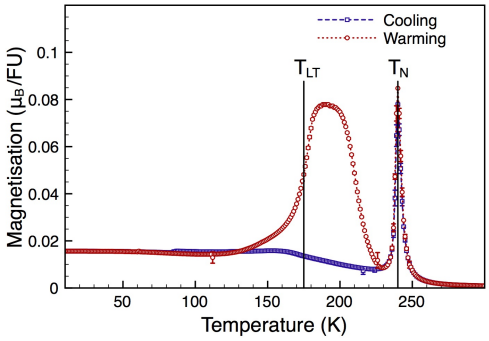

Figure 5.11: Magnetisation measurement per formula unit (FU) along the c-axis on warming and cooling with an applied field of 300 Oe. The transitions previously determined through neutron scattering [167] are indicated.

ment. The sample was studied using hard x-rays at ID20 and XMaS, ESRF, where the machine was operated in *7/8 + 1 mode* [88], with a ring current of 200 mA. The soft x-ray experiments were conducted at ID08, ESRF and I06, DLS. In the first of these studies the machine was operated in *7/8 + 1 mode*, while in the latter the machine was operated both in *hybrid* mode (250 mA) and with a custom filling pattern (275 mA). Soft x-ray diffraction measurements were also taken at the SIM (Surfaces/Interfaces Microscopy) beamline at the SLS (Swiss Light Source), using the RESOXS (REsonant SOft X-ray Scattering) endstation [169]. The SLS is a 2.4 GeV machine, and was operated with a current of 400 mA throughout the experiment.

ID08 was used as described in the last chapter, while on I06 the new RASOR diffractometer was used, making $LuFe_2O_4$ one of the first materials to be studied with this chamber. RASOR (Reflectivity and Advanced Scattering from Ordered Regimes), figure 5.12(a), is a three-circle diffractometer, offering θ, 2θ and χ motions. An attocube piezorotator was also used to provide a ϕ rotation, as shown in figure 5.12(b). The system was cooled using a Janis helium flow cryostat, providing temperatures down to 80 K while using the attocube. The chamber also has two sets of detector slits, a dedicated fluorescence detector, and a conventional analyser stage for a forthcoming polarisation analyser.

The SIM beamline uses two undulators, capable of producing incident light with any arbitrary polarisation, with an energy between 95 and 2000 eV. A collimating mirror is followed by a second mirror and a plane grating monochromator, which is then further collimating by slits. The beam can be refocussed by an additional mirror to produce a focussed spot size of $10\ \mu$m $\times 100\ \mu$m at the sample. However, due to problems regarding translating over the sample, and so hitting different domains, the beam was not refocussed, and the resultant beam was much larger than the sample. The RESOXS endstation is similar to RASOR in many regards, although the geometry of the chamber requires horizontal scattering. The principle difference, at the time of the experiment, was that the RESOXS endstation was equipped with a soft x-ray polarisation analyser. For soft x-rays this requires a custom grown multi-

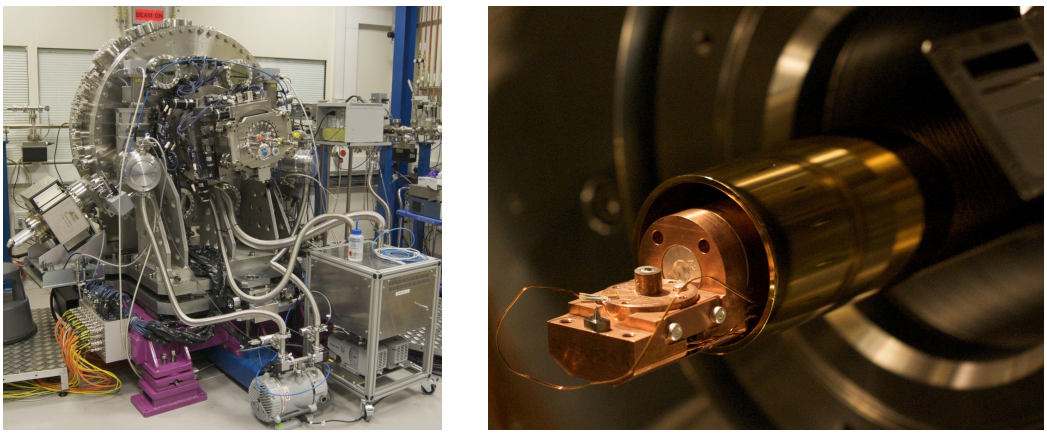

(a) (b)

Figure 5.12: (a) The exterior of RASOR mounted on the I06 beamline at DLS. (b) The sample of $LuFe_2O_4$ mounted on the attocube ϕ rotation on the end of the cryostat inside RASOR.

layer instead of a single crystal, as the lattice spacing of single crystals is generally too small to be of any use in most cases. Here, a thickness graded tungsten/carbon multilayer was used to allow analysis of energies between 700 and 850 eV. Scans at the conclusion of the experiment revealed the leakthrough between channels was approximately 1%. When the multilayer analyser is used the scattered intensity is reduced by approximately 99%, meaning that only very strong reflections can be successfully subjected to full polarisation analysis.

5.3 Results and Discussion

5.3.1 Hard X-ray Scattering

The sample was initially studied on XMaS, using x-rays tuned to just below the iron K edge, and as in previous chapters, an MgO (2 2 2) analyser crystal was used for polarisation analysis. After aligning the crystal, the sample was cooled to 200 K and re-aligned. Several of the superlattice reflections were then identified, including the half integer and τ-satellite reflections. To examine the domain populations a survey was conducted around the (0, 0, $\frac{27}{2}$) reflections, as shown in figure 5.13.

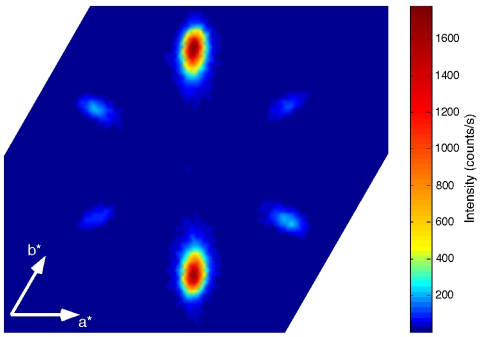

Figure 5.13: Reciprocal space map of the satellites surrounding the (0, 0, $\frac{27}{2}$) reflection, performed at 200 K with an energy of 7.092 keV. Results collected on XMaS, ESRF.

Thus the (τ, -2τ) pair of satellites were identified as being the dominant set. The corresponding scans in reciprocal space are shown in figure 5.14, and their widths given in table 5.1. The ratio of the satellite intensities appeared to differ somewhat with the value of L, with the dominant pair of satellites varying between 4-10 times more intense. In both hard x-ray experiments the (τ, -2τ) pair of satellites remained the dominant pair, despite the surface being re-cleaved. Energy scans of various superlattice reflections were collected, at a variety of temperatures, figures 5.15 and 5.16. We found that there was very little or no resonant enhancement at the iron K edge for the majority of superlattice reflections, with the only exception being the ($\frac{1}{3}$, $-\frac{2}{3}$, $\frac{7}{2}$) reflection. This is in agreement with the prior study conducted by Mulders *et al.* [162], who found very small resonant enhancements at $\frac{1}{3}$-type reflections, although it appears they did not measure the τ-satellites. We see no significant change in the shape of the spectra at different temperatures. We

Table 5.1: Widths and correlation lengths for the (τ, -2τ, $\frac{27}{2}$) reflection, measured at 7.092 keV at 200 K.

Direction	FWHM (r. l. u.)	Inv. Corr. Len. (Å^{-1})	Corr. Len. (Å)
(H, $-2H$, 0)	0.00672 $\pm$ 0.00022	0.01230 $\pm$ 0.00040	113 $\pm$ 4
L	0.03901 $\pm$ 0.00029	0.00480 $\pm$ 0.00004	285 $\pm$ 2

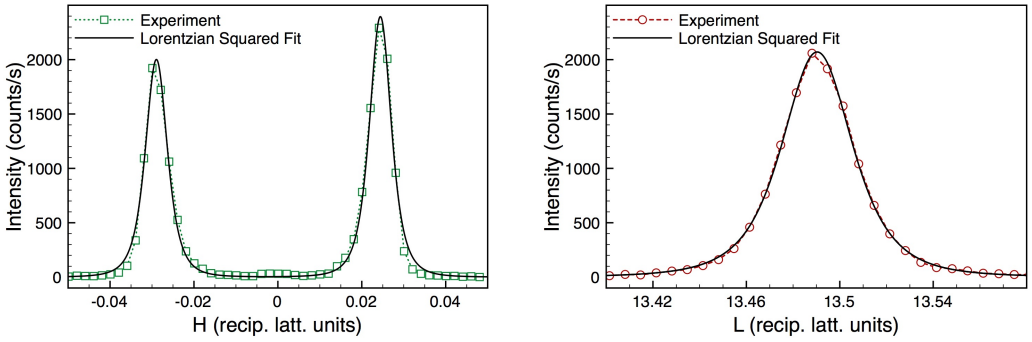

(a) (b)

Figure 5.14: (a) Scan over the $(-\tau,\ 2\tau,\ \frac{27}{2})$, $(0,\ 0,\ \frac{27}{2})$ and $(\tau,\ -2\tau,\ \frac{27}{2})$ reflections along the $[H,\ -2H,\ 0]$ direction. The central reflection is present, but weak, registering less than 50 counts per second. (b) Scan along the L direction, over the $(\tau,\ -2\tau,\ \frac{27}{2})$ reflection. Both scans were performed at 200 K with an energy of 7.092 keV. Results collected on XMaS, ESRF.

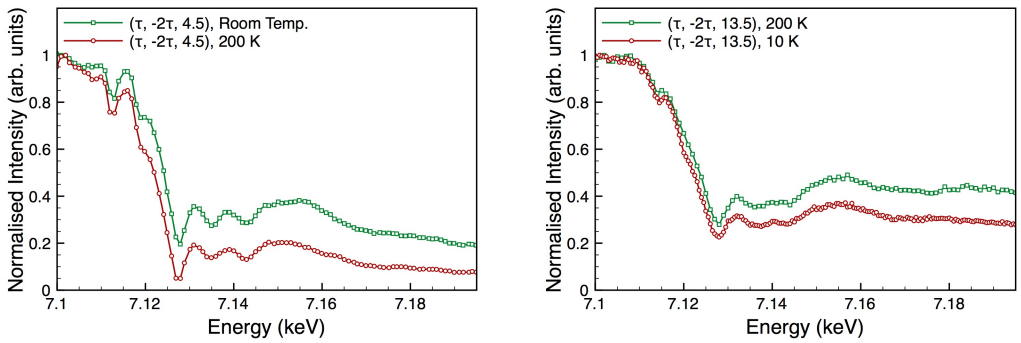

(a) (b)

Figure 5.15: (a) Energy scans at fixed wavevectors of the $(\tau,\ -2\tau,\ \frac{9}{2})$ reflection. Results collected on ID20, ESRF. (b) Energy scans at fixed wavevectors of the $(\tau,\ -2\tau,\ \frac{27}{2})$ reflection. Results collected on XMaS, ESRF. All scans were performed in the σ-σ channel, and have been normalised for ease of comparison.

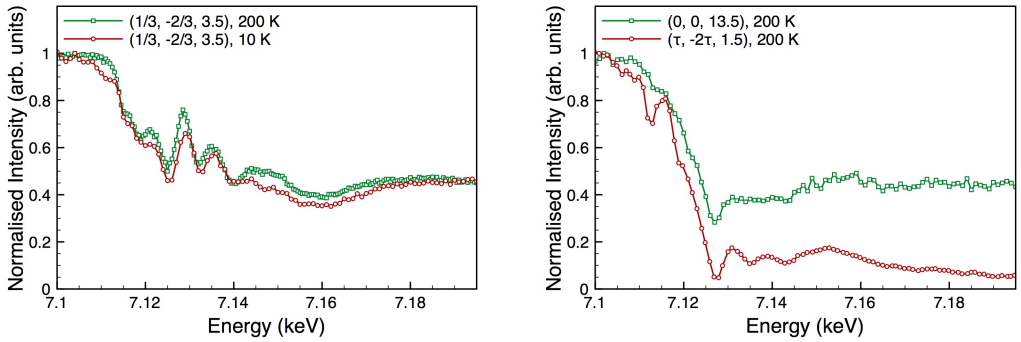

(a) (b)

Figure 5.16: (a) Energy scans at fixed wavevectors of the $(\frac{1}{3}, -\frac{2}{3}, \frac{7}{2})$ reflection. Results collected on XMaS, ESRF. (b) Energy scans at fixed wavevectors of the (0, 0, 13.5) and $(\tau, -2\tau, \frac{3}{2})$ reflections. Results collected on XMaS and ID20, respectively. All scans were performed in the σ-σ' channel, and have been normalised for ease of comparison.

point out here that since very little resonant enhancement is present, it is clear that the reflections observed are primarily the result of the structural distortion associated with the charge order. The lack of changes to the spectra with temperature indicates that there is no significant change to the structure over the temperature range studied. The energy of the incident x-rays was also tuned to the lutetium L_3 edge, and energy scans were conducted at various reflections. However, no resonant enhancements were observed at any reflection.

To detect any anisotropy in the reflections, the sample was subjected to full linear polarisation analysis at several temperatures and energies. The analyser crystal was measured to operate with a channel leakthrough of $\sim 0.33\%$, and a 1200 μm thick diamond phase plate was used. The phase plate was operated in half-wave plate mode, and was calibrated to operate with no less than $98.6 \pm 1.6\%$ linear conversion for all but the final energy, where a conversion of $97.9 \pm 4.5\%$ was achieved. However, even this conversion factor is more than sufficient to detect any anisotropy. Full linear polarisation analysis was conducted on the $(\tau, -2\tau, \frac{9}{2})$ reflection at 7.1155 keV at room temperature and 7.1199 keV at 200 K, and on the $(\frac{1}{3}, -\frac{2}{3}, \frac{7}{2})$ reflection at 7.1276 keV at room temperature and 7.1195 keV at 200 K.

The results for all of these studies were practically identical; a typical example is given in figure 5.17. This is again comparable to the results of the previous study by Mulders *et al*. These results demonstrate that the reflections principally originate from an isotropic charge scattering process, as expected for a structural distortion, and that any structural ATS component is weak. Of course there may be some small anisotropic component, which only becomes apparent when the isotropic term is weakest, close to $2\theta = 90°$, as in the case for iron oxyborate. However, no additional pronounced resonant features appear on the $\frac{1}{3}$-type reflections at higher angles (checked up to $2\theta \approx 82.5°$), suggesting this is not the case; although unfortunately the τ-satellites were only checked up to $2\theta \approx 55.5°$.

5.3.2 Soft X-ray Scattering

To confirm the isotropy, the sample was also studied with soft x-rays, allowing direct access to the iron $3d$ and oxygen $2p$ bands. This does not enable us to solely probe the electronic superstructural order however, and the structural components are still present. Nevertheless, the relative intensities of the superstructural components are much stronger than at higher energies.

Only a few select reflections are accessible at the iron $L_{2,3}$ and oxygen K edges, due to the reduced size of the Ewald sphere at soft x-ray energies. Namely the central (0, 0, $\frac{3}{2}$) reflection and the (τ, τ, $\frac{3}{2}$) satellites. The sample was initially studied at the soft x-ray beamline, ID08 at the ESRF, but also at I06 at DLS and the SIM beamline at the SLS. Due to the slightly different energy calibration of all three beamlines, there is an offset between them, as shown in figure 5.18. Since the exact energy is not required for this discussion this is not a problem, although we are required to choose a calibration for consistency. In that regard the first experiment has been used to provide the definitive energy. ID08 is regularly calibrated using gas absorption, and so in all future figures and text the energies have been adjusted to be consistent with this beamline.

The sample was initially mounted within the ID08 vacuum chamber, such that the (τ, -2τ, $\frac{3}{2}$) reflection was in the scattering plane, directed towards the x-ray

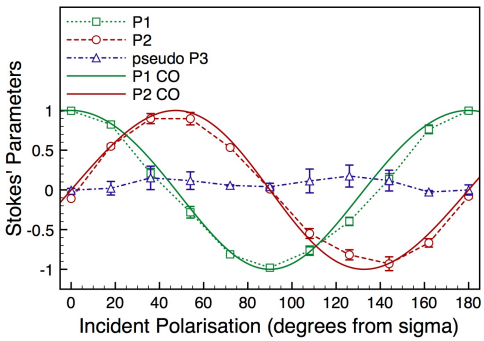

Figure 5.17: Linear polarisation analysis of the $(\tau, -2\tau, \frac{9}{2})$ reflection, at 200 K, performed at an energy of 7.120 keV. The solid lines show the expected dependence for isotropic charge scattering. Results collected on ID20, ESRF.

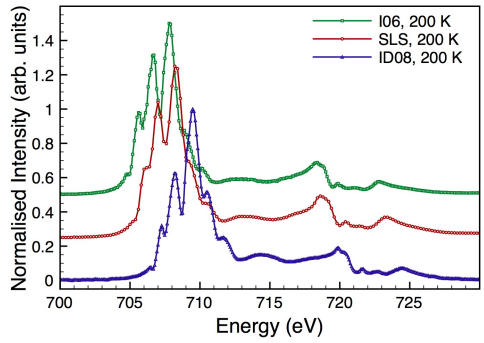

Figure 5.18: Energy scans at fixed wavevector of the $(2\tau, -\tau, \frac{3}{2})$ reflection, measured at 200 K with σ incident polarisation, showing the offsets in energy between ID08, ESRF; I06, DLS; and the RESOXS station at the SLS. In all future figures and in the text, the energies have been re-calibrated to be consistent with the ID08 energies. The scans have been normalised and offset for comparison.

source. The energy of the beamline was then increased to 1.5 keV in order to locate the (0 0 3) Bragg reflection for alignment. This is a rare privilege with soft x-rays, as Bragg reflections are generally outside the Ewald sphere, even at energies up to the typical maximum of soft x-ray beamlines of 2 keV. After alignment the sample was cooled to 200 K, repositioned in the beam, and the (τ, -2τ, $\frac{3}{2}$) reflection searched for at the iron L_3 edge in the σ incident channel. After locating the reflection the sample was scanned with respect to energy, figure 5.19. The (2τ, $-\tau$, $\frac{3}{2}$) satellites were then identified and found to have the same energy dependence. Scans through each of the satellites are shown in figure 5.20. Surprisingly, we found that in contrast to the hard x-ray study, the intensities of the satellites did not coincide with those previously measured. Rather than one set of intense satellites and two weak sets, all of the satellites had intensities with the same order of magnitude. Indeed, the formerly weakest (τ, τ) set of reflections appears to be the strongest in the soft x-ray regime. As soft x-ray diffraction is a near surface probe, rather than a bulk probe (the attenuation length in $LuFe_2O_4$ at the iron L_3 edge is ~ 700 Å), we ascribe this difference to changes in strain near the surface, resulting in an equal preference for domain population. Indeed, a hard x-ray study of thin films of $LuFe_2O_4$ may provide definitive proof of this proposition.

The small penetration depth of soft x-rays often means that an accurate value of the correlation length can not be calculated. However, as shown in table 5.2, the correlation depth as measured by hard x-rays confirms that the correlation length is well within the attenuation length at the iron L_3 edge. From this it is clear that while the superstructure domain populations may be very different at the surface, the charge order is is only slightly less well correlated than in the bulk. This is

Table 5.2: Widths and correlation lengths for the (τ, -2τ, $\frac{27}{2}$) reflection, measured at 709.5 eV at 200 K.

Direction	FWHM (r. l. u.)	Inv. Corr. Len. (Å^{-1})	Corr. Len. (Å)
$(H, -2H, 0)$	0.00713 ± 0.00019	0.01302 ± 0.00034	106 ± 3
L	0.06103 ± 0.00003	0.00759 ± 0.00004	182 ± 1

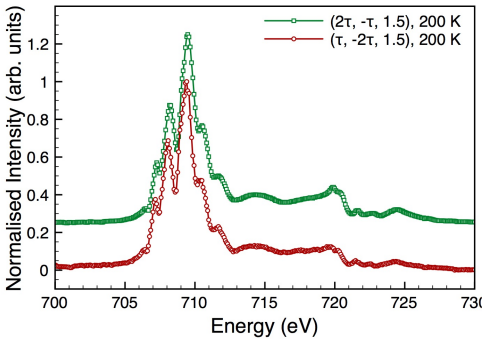

Figure 5.19: Energy scans at fixed wavevector of the $(2\tau, -\tau, \frac{3}{2})$ and $(\tau, -2\tau, \frac{3}{2})$ reflections, measured at 200 K, with σ incident polarisation. The scans have been normalised and offset for comparison. Results collected on ID08, ESRF.

especially clear when we compare figure 5.21 with figure 5.14, where we can clearly see that the reflections have very similar widths.

The satellite reflections were scanned across the iron $L_{2,3}$ edges and the oxygen K edge, with σ and π incident light, at various temperatures, with no post-scatter polarisation analysis, figure 5.22. Fluorescence measurements were also recorded, to confirm that the observed features were not merely from the fluorescent background. As can be seen in figure 5.23, the fluorescence can not be responsible for the observed reflections. The incident energy was also tuned to the lutetium M_5 edge, however no reflections were observed at this energy. The reflection at the oxygen K edge demonstrates a strong hybridisation between the iron and oxygen sites [170]. It is rare to observe such a signal in charge ordered structures, with the obvious exception being the charge stripe cuprates [171]. However, hybridisation is generally present, and it is expected that in this case the low symmetry of the system results in a signal being observed.

We find that there is clearly a change in the local environment with temperature, as there are large differences in the iron L_2 resonance for π incident x-rays, as well as a large change in the relative intensity of the first feature of the L_3 resonance at 85 K. The largest change occurs below T_{LT} indicating that the change in the spectra is related to the change in the structure. In contrast the spectra at the oxygen K

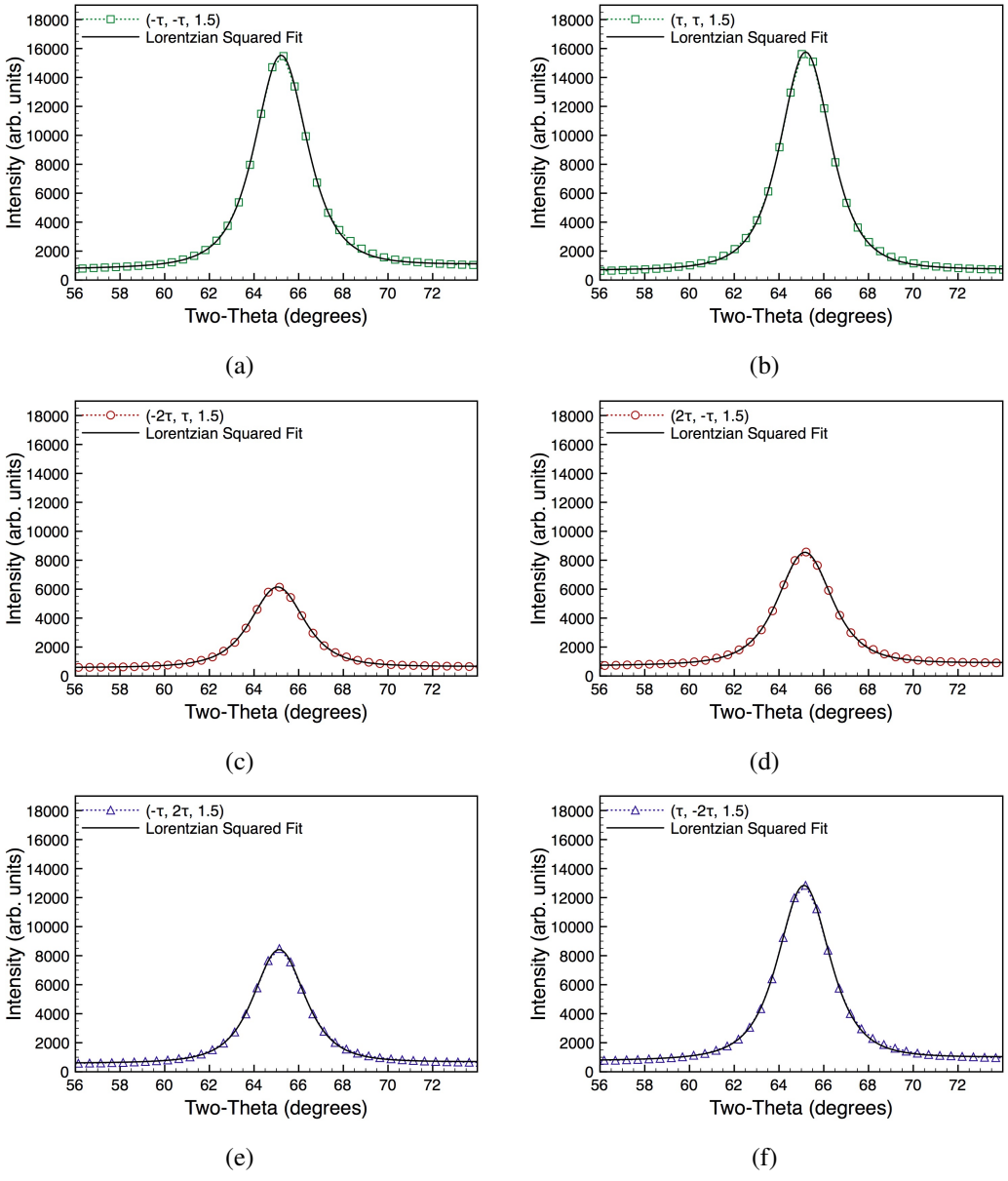

Figure 5.20: θ-2θ scans of the satellites around the (0, 0, 1.5) reflection, measured at 200 K (on cooling), at an energy of 709.5 eV. Results collected on ID08, ESRF.

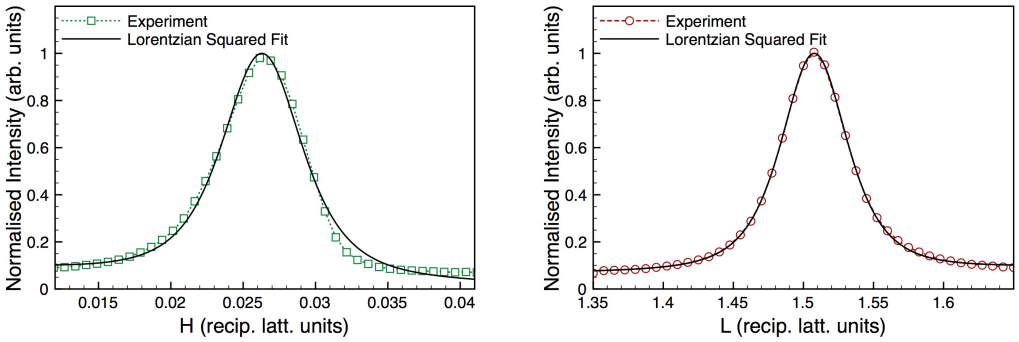

(a) (b)

Figure 5.21: Scans over the $(\tau, -2\tau, \frac{3}{2})$ reflection along (a) the $[H, -2H, 0]$ direction and (b) the L direction. Both scans were performed at 200 K (on cooling) with an energy of 709.5 eV. Results collected on ID08, ESRF.

edge show less significant changes, with no noticeable variation between 200 K and 85 K. As seen in figure 5.24, we see no change in the spectra between warming and cooling through the hysteretic region at 200 K, although the signal is approximately 40% weaker on cooling in both the σ and π incident channels. However, the most surprising result regarding the energy scans, is that the σ and π incident channels clearly produce very different spectra. For isotropic charge scattering we would expect identically shaped spectra, which have an intensity ratio of $1 : \cos^2(2\theta)$ between the σ and π incident channels. However, it is clear that this is not the case, as the spectra are clearly different at both the iron $L_{2,3}$ and oxygen K edges. In fact even for anisotropic scattering we also expect the shape of the spectra for both channels to be the same, as long as there is only one origin for the reflection. The energy scans thus clearly demonstrate that there is at least one anisotropic component to the scattering for the τ-satellites.

In order to investigate this anisotropy, the sample was subjected to linear polarisation analysis, by changing the incident polarisation only. Unlike hard x-rays this does not require the use of a phase plate, or any other absorbing element, but can be achieved by independently controlling the four jaws of the undulator. This was performed at the energies corresponding to the maximum intensities in the incident σ channel for both the iron L_3 and oxygen K edges, as shown in figure 5.25. At 80

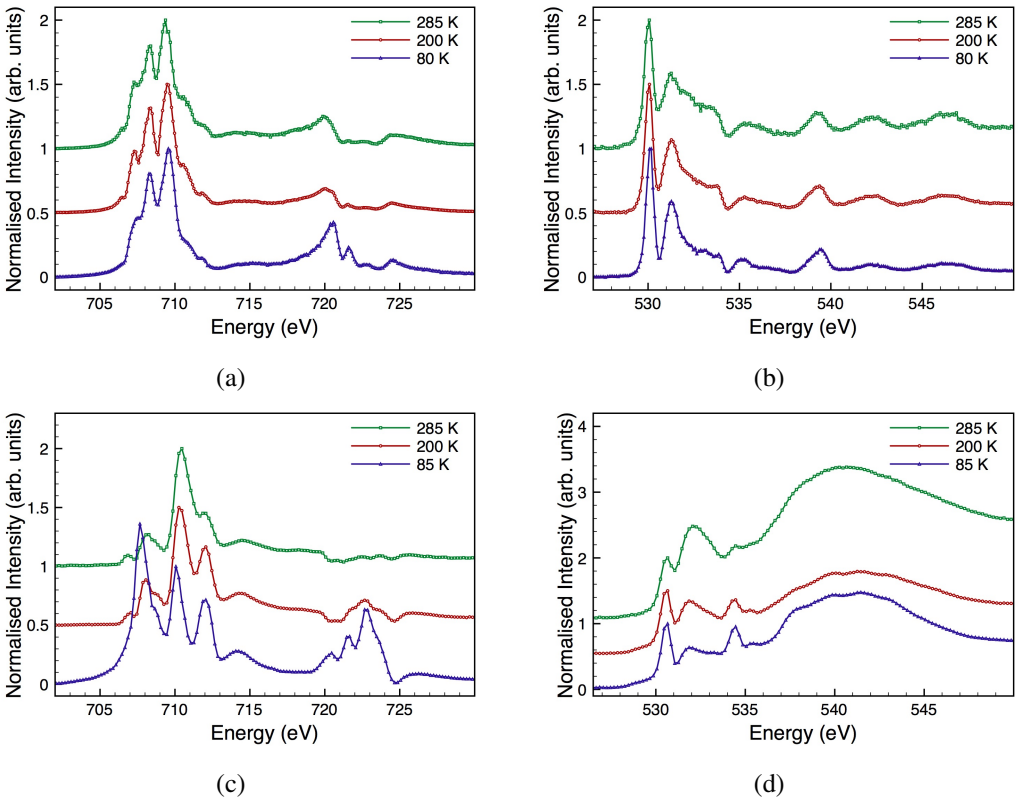

Figure 5.22: Energy scans at fixed wavevector of the $(2\tau, -\tau, \frac{3}{2})$ reflection with σ incident light, at (a) the iron $L_{2,3}$ edges and (b) the oxygen K edge. Results collected on I06, DLS. Energy scans at fixed wavevector of the $(\tau, -2\tau, \frac{3}{2})$ reflection with π incident light, at (c) the iron $L_{2,3}$ edges and (d) the oxygen K edge. Results collected on SIM, SLS. All scans have been normalised and offset for comparison.

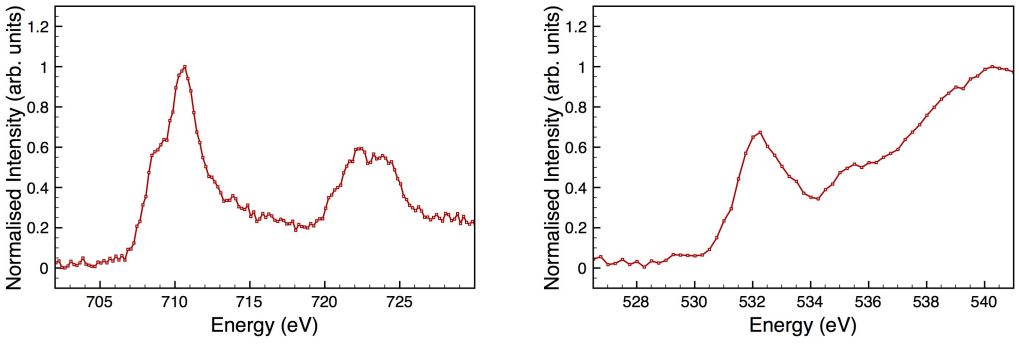

Figure 5.23: Fluorescence measurements at 200 K on cooling, with σ incident light. Results collected on SIM, SLS.

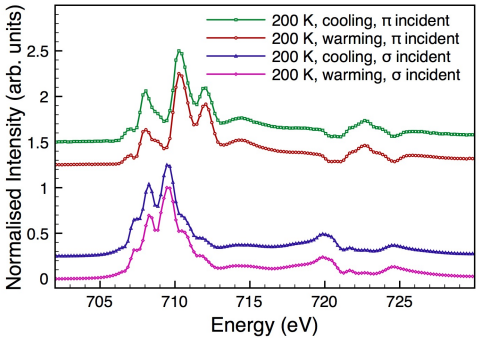

Figure 5.24: Energy scans at fixed wavevector of the $(\tau, -2\tau, \frac{3}{2})$ reflection at 200 K on warming and cooling, at the iron $L_{2,3}$ edges. Results collected on SIM, SLS.

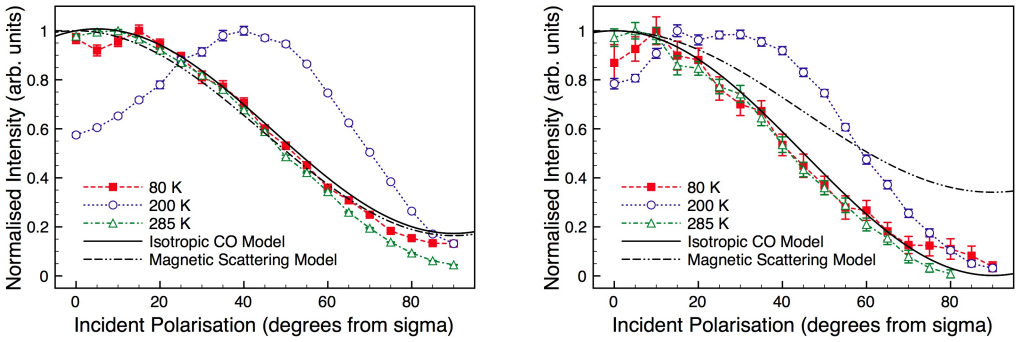

(a) (b)

Figure 5.25: Linear polarisation analysis for the $(2\tau, -\tau, \frac{3}{2})$ reflection, measured at (a) 709.5 eV and (b) 531.3 eV. The solid black line shows the expected behaviour for isotropic scattering while the dot-dashed black line shows the expected behaviour for magnetic scattering. Results collected on I06, DLS.

and 285 K we find that at this energy the dominant contribution appears to be from isotropic charge scattering, in both cases. This is also appears to be true at 200 K, although the anisotropic component is more important at this temperature. The model for magnetic scattering shows a similar dependence, although it clearly can not contribute at 285 K, as it is above T_{N}. To confirm that the magnetic scattering process does not contribute at all, the reflection was studied again using the multilayer polarisation analyser. In this case the scattering was only intense enough to observe in the σ-σ' channel, at all temperatures. This confirms that the scattering process at this energy is charge rather than magnetic, as for magnetic scattering we would expect the rotated polarisation channels to be dominant. Unfortunately the linear polarisation analysis, akin to that shown in figure 5.25, was not repeated at other energies, where the dominant contribution is certain to differ. We must then ask: could magnetic scattering contribute to this reflection at other energies? Since the difference between the σ and π incident spectra do not change significantly between 285 and 200 K this is unlikely, as this is where we would expect to see the biggest change, considering the large feature observed at $\sim$ 200 K in magnetic neutron scattering. The remaining possibility is that the system is simultaneously orbitally ordered within the charge ordered state, and it is the resultant charge-orbital order we are sensitive to at the iron $L_{2,3}$ edges.

It is only natural to ask whether such an anisotropic signal is truly an orbital order contribution, or merely a manifestation of an anisotropic structural distortion (an ATS signal). If it is the latter, then we would naturally expect the signal to also be apparent at the Fe K edge, as observed in magnetite. However, this is a somewhat naive justification, as there is a large isotropic scattering term present, which could mask the ATS contribution, as in Fe_2OBO_3 at low 2θ values. Nevertheless, we are forced to comment on the result observed, which indicates an anisotropy in the iron $3d$ band, which is not detected within the $4p$ band.

A temperature dependence of the $(2\tau, -\tau, \frac{3}{2})$ reflection was subsequently performed at the iron L_3 edge in the σ incident channel, as shown in figure 5.26. On warming from base temperature the τ-reflection is initially relatively stable in in-

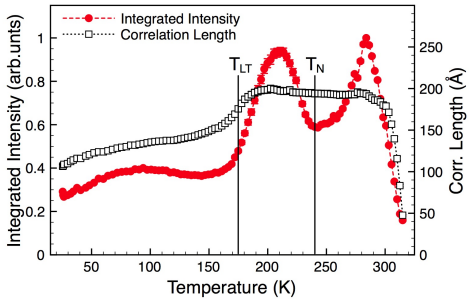

Figure 5.26: The temperature dependence on warming, of the integrated intensity (red circles) and the correlation length (black squares) of the (2τ, $-\tau$, $\frac{3}{2}$) reflection, measured at 709.5 eV. The correlation length is measured along the [H, $-2H$, 0] direction. The transitions previously determined through neutron scattering [167] are indicated. Results collected on ID08, ESRF.

tensity, becoming gradually more correlated toward T_{LT}. However, at T_{LT} we see an increase in the intensity, and a sharpening of the diffraction peaks. This seems to agree with the hard x-ray data measured for the ($\frac{1}{3}$, $\frac{1}{3}$, $\frac{27}{2}$) reflection [159], which shows a sharp jump in intensity at T_{LT}. There is a peak in intensity between T_{LT} and T_{N}, providing evidence for the stabilisation of the charge order by the magnetic structure. However, T_{N} appears to be at a local minima for the intensity of the reflection, above which the charge-orbital order appears to recover. The same behaviour has not been seen in non-resonant hard x-ray studies, which instead have shown a small decrease in intensity between 240 K and 300 K. This difference can be attributed to the fact that we are probing the $3d$ states rather than principally examining the structural distortion. This adds further support to our supposition of charge-orbital order, as if the anisotropy was purely a structural anisotropy, we would expect the hard x-ray temperature dependency to agree well.

The increase in intensity between 240 K and 285 K indicates that there is a greater contrast in the density of states between inequivalent iron sites at this energy. Specifically, this indicates an increase in the charge disproportionation between 240 K and 285 K. This increase is likely to be small however, as there is no significant change in spectra, and the structural distortion related to the charge order continues to decrease with increasing temperature. There is little change in

the correlation length over T_{N}. Finally, the results clearly show the charge-orbital order being extinguished at ≈ 320 K.

Finally, the (0, 0, $\frac{3}{2}$) reflection was studied at both the iron $L_{2,3}$ and oxygen K edges, as shown in figure 5.27. At the iron edges the intensities with σ and π incident polarisations produced identical spectra, in terms of shape and intensity. This is exactly what is expected for this geometry when the magnetisation is directed along the c-axis. This can be seen explicitly when we consider the magnetic (dipole) term in equation 1.24, expressed as a Jones matrix, as written by Hill and McMorrow [172],

$$f_{E1-E1}^{dipole} \propto \begin{pmatrix} 0 & z_1\cos\theta + z_3\sin\theta \\ z_3\sin\theta - z_1\cos\theta & -z_2\sin 2\theta \end{pmatrix}, \tag{5.4}$$

where **z** gives the magnetic dipole moment direction. The axes correspond to the Blume and Gibbs setting, as given in figure 1.9, where the z_3 direction is analogous to the c-axis. At the oxygen K edge we found that the contamination from a higher harmonic, *i.e.* 2×530 eV from the (0 0 3) Bragg reflection almost completely masked the (0, 0, $\frac{3}{2}$) reflection in the σ incident channel. However, we were able to observe the resonance on top of a large harmonic background while using π incident polarisation. This is a demonstration of the $\cos^2(2\theta)$ drop-off for the harmonic background, while the magnetic signal is expected to be equally intense in both incident channels. Harmonic contamination at the iron edges was also present, although observation of the reflection above T_{N} confirmed that the contamination was negligible at these energies.

To definitively confirm that the reflection was magnetic in origin, the reflection was also studied using the multilayer polarisation analyser at the iron L_3 edge. In contrast to hard x-ray studies, the reflection was much stronger than the τ-satellites, making alignment of the polarisation analyser significantly easier. The analysis was conducted at 709.7 eV, and the π-σ' component was found to be the most intense at all temperatures, with the σ-π' channel being three to five times weaker. The non-rotated channels were significantly smaller, with at most 5% of the π-σ' intensity.

However, this is not consistent with the analysis conducted without the polarisation analyser, as the $\sigma \rightarrow \sigma' + \pi'$ intensity was found to be equal to the $\pi \rightarrow \sigma' + \pi'$ intensity. This discrepancy is almost certainly the result of problems in using the analyser stage, which requires moving the graded multilayer and relocating the reflection. The likelihood of the beam being incident on another part of the sample and/or on another part of the multilayer is thus high. Nevertheless, the analysis does confirm that the majority of the signal is in the rotated channels, as expected, with small contributions in the unrotated channels resulting from a combination of channel leakthrough, and the aforementioned complications.

Energy scans were conducted with the polarisation analyser in the rotated channels, shown in figure 5.28. We can clearly see that the channels are identical, although unfortunately the L_2 edge is too weak to observe while using the polarisation analyser. Finally, the temperature dependence at the L_3 edge was collected on both warming and cooling, figure 5.29. In accordance with the neutron data we see a very similar dependence on cooling, with the magnetic reflection showing a maximum intensity at T_{LT}. On warming the sample does not show the same intense feature between T_{LT} and T_{N}, and instead retains the same moderate intensity until collapse at T_{N}. The same drop in correlation length on cooling below T_{LT} is also observed. Perhaps the most surprising aspect about this temperature dependence is how it compares to the magnetisation measurement shown in figure 5.11. In the magnetisation measurement, conducted at 300 Oe, the opposite trend is observed on field cooling and warming. Since the scattering amplitude is proportional to the magnetic moment we may expect to see the same trend. However, the magnetisation measurement records the net modulus magnetisation, while the diffraction measurement represents the magnitude of the moments within a correlated magnetic structure, with a specific wavevector. The measurements are thus not necessarily expected to be identical. In this case our results indicate that on zero-field cooling the magnetic structure undergoes some change below T_{LT} which is then sustained on warming. This change cannot be a change in magnetisation direction, as this would be immediately obvious from a change in the ratio of incident σ:π

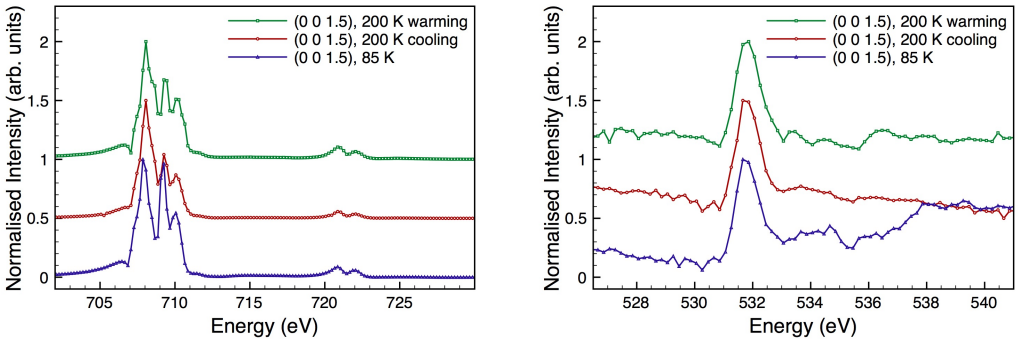

Figure 5.27: Energy scans at fixed wavevector of the (0, 0, $\frac{3}{2}$) reflection, at (a) the iron $L_{2,3}$ edges and (b) the oxygen K edge. The scans have been normalised and offset for comparison. For (a) the σ and π incident channels give exactly equal results. For (b) the σ channel is dominated by contamination from a higher harmonic, and so only the π incident channel is shown. The non-resonant backgrounds have also been subtracted for ease of comparison. Results collected on SIM, SLS.

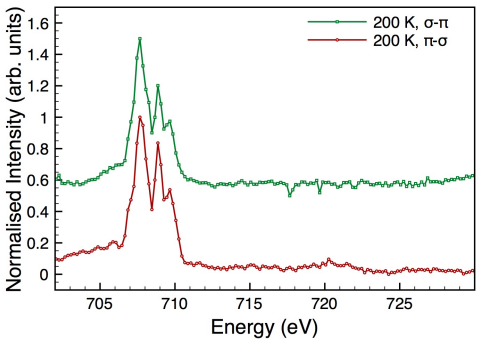

Figure 5.28: Energy scans at fixed wavevector of the (0, 0, $\frac{3}{2}$) reflection, at the iron $L_{2,3}$ edges in the σ-π' and π-σ' channels measured at 200 K on cooling. The scans have been normalised and offset for comparison. Results collected on SIM, SLS.

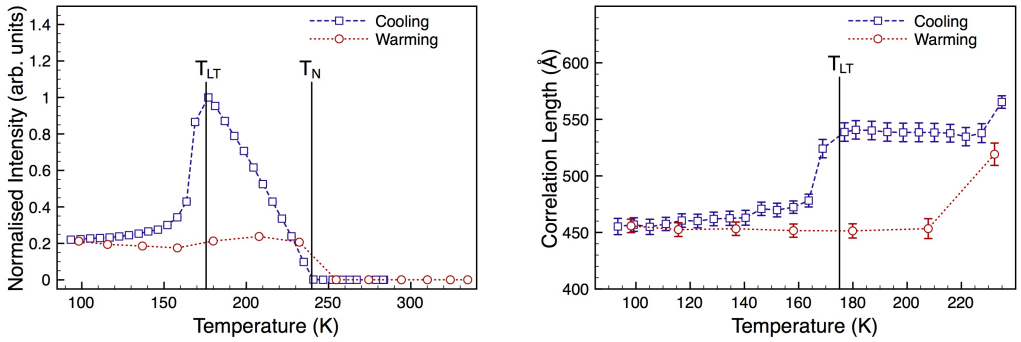

(a) (b)

Figure 5.29: The temperature dependence on cooling and warming, of the (0, 0, $\frac{3}{2}$) reflection, showing (a) the integrated intensity and (b) the correlation length. Above T_N only the second harmonic contamination from the (0 0 3) Bragg reflection was present. The reflection was measured at 707.7 eV. The transitions previously determined through neutron scattering [167] are indicated. Results collected on SIM, SLS.

intensities. The difference is thus most likely a subtle change in magnetic structure. The origin for the increase in the magnetisation on warming is concomitant with the increase in intensity of the charge-orbital reflection on warming, which is most likely due to an increase in the charge disproportionation. This, of course, could explain the increase in magnetisation as well, as the increased charge density on ordered sites necessarily determines the magnitude of the magnetic moment.

5.4 Conclusions

In summary we have principally studied the τ-satellites and the central reflections at $L = \frac{3(2n+1)}{2}$ positions in multiferroic $LuFe_2O_4$ using hard and soft x-ray resonant diffraction. Surprisingly, the reflection is not only visible at the iron edges, but also at the oxygen K edge, which demonstrates a strong hybridisation between the iron and oxygen sites. For the central (0, 0, $\frac{3}{2}$) reflection we have observed a magnetic signal using soft x-rays, which so far has not been detected using neutrons. However, this is due to geometrical constraints in previous neutron studies [114]. The magnetisation axis is confirmed to be along the c-axis at all temperatures, through

consideration of the incident and scattered polarisation channels. We also observe a dramatic change in the magnetic behaviour between cooling and warming, which we attribute to a *locking-in* of the low temperature magnetic structure.

The resonances at the iron $L_{2,3}$ edge for the $(\tau, \ -2\tau, \ \frac{3}{2})$ reflection demonstrate that there is a development of the charge ordered state between phases, with the temperature dependence indicating the charge disproportion experiences a local maximum just above T_{LT}. Both T_{LT} and T_{N} correspond to features in the temperature dependence of the charge order reflection, providing strong evidence for the coupling between the charge and magnetic structures. The hysteresis previously observed below 240 K does not appear to affect the electronic structure significantly, as indicated by the identical spectra on warming and cooling. The most exciting result from the soft x-ray study is the anisotropy associated with the τ-satellites, characteristic of orbital ordering at the charge ordering wavevector. This anisotropy also develops with temperature, as indicated by the soft x-ray polarisation dependencies, for both the iron and oxygen sites. However, at all temperatures the dominant contribution appears to be from isotropic charge scattering.

It is surprising that the anisotropy is not at all apparent at the iron K edge, but by no means inconceivable, as we are probing different electronic states at different angles in 2θ. Our conclusions regarding charge-orbital order are in contrast to those reached by Mulders *et al.* [162], who believed the system to be isotropic; however, such an interpretation is understandable without the corresponding soft x-ray data. This thus highlights the importance of complementary hard and soft x-ray studies in order to fully probe local electronic environments around a site.

Chapter 6

Summary

This thesis has focussed on the phenomena of charge order and orbital order in transition metal oxides, using the technique of resonant x-ray diffraction (RXD): an appropriate approach due to its elemental and band specificity. The technique is powerful, but all too often it is under-appreciated, as studies merely focus on problems which have previously been addressed using neutron or powder techniques. In this thesis we have attempted to address unresolved problems and systems for which RXD is particularly suited.

The first experimental chapter discussed magnetite, which is still often cited as the classic example of a charge ordered material. However, it has become clear that magnetite is a non-ionic charge ordered material, with a complex low temperature electronic and crystal structure. Despite this hindrance, numerous experimental studies have claimed to observe orbital order in recent years. By studying a high quality crystal of magnetite using resonant x-ray diffraction at the iron K edge we have demonstrated that the forbidden $(0, 0, 2n + 1)_C$ and superlattice $(0, 0, \frac{2n+1}{2})_C$ reflections can be adequately explained using a simple charge ordered model. However, we have also employed the technique of full linear polarisation analysis and discovered the remarkable phenomenon of conversion of linearly to non-linearly polarised light, through interference between the iron sublattices at the absorption edge. To the authors' knowledge this is the first report of such a phenomena produced via this mechanism.

In order to extend such analysis to a relatively new system, which has faced similar problems regarding charge order and a complex low temperature crystal structure, the next chapter focussed on iron oxyborate. Fe_2OBO_3 is a system which has previously been described as a fully ionic charge ordered material. However, separate studies have refuted the claim that Fe_2OBO_3 is charge ordered at all. We have demonstrated that the *up/down* structure of iron oxyborate is the correct low temperature structure, and have shown that charge order is necessary to describe the resonant features of select reflections. However, due to the lack of a precise low temperature structure, accurate determination of the charge disproportionation has proved impossible. Despite this limitation we have been able to estimate a charge disproportionation of between 0.4 and 0.8 e^- in order to describe the relative intensities of the resonant/non-resonant features. We have directly observed the hysteretic temperature dependence of the charge order, and found remarkable changes in the correlation of the charge order on a large time-scale. We have also established a difference in the correlation lengths between the surface and bulk of the crystal, with long range charge order only truly developing at a depth greater than 5 μm from the surface. Using full polarisation analysis we have demonstrated the conversion of linearly to non-linearly polarised light, and *vice versa*, and have simulated the conversion well using the FDMNES code. This is found to principally result from interference between the Thomson and anomalous components, and is only visible for those reflections for which the isotropic components are suppressed by the scattering geometry. This is an extension of the mechanism responsible for the non-linear polarisation in magnetite.

The second half of this thesis has focussed on the technique of soft x-ray resonant diffraction (SXRD), which offers the significant advantage of directly probing the transition metal $3d$ band. We have studied $Pr(Sr_{0.1}Ca_{0.9})_2Mn_2O_7$, which is a relatively well understood material. However, by using SXRD we have performed the first direct study of the orbital order. Unlike the majority of layered manganite perovskites, $Pr(Sr_{0.1}Ca_{0.9})_2Mn_2O_7$ possesses an orthorhombic structure, constraining the direction of the orbital stripes. Surprisingly, the system undergoes a rotation

of the stripe direction with little change of the lattice parameters. We have used soft x-ray resonant diffraction at the manganese $L_{2,3}$ edges to directly probe these orbital structures. We have found that there is no change in the type of orbital occupancy over the whole temperature range, and no noticeable change at the low temperature transition, T_{S}. By comparison of the spectra to alternative bilayer manganites we have found that the system is a weakly distorted Jahn-Teller system, with the signal principally originating from the orbital order. There is significant overlap between the two phases, which we attribute to phase separation. We have found a large increase in signal intensity at T_{CO2}, indicative of an increase to the charge disproportionation, which is then constant down to low temperatures.

Finally we have studied lutetium ferrate using both hard and soft x-ray techniques. $LuFe_2O_4$ is a multiferroic material which differs from the majority of multiferroic materials by its unusual ferroelectric mechanism. The frustrated charge ordering results in a dipole moment forming between iron layers, which results in (anti)ferroelectric order below 320 K. We have probed the charge and magnetic structures, revealing coincident features in their temperature dependencies, indicative of magneto-electric coupling. We have confirmed that the magnetic order is directed along the c-axis, with no change in the magnetisation direction over the temperature range studied. Critically, we have detected the first indication of orbital anisotropy within the charge ordered phase. This anisotropy is only apparent when directly probing the iron $3d$ band, while only the structural distortions are evident when probing the $4p$ band, highlighting the importance of complementary hard and soft x-ray techniques.

There is clearly scope for a great deal of future work, as some problems remain unanswered. With regard to magnetite and iron oxyborate, the key is solving the crystal structures. For the case of Fe_2OBO_3 such a refinement will be of great advantage, as it will then be possible to return to the data contained within this thesis, and provide a more accurate value for the charge disproportionation. However, the difficulty is not in producing stoichiometrically correct samples, but in performing a structural refinement over the oppositely distorted charge domains. The solution

thus lies in producing a crystal with a single (or substantially dominant) domain for single-crystal refinement.

For the bilayer manganite and the rare-earth ferrates, the future lies in alternative dopings/dopants. For the bilayer, the region of the phase diagram approaching $y < 0.4$ is of course the most interesting, as it is here where the competition between the different magnetic and orbital order phases can be studied. Meanwhile, it has already been found that ferroelectricity is general to the $R\mathrm{Fe_2O_4}$ series, and so the changes in charge order upon exchange of the rare-earth ion provides an irresistible avenue of study. Simulation of the energy spectra of the τ-reflections is also critical, however, such a simulation over such a huge unit cell is no trivial matter.

In conclusion, we have used resonant x-ray diffraction to study the charge and orbital ordering in a range of complex systems. These properties are key components in the physics of transition metal oxides, and so by increasing our understanding of these phenomena we become capable of creating and manipulating more advanced materials.

References

[1] F. de Bergevin and M. Brunel. *Phys. Lett. A*, 39:141, 1972.

[2] F. de Bergevin and M. Brunel. *Acta Cryst.*, A37:314, 1981.

[3] J. Als-Nielsen and D. McMorrow. *Elements of Modern X-Ray Physics*. Wiley, first edition, 2001.

[4] Q. Huang, M. L. Foo, J. W. Lynn, H. W. Zandbergen, G. Lawes, Yaya Wang, B. H. Toby, A. P. Ramirez, N. P. Ong, and R. J. Cava. *J. Phys.: Condens. Matter*, 16:5803, 2004.

[5] J. M. Tranquada, B. J. Sternlieb, J. D. Axe, Y. Nakamura, and S. Uchida. *Nature*, 375:561, 1995.

[6] Y. Moritomo, A. Asamitsu, H. Kuwahara, and Y. Tokura. *Nature*, 380:141, 1996.

[7] E. J. W. Verwey. *Nature (London)*, 144:327, 1939.

[8] E. J. W. Verwey, P. W. Haayman, and F. C. Romeijn. *J. Chem. Phys.*, 15:181, 1947.

[9] P. A. Miles, W. B. Westphal, and Z. von Hippel. *Rev. Mod. Phys.*, 29:279, 1957.

[10] P. W. Anderson. *Phys. Rev.*, 102:4, 1956.

[11] J. B. Goodenough. *Phys. Rev.*, 100:564, 1955.

[12] P. G. Radaelli, D. E. Cox, L. Capogna, S-W. Cheong, and M. Marezio. *Phys. Rev. B.*, 59:14440, 1999.

[13] Y. Moritomo, Y. Tomioka, A. Asamitsu, Y. Tokura, and Y. Matsui. *Phys. Rev. B.*, 51:3297, 1995.

[14] B. J. Sternlieb, J. P. Hill, U. C. Wildgruber, G. M. Luke, B. Nachumi, Y. Moritomo, and Y. Tokura. *Phys. Rev. Lett.*, 76:2169, 1996.

[15] Y. Tokura, editor. *Colossal Magnetoresistive Oxides*. Gordon and Breach Science Publishers, first edition, 2000.

[16] P. W. Atkins. *Molecular Quantum Mechanics*. Oxford University Press, second edition, 1983.

[17] J. E. Huheey, E. A. Keiter, and R. L. Keiter. *Inorganic Chemistry: Principles of Structure and Reactivity*. Harper Collins College Publishers, fourth edition, 1993.

[18] J. J. Zuckerman. *J. Chem. Edu.*, 42:315, 1965.

[19] E. Wigner. *Phys. Rev.*, 46:1002, 1934.

[20] C. H. Chen, S-W. Cheong, and H. Y. Hwang. *J. App. Phys.*, 81:4326, 1997.

[21] S. Mori, C. H. Chen, and S-W. Cheong. *Nature*, 392:473, 1998.

[22] S. Grenier, V. Kiryukhin, S-W. Cheong, B. G. Kim, J. P. Hill, K. J. Thomas, J-M. Tonnerre, Y. Joly, U. Staub, and V. Scagnoli. *Phys. Rev. B.*, 75:085101, 2007.

[23] C. Kittel. *Introduction to Solid State Physics*. John Wiley and Sons, sixth edition, 1986.

[24] R. E. Thorne. *Physics Today*, May:42, 1996.

[25] M. D. Johannes and I. I. Mazin. *Phys. Rev. B.*, 77:165135, 2008.

[26] E. Nazarenko, J. E. Lorenzo, Y. Joly, J. L. Hodeau, D. Mannix, and C. Marin. *Phys. Rev. Lett.*, 97:056403, 2006.

[27] J. Herrero-Martín, G. Subías, J. García, J. Blasco, and M. C. Sánchez. *Phys. Rev. B.*, 79:045121, 2009.

[28] J. García, M. C. Sánchez, J. Blasco, G. Subías, and M. G. Proietti. *J. Phys.: Condens. Matter*, 13:3243, 2001.

[29] G. Subías, J. García, P. Beran, M. Nevřiva, M. C. Sánchez, and J. L. García-Muñoz. *Phys. Rev. B.*, 73:205107, 2006.

[30] G. Subías, M. C. Sánchez, J. García, J. Herrero-Martín, C. Mazzoli, P. Beran, M. Nevřiva, and J. L. García-Muñoz. *J. Phys.: Condens. Matter*, 20:235211, 2008.

[31] P. M. Woodward, D. E. Cox, T. Vogt, C. N. R. Rao, and A. K. Cheetham. *Chem. Mater.*, 11:3538, 1999.

[32] R. J. Goff and J. P. Attfield. *Phys. Rev. B.*, 70:140404(R), 2004.

[33] J. C. Loudon, S. Cox, A. J. Williams, J. P. Attfield, P. B. Littlewood, P. A. Midgley, and N. D. Mathur. *Phys. Rev. Lett.*, 94:097202, 2005.

[34] H. Raebiger, S. Lany, and A. Zunger. *Nature*, 453:763, 2008.

[35] G. C. Milward, M. J. Calderón, and P. B. Littlewood. *Nature*, 433:607, 2005.

[36] S. Cox, J. C. Loudon, A. J. Williams, J. P. Attfield, P. A. Midgley, and N. D. Mathur. *Phys. Rev. B.*, 78:035129, 2008.

[37] S. Cox, J. Singleton, R. D. McDonald, A. Migliori, and P. B. Littlewood. *Nat. Mat.*, 7:25, 2008.

[38] S. Cox, J. C. Lashley, E. Rosten, J. Singleton, A. J. Williams, and P. B. Littlewood. *J. Phys.: Condens. Matter*, 19:192201, 2007.

[39] D. V. Evtushinsky, D. S. Inosov, G. Urbanik, V. B. Zabolotnyy, R. Schuster, P. Sass, T. Hänke, C. Hess, B. Büchner, R. Follath, P. Reutler, A. Revcolevschi, A. A. Kordyuk, and S. V. Borisenko. *arXiv:0810.3667v1 [cond-mat.str-el] 20 Oct 2008*.

[40] W. R. Busing and H. A. Levy. *Acta Cryst.*, 22:457, 1967.

[41] M. Blume and D. Gibbs. *Phys. Rev. B.*, 37:1779, 1988.

[42] E. Hecht. *Optics*. Addison-Wesley, fourth edition, 2002.

[43] M. Blume. *J. App. Phys.*, 57:3615, 1985.

[44] M. Altarelli. *Magnetism: a Synchrotron Radiation Approach*, chapter *X-ray Scattering of Polarised X-rays: A Theoretical Introduction*. Springer, Berlin, Germany, first edition, 2006.

[45] J. P. Hannon, G. T. Trammell, M. Blume, and D. Gibbs. *Phys. Rev. Lett.*, 61:1245, 1988.

[46] M. Blume. *Resonant Anomalous X-ray Scattering*, chapter *Magnetic Effects in Anomalous Dispersion*. North-Holland, Amsterdam, first edition, 1994.

[47] Y. Murakami, J. P. Hill, D. Gibbs, M. Blume, I. Koyama, M. Tanaka, H. Kawata, T. Arima, Y. Tokura, K. Hirota, and Y. Endoh. *Phys. Rev. Lett.*, 81:582, 1998.

[48] V. E. Dmitrienko. *Acta Cryst.*, A39:29, 1983.

[49] D. H. Templeton and L. K. Templeton. *Phys. Rev. B.*, 49:14850, 1994.

[50] J. Igarashi and T. Nagao. *J. Phys. Soc. Jap.*, 77:084706, 2008.

[51] S. Di Matteo, Y. Joly, and C. R. Natoli. *Phys. Rev. B.*, 72:144406, 2005.

[52] C. Mazzoli, S. B. Wilkins, S. Di Matteo, B. Detlefs, C. Detlefs, V. Scagnoli, L. Paolasini, and P. Ghigna. *Phys. Rev. B.*, 76:195118, 2007.

[53] J. García, G. Subías, M. G. Proietti, H. Renevier, Y. Joly, J. L. Hodeau, J. Blasco, M. C. Sánchez, and J. F. Bérar. *Phys. Rev. Lett.*, 85:578, 2000.

[54] C. Detlefs. *Physica B.*, 345:45, 2004.

[55] Y. Murakami, H. Kawada, H. Kawata, M. Tanaka, T. Arima, Y. Moritomo, and Y. Tokura. *Phys. Rev. Lett.*, 80:1932, 1998.

[56] M. Benfatto, Y. Joly, and C. R. Natoli. *Phys. Rev. Lett.*, 83:636, 1999.

[57] Y. Joly. *Phys. Rev. B.*, 63:125120, 2001.

[58] M. Blackman. *J. Contemp. Phys*, 24:319, 1983.

[59] M. Alexe, M. Ziese, D. Hesse, P. Esquinazi, K. Yamauchi, T. Fukushima, S. Picozzi, and U. Gösele. *Adv. Mat.*, 21:4452, 2009.

[60] H. Li. *Phys. Rev.*, 40:1002, 1932.

[61] T. Okamura. *Sci. Rep. Tohoku Imp. Univ.*, 21:231, 1932.

[62] L. R. Bickford Jnr. *Rev. Mod. Phys.*, 25:75, 1953.

[63] R. W. Millar. *J. Am. Chem. Soc.*, 51:215, 1929.

[64] P. Weiss and R. Forrer. *Ann. Phys.*, 12:279, 1929.

[65] J. P. Shepherd, J. W. Koenitzer, R. Aragón, J. Spalek, and J. M. Honig. *Phys. Rev. B.*, 43:8461, 1991.

[66] I. Leonov, A. N. Yaresko, V. N. Antonov, and V. I. Anisimov. *Phys. Rev. B.*, 74:165117, 2006.

[67] H-T. Jeng, G. Y. Guo, and D. J. Huang. *Phys. Rev. B.*, 74:195115, 2006.

[68] I. Leonov, A. N. Yaresko, V. N. Antonov, M. A. Korotin, and V. I. Anisimov. *Phys. Rev. Lett.*, 93:146404, 2004.

[69] C. Medrano, M. Schlenker, J. Baruchel, J. Espeso, and Y. Miyamoto. *Phys. Rev. B.*, 59:1185, 1999.

[70] J. P. Wright, J. P. Attfield, and P. G. Radaelli. *Phys. Rev. Lett.*, 87:266401, 2001.

[71] J. P. Wright, J. P. Attfield, and P. G. Radaelli. *Phys. Rev. B.*, 66:214422, 2002.

[72] Y. Joly, J. E. Lorenzo, E. Nazarenko, J.-L. Hodeau, D. Mannix, and C. Marin. *Phys. Rev. B.*, 78:134110, 2008.

[73] J. M. Zuo, J. C. H. Spence, and W. Petuskey. *Phys. Rev. B.*, 42:8451, 1990.

[74] G. Subías, J. García, J. Blasco, M. G. Proietti, H. Renevier, and M. C. Sánchez. *Phys. Rev. Lett.*, 93:156408, 2004.

[75] H. Uzu and A. Tanaka. *J. Phys. Soc. Jap.*, 77:074711, 2008.

[76] J.-H. Park, L. H. Tjeng, J. W. Allen, P. Metcalf, and C. T. Chen. *Phys. Rev. B.*, 55:12813, 1997.

[77] J. E. Lorenzo, C. Mazzoli, N. Jaouen, C. Detlefs, D. Mannix, S. Grenier, Y. Joly, and C. Marin. *Phys. Rev. Lett.*, 101:226401, 2008.

[78] D. J. Huang, H.-J. Lin, J. Okamoto, K. S. Chao, H.-T. Jeng, G. Y. Guo, C.-H. Hsu, C.-M. Huang, D. C. Ling, W. B. Wu, C. S. Yang, and C. T. Chen. *Phys. Rev. Lett.*, 96:096401, 2006.

[79] J. Schlappa, C. Schüßler Langeheine, C. F. Chang, H. Ott, A. Tanaka, Z. Hu, M. W. Haverkort, E. Schierle, E. Weschke, G. Kaindl, and L. H. Tjeng. *Phys. Rev. Lett.*, 100:026406, 2008.

[80] S. B. Wilkins, S. Di Matteo, T. A. W. Beale, Y. Joly, P. D. Hatton, P. Bencok, F. Yakhou, C. Mazzoli, and V. A. M. Brabers. *Phys. Rev. B.*, 79:201102(R), 2009.

[81] V. A. M. Brabers. *J. Cryst. Growth*, 8:26, 1971.

[82] N-T. H. Kim-Ngan, W. Soszka, Z. Tarnawski, and A. Kozlowski. *Physica B.*, 353:164, 2004.

[83] J. M. Honig. *J. Alloys Compd.*, 229:24, 1995.

[84] B. A. Calhoun. *Phys. Rev.*, 94:1577, 1954.

[85] S. R. Bland, B. Detlefs, S. B. Wilkins, T. A. W. Beale, C. Mazzoli, Y. Joly, P. D. Hatton, J. E. Lorenzo, and V. A. M. Brabers. *J. Phys.: Condens. Matter*, 21:485601, 2009.

[86] S. R. Bland, B. Detlefs, S. B. Wilkins, T. A. W. Beale, C. Mazzoli, Y. Joly, P. D. Hatton, J. E. Lorenzo, S. D. Brown, and V. A. M. Brabers. *J. Phys.: Conf. Series*, 211:012009, 2010.

[87] M. Hart and L. Berman. *Acta. Cryst.*, A54:850, 1998.

[88] ESRF Machine Webpage. http://www.esrf.eu/accelerators/operation/modes.

[89] B. W. Batterman. *Phys. Rev. B.*, 45:12677, 1992.

[90] C. Giles, C. Vettier, F. de Bergevin, C. Malgrange, G. Grübel, and F. Grossi. *Rev. Sci. Instrum.*, 66:1518, 1995.

[91] V. Scagnoli, C. Mazzoli, C. Detlefs, P. Bernard, A. Fonacaro, L. Paolasini, F. Fabrizi, and F. de Bergevin. *J. Sync. Rad.*, 16:778, 2009.

[92] XMaS Webpage. http://www.esrf.eu/usersandscience/experiments/crg/bm28/.

[93] M. Renninger. *Z. Physik*, 106:141, 1937.

[94] S. B. Wilkins. *Charge and Spin Correlations in Transition Metal Oxides*. PhD thesis, Durham University, 2002.

[95] B. Detlefs, S. B. Wilkins, R. Caciuffo, J. A. Paixão, K. Kaneko, F. Honda, N. Metoki, N. Bernhoeft, J. Rebizant, and G. H. Lander. *Phys. Rev. B.*, 77:024425, 2008.

[96] R. D. Johnson, S. R. Bland, C. Mazzoli, T. A. W. Beale, C-H. Du, C. Detlefs, S. B. Wilkins, and P. D. Hatton. *Phys. Rev. B.*, 78:104407, 2008.

[97] M. Bass, editor. *Handbook of Optics, Classical, Vision and X-ray Optics, Volume 3*. McGraw-Hill, second edition, 2001.

[98] I. S. Elfimov, V. I. Anisimov, and G. A. Sawatzky. *Phys. Rev. Lett.*, 82:4264, 1999.

[99] J. Kanamori. *J. App. Phys.*, 31(5):14S, 1960.

[100] K. I. Kugel and D. I. Khomskii. *Sov. Phys. Usp.*, 25:231, 1982.

[101] J. P. Attfield, A. M. T. Bell, L. M. Rodriguez-Martinez, J. M. Greneche, R. J. Cernik, J. F. Clarke, and D. A. Perkins. *Nature*, 396:655, 1998.

[102] J. P. Attfield, A. M. T. Bell, L. M. Rodriguez-Martinez, J. M. Greneche, R. Retoux, M. Leblanc, R. J. Cernik, J. F. Clarke, and D. A. Perkins. *J. Mater. Chem.*, 9:205, 1999.

[103] R. J. Goff, A. J. Williams, and J. P. Attfield. *Phys. Rev. B.*, 70:014426, 2004.

[104] R. Norrestam, M. Kritikos, and A. Sjödin. *J. Sol. State Chem.*, 114:311, 1995.

[105] A. P. Douvalis, V. Papaefthymiou, A. Moukarika, T. Bakas, and G. Kallias. *J. Phys.: Condens. Matter*, 12:177, 2000.

[106] M. A. Continentino, A. M. Pedriera, R. B. Guimarãaes, M. Mir, J. C. Fernandes, R. S. Frietas, and L. Ghivelder. *Phys. Rev. B.*, 64:014406, 2001.

[107] J. P. Attfield, J. F. Clarke, and D. A. Perkins. *Physica B.*, 180:581, 1992.

[108] I. Leonov, A. N. Yaresko, V. N. Antonov, J. P. Attfield, and V. I. Anisimov. *Phys. Rev. B.*, 72:014407, 2005.

[109] I. Leonov, A. N. Yaresko, V. N. Antonov, J. P. Attfield, and V. I. Anisimov. *Phys. Rev. B.*, 74:176402, 2006.

[110] J. García and G. Subías. *Phys. Rev. B.*, 74:176401, 2006.

[111] M. Angst, P. Khalifah, R. P. Hermann, H. J. Xiang, M.-H. Whangbo, V. Varadarajan, J. W. Brill, B. C. Sales, and D. Mandrus. *Phys. Rev. Lett.*, 99:086403, 2007.

[112] M. Angst, R. P. Hermann, W. Schweika, J-W. Kim, P. Khalifah, H. J. Xiang, M.-H. Whangbo, D.-H. Kim, B. C. Sales, and D. Mandrus. *Phys. Rev. Lett.*, 99:256402, 2007.

[113] Y. J. Song, H. X. Yang, H. F. Tian, C. Ma, Y. B. Qin, L. J. Zeng, H. L. Shi, J. B. Lu, and J. Q. Li. *Phys. Rev. B.*, 81:020101(R), 2010.

[114] M. Angst. *Private Communication*.

[115] A. D. Balaev, O. A. Bayukov, A. D. Vasil'ev, D. A. Velikanov, N. B. Ivanova, N. V. Kazak, S. G. Ovchinnikov, M. Adb-Elmeguid, and V. V. Rudenko. *J. Exp. Theo. Phys.*, 97:989, 2003.

[116] Y. Tokura. *Rep. Prog. Phys.*, 69:797, 2006.

[117] C. Zener. *Phys. Rev.*, 82:403, 1951.

[118] P. W. Anderson and H. Hasegawa. *Phys. Rev.*, 100:675, 1955.

[119] P-G. De Gennes. *Phys. Rev.*, 118:141, 1960.

[120] S. B. Wilkins, P. D. Spencer, T. A. W. Beale, P. D. Hatton, M. von Zimmermann, S. D. Brown, D. Prabhakaran, and A. T. Boothroyd. *Phys. Rev. B.*, 67:205110, 2003.

[121] Y. Tokunaga, T. Lottermoser, Y. Lee, R. Kumai, M. Uchida, T. Arima, and Y. Tokura. *Nat. Mat.*, 5:937, 2006.

[122] D. Okuyama, Y. Tokunaga, R. Kumai, Y. Taguchi, and Y. Tokura. *Phys. Rev. B.*, 80:064402, 2009.

[123] Y. Tokunaga, T. J. Sajo, M. Uchida, R. Kumai, Y. Matsui, T. Arima, and Y. Tokura. *Phys. Rev. B.*, 77:064428, 2008.

[124] Y. Tokunaga, R. Kumai, N. Takeshita, Y. Kaneko, J. P. He, T. Arima, and Y. Tokura. *Phys. Rev. B.*, 78:155101, 2008.

[125] Y. S. Lee, Y. Tokunaga, T. Arima, and Y. Tokura. *Phys. Rev. B.*, 75:174406, 2007.

[126] Z. A. Li, X. Li, Z. Wang, H. F. Tian, C. Ma, L. J. Zeng, and H. X. Yang. *Europhys. Lett*, 86:67010, 2009.

[127] H. Itoh, Y. Tokunaga, N. Kida, R. Shimano, and Y. Tokura. *App. Phys. Lett.*, 96:032902, 2010.

[128] T. A. W. Beale, S. R. Bland, R. D. Johnson, P. D. Hatton, J. C. Cezar, S. S. Dhesi, M. von Zimmermann, D. Prabhakaran, and A. T. Boothroyd. *Phys. Rev. B.*, 79:054433, 2009.

[129] T. A. W. Beale, S. R. Bland, R. D. Johnson, , J. C. Cezar, S. S. Dhesi, D. Prabhakaran, and A. T. Boothroyd. *J. Phys.: Conf. Series*, 211:012007, 2010.

[130] ID08 Webpage. http://www.esrf.eu/usersandscience/experiments/electstructmagn/id08/.

[131] G. Beutier, A. Marty, F. Livet, G. van der Laan, S. Stanescu, and P. Bencock. *Rev. Sci. Instrum.*, 78:093901, 2007.

[132] I06 Webpage. http://www.diamond.ac.uk/home/beamlines/i06.html.

[133] M. D. Roper, G. van der Laan, H. A. Dürr, E. Dudzik, S. P. Collins, M. C. Miller, and S. P. Thompson. *Nuc. Inst. Meth. Phys. Res. A*, 467-468:1101, 2001.

[134] BW5 Webpage. http://hasylab.desy.de/facilities/doris_iii/beamlines/e4856/index_eng.html.

[135] R. Bouchard, D. Hupfeld, T. Lippmann, H-B. Neumann, H. F. Poulsen, U. Rütt, J. R. Schneider, J. Süssenbach, and M. von Zimmermann. *J. Sync. Rad.*, 5:90, 1998.

[136] C. W. M. Castleton and M. Altarelli. *Phys. Rev. B.*, 62:1033, 2000.

[137] S. B. Wilkins, N. Stojić, T. A. W. Beale, N. Binggeli, P. D. Hatton, P. Bencok, S. Stanescu, J. F. Mitchell, P. Abbamonte, and M. Altarelli. *J. Phys.: Condens. Matter*, 18:L323, 2006.

[138] A. Moreo, S. Yunoki, and E. Dagotta. *Science*, 283:2034, 1999.

[139] N. A. Hill. *J. Phys. Chem. B.*, 104:6694, 2000.

[140] J. Wang, J. B. Neaton, H. Zheng, V. Nagarajan, S. B. Ogale, B. Liu, D. Viehland, V. Vaithyanathan, D. G. Schlom, U. V. Waghmare, N. A. Spaldin, K. M. Rabe, M. Wuttig, and R. Ramesh. *Science*, 299:1719, 2003.

[141] N. Hur, S. Park, P. A. Sharma, S. Guha, and S-W. Cheong. *Phys. Rev. Lett.*, 93:107207, 2004.

[142] M. Fiebig. *J. Phys. D: Appl. Phys.*, 38:R123, 2005.

[143] W. Prellier, M. P. Singh, and P. Murugavel. *J. Phys.: Condens. Matter*, 17:R803, 2005.

[144] M. Mostovoy. *Phys. Rev. Lett.*, 96:067601, 2006.

[145] S-W. Cheong and M. Mostovoy. *Nat. Mat.*, 6:13, 2007.

[146] I. E. Dzyaloshinskii. *JETP*, 10:628, 1960.

[147] D. N. Astrov. *JETP*, 11:708, 1960.

[148] W. Eerenstein, N. D. Mathur, and J. F. Scott. *Nature*, 442:759, 2006.

[149] N. S. P. Bhuvanesh and J. Gopalakrishnan. *J. Mater. Chem.*, 7:2297, 1997.

[150] R. Seshadri and N. A. Hill. *Chem. Mater.*, 13:2892, 2001.

[151] C. J. Fennie and K. M. Rabe. *Phys. Rev. B.*, 72:100103(R), 2005.

[152] D. I. Khomskii. *J. Mag. Mag. Mat.*, 306:1, 2006.

[153] M. Kenzelmann, A. B. Harris, S. Jonas, C. Broholm, J. Schefer, S. B. Kim, C. L. Zhang, S-W. Cheong, O. P. Vajk, and J. W. Lynn. *Phys. Rev. Lett.*, 95:087206, 2005.

[154] N. Ikeda, H. Oshumi, K. Ohwada, K. Ishii, T. Inami, K. Kakurai, Y. Murakami, K. Yoshii, S. Mori, Y. Horibe, and H. Kitô. *Nature*, 436:1136, 2005.

[155] T. Portengen, Th. Östreich, and L. J. Sham. *Phys. Rev. B.*, 54:17452, 1996.

[156] J. van den Brink and D. I. Khomskii. *J. Phys.: Condens. Matter*, 20:434217, 2008.

[157] Y. Zhang, H. X. Yang, Q. Guo, H. F. Tian, J. L. Luo, and J. Q. Li. *Phys. Rev. B.*, 76:184105, 2007.

[158] Y. Yamada, K. Kitsuda, S. Nohdo, and N. Ikeda. *Phys. Rev. B.*, 62:12167, 2000.

[159] M. Angst, R. P. Hermann, A. D. Christianson, M. D. Lumsden, C. Lee, M-H. Whangbo, J-W. Kim, P. J. Ryan, S. E. Nagler, W. Tian, R. Jin, B. C. Sales, and D. Mandrus. *Phys. Rev. Lett.*, 101:227601, 2008.

[160] Y. Yamada, S. Nohdo, and N. Ikeda. *J. Phys. Soc. Jap.*, 66:3733, 1997.

[161] N. Ikeda, K. Kohn, N. Myouga, E. Takahashi, H. Kitô, and S. Takekawa. *J. Phys. Soc. Jap.*, 69:1526, 2000.

[162] A. M. Mulders, S. M. Lawrence, U. Staub, M. Garcia-Fernandez, V. Scagnoli, C. Mazzoli, E. Pomjakushina, K. Conder, and Y. Wang. *Phys. Rev. Lett.*, 103:077602, 2009.

[163] X. S. Xu, M. Angst, T. V. Brinzari, R. P. Hermann, J. L. Musfeldt, A. D. Christianson, D. Mandrus, B. C. Sales, S. McGill, J-W. Kim, and Z. Islam. *Phys. Rev. Lett.*, 101:227602, 2008.

[164] A. Nagano, M. Naka, J. Nasu, and S. Ishihara. *Phys. Rev. Lett.*, 99:217202, 2007.

[165] The doubly degenerate orbitals are expressed as $(ad_{yz} - bd_{xy}/ad_{zx} + bd_{x^2-y^2})$ and $(ad_{xy} + bd_{yz}/ad_{x^2-y^2} - bd_{zx})$, with the latter having slightly lower energy. See reference 164 for full details.

[166] J. IIda, M. Tanaka, Y. Nakagawa, S. Funahashi, N. Kimizuka, and S. Takekawa. *J. Phys. Soc Jap.*, 62:1723, 1993.

[167] A. D. Christianson, M. D. Lumsden, M. Angst, Z. Yamani, W. Tian, R. Jin, E. A. Payzant, S. E. Nagler, B. C. Sales, and D. Mandrus. *Phys. Rev. Lett.*, 100:107601, 2008.

[168] M. A. Subramanian, T. He, J. Chen, N. S. Rogado, T. G. Calvarese, and A. W. Sleight. *Adv. Mat.*, 18:1737, 2006.

[169] N. Jaouen, J-M. Tonnerre, G. Kapoujian, P. Taunier, J-P. Roux, D. Raoux, and F. Sirotti. *J. Synchrotron Rad.*, 11:353, 2004.

[170] T. A. W. Beale, S. B. Wilkins, R. D. Johnson, S. R. Bland, Y. Joly, T. R. Forrest, D. F. McMorrow, F. Yakhou, A. T. Boothroyd, and P. D. Hatton. *Submitted to Phys. Rev. Lett.*, 2010.

[171] P. Abbamonte, A Rusydi, S. Smadici, G. D. Gu, G. A. Sawatzky, and D. L. Feng. *Nat. Phys.*, 1:155, 2005.

[172] J. P. Hill and D. F. McMorrow. *Acta. Cryst*, A52:236, 1996.